EXPERIMENTAL INVESTIGATION AND MODELING OF POLYJET AND BINDER JETTING ADDITIVE MANUFACTURING PROCESSES

A Dissertation

by

XINGJIAN WEI

Submitted to the Graduate and Professional School of
Texas A&M University
in partial fulfillment of the requirements for the degree of

DOCTOR OF PHILOSOPHY

Chair of Committee,	Zhijian Pei
Co-Chair,	Li Zeng
Committee Members,	Chao Ma
	Sarah Wolff
Head of Department,	Lewis Ntaimo

May 2022

Major Subject: Industrial Engineering

ABSTRACT

The dissertation has two aspects. The first aspect is to investigate the relationships between process parameters and responses of interest in two types of additive manufacturing processes: PolyJet and Binder Jetting. The second aspect is to compensate color deviations of printed samples from color specifications entered in the printer software using a data-driven approach.

In the first two chapters of the dissertation, the effects of PolyJet process parameters (such as surface finish type, print orientation, and layer thickness) on mechanical properties, surface roughness, and dimensional accuracy of printed samples are investigated by designed experiments. Analysis of variance (ANOVA) is used to determine whether these process parameters are statistically significant. Some process parameters are found to have significant main effects as well as interaction effects on the responses.

From chapter three to chapter five, color inaccuracy issue of the PolyJet process is addressed in three steps. First, the effects of surface finish type on the measured color of printed samples are investigated. Then, a machine learning algorithm, i.e., multilayer perceptron neural network, is utilized to model the relationship between color specification and measured color. The established model results in a high prediction accuracy. Lastly, a compensation methodology, which combines design of experiments, predictive modeling, and multi-response optimization, is proposed to find the optimal color specifications for the printer software to result in a color on the printed sample that

has the smallest deviation from the target color. Case studies validate that the proposed methodology reduces color deviations.

In the last part of the dissertation, powder dispense rate of ultrasonic hopper dispensing system equipped on a Binder Jetting 3D printer is investigated. The effects of initial powder amount, ultrasonic intensity, ultrasonic frequency, and cumulative number of dispensing cycles on powder dispense rate are evaluated experimentally. It is found that powder dispense rate can be controlled by altering process parameters, but it decreases as the powder dispensing process continues, even with fixed process parameters.

ACKNOWLEDGEMENTS

I would like to thank my committee chair, Dr. Pei, my committee co-chair, Dr. Zeng, and my committee members, Dr. Ma and Dr. Wolff, for their guidance and support throughout the course of my PhD journey.

Thanks also go to my friends and colleagues and the department faculty and staff for making my time at Texas A&M University a great experience.

I am also grateful for having an INTERN opportunity at Saint-Gobain Research North America, funded by NSF.

Finally, thanks to my mother and father for their support and to my wife for her patience and love.

CONTRIBUTORS AND FUNDING SOURCES

Contributors

This work was supervised by a dissertation committee consisting of committee chair, Professor Zhijian Pei of the Department of Industrial and Systems Engineering (ISEN), committee co-chair Professor Li Zeng of the School of Data Science at City University of Hong Kong, and committee members Professor Chao Ma of the Department of Engineering Technology & Industrial Distribution (ETID) and Professor Sarah Wolff of the Department of Industrial and Systems Engineering.

Since all the chapters in this dissertation are published or to be published, detailed information about contributors for specific chapters is provided in these papers.

Funding Sources

The major portion of the research contained in this dissertation was financially supported by the startup funds of Professor Zhijian Pei. Financial support in the form of graduate research assistantship in some semesters was provided by NSF and AFOSR. Financial support in the form of graduate teaching assistantship in some semesters was provided by the ISEN and ETID departments. The student is grateful for all the financial supports.

TABLE OF CONTENTS

Page

LIST OF FIGURES

Page

LIST OF TABLES

Page

1. INTRODUCTION

In additive manufacturing (AM), a.k.a. 3D printing (3DP), raw materials are stacked in layer-by-layer fashion by different types of bonding mechanisms to fabricate a 3D object. AM processes involve a variety of process parameters that determine final part qualities (including mechanical strength, surface roughness, dimensional accuracy, and color accuracy). A number of adjustable parameters unique to each AM process exist. Two types of inkjet printing technology-based AM processes are investigated in the dissertation. PolyJet is a photocurable polymer AM process known for its high resolution and accuracy, as well as multi-material capability. Binder Jetting is another jetting-based AM process in which a wide range of metal and ceramic materials in powder shape is temporarily bonded by adhesive binder.

1.1. PolyJet 3D Printing Process

In the literature, process parameters have been investigated and characterized for the PolyJet process. Table 1.1 summarizes frequencies of available literatures about effects of process parameters on final part qualities.

Table 1.1 Literatures and knowledge gaps for the PolyJet process

	Mechanical properties	Surface roughness	Dimensional accuracy	Color accuracy
Print orientation	O	O	O	O
Layer thickness	Δ	Δ	Δ	×
Finish type	Δ	O	Δ	Δ
Shore hardness	×	×	×	×

* O: >3 studies; Δ: 1~3 studies; ×: 0 study

Print orientation is a universal process parameter for most AM processes. Because building an object involves continuous layer stacking, it is an anisotropic process. Especially, complex geometries are affected by print orientation more easily because layering effects could result in different final part properties at local areas. There is a consensus in the literature that orientation along the X axis produced the highest elastic modulus and elongation for the PolyJet process [1-3]. However, results about the effects of print orientation on ultimate tensile strength are not consistent [2-4]. In addition, the effects of print orientation on final part properties are mostly investigated by simple geometries, and there are no reported studies on how the conclusions hold true for complex geometries. Effects of print orientation on surface roughness are well studied [1,5]. It is found that surface parallel to print platform has the lowest surface roughness (up to submicron level), and surface roughness increases as surface orientation increases until 90°. Reported studies contain inconsistent results on which print orientation is better for dimensional accuracy [6,7]. There are only limited numbers of reported studies about the effects of print orientation on color accuracy. It is reported that color uniformity can be affected by print orientation and post-processing [8]. Another study minimizes color variation among different print orientations [9]. However, no study characterizes deviations between the printed colors and colors that set by users. There are no commonly accepted methods to predict and compensate such deviations, either.

Layer thickness is another universal parameter in AM processes. There are fewer reported studies about effects of layer thickness, finish type or types of material on dimensional accuracy in comparison with print orientation [10]. There is a consensus in

the literature that smaller layer thickness gives better dimensional accuracy [11]. It is also reported that layer thickness does not significantly affect surface roughness [5,12]. There is only one reported study that investigates effects of layer thickness on mechanical properties where larger layer thickness is reported to produce higher tensile strength [13].

A number of reported studies investigated the effects of finish type on final part qualities. Despite the differences in printer and material used in reported studies, these studies have a consistent conclusion that glossy finish type leads to lower surface roughness than matte finish type [1,5,12,14]. On the other hand, the conclusions about the effects of finish type on dimensional accuracy is not consistent. One study finds that glossy finish type leads to better accuracy [11], but another study concludes that matte finish type offers better dimensional accuracy [15]. One study claims that changing surface texture (i.e., glossy finish vs. matte finish) would not affect color appearance significantly [16]. However, there are no reported investigations on how finish type affects color accuracy in the PolyJet process.

Shore hardness is a unique parameter in the PolyJet process. There are no reported studies on how Shore hardness would affect final part qualities. Whether or not Shore hardness has an interaction effect with other process parameters is not reported either.

In summary, there are knowledge gaps for each final part quality. First, information on effects of layer thickness on mechanical properties is limited in the literature, and whether there are interaction effects between layer thickness and print orientation is unknown. Second, there are no reported studies on Shore hardness, and the effects of Shore hardness and finish type on surface finish and dimensional accuracy have

not been studied. Lastly, little information on color accuracy of the PolyJet process is available in the literature. Effects of finish type on color accuracy have not been reported.

1.2. Binder Jetting 3D Printing Process

The literature contains reported studies on critical feedstock powder characteristics (e.g., particle sizes, particle distributions, and morphology) that affect final part density [17-19]. Powders of fine particle sizes or irregular morphology have good sinterability but poor flowability, whereas powders of coarse particle sizes or spherical morphology have a poor sinterability but good flowability. Powders with a wide particle distribution are prone to powder segregation but could achieve a higher density, while powders with a narrow particle distribution could lead to a part with uniform microstructures but would not have a high density. Bi-modal powders can take advantage of good powder properties from both fine and coarse powders, and is a compromise between a good sinterability and flowability as well as powder segregation [19].

Critical steps in binder jetting 3D printing that are often investigated in the literature include powder spreading, binder deposition, and sintering [17-19]. Table 1.2 shows steps and related process parameters in the Binder Jetting (BJ) process, and numbers of corresponding studies reported in the literature. Process parameters that significantly affect final part density include binder saturation, layer thickness, roller traverse speed, and roller rotational speed [17]. However, reported effects of powder dispensed amount, which is controlled by powder dispensing, on green density are contradictory in the literature. Two studies concluded that larger dispensed amount

increases green density [20,21], but one study claims that dispensed amount does not increase green density significantly [22].

Table 1.2 Knowledge gaps regarding effects of process parameters on part quality in binder jetting

Step	Parameter	Part Density
Dispensing	Screen size	×
	Ultrasonic frequency	×
	Overdose rate	Δ
Spreading	Roller traverse speed	O
	Roller rotational speed	O
Printing	Layer thickness	O
	Binder saturation	O
Curing	Curing temperature	O
	Curing duration	O
Sintering	Dwelling time	O
	Sintering temperature	O

* O: >3 studies; Δ: 1~3 studies; ×: 0 study

Therefore, there are knowledge gaps for powder dispensing in BJ process. Hopper powder dispensing has been reported in the literature. Discrete Element Method (DEM) has been used to simulate flow behavior of powder inside of a hopper [23-26]. Reported studies also investigate effects of hopper shape, powder refilling and hopper internal angle on dispensing behaviors [28-30]. However, powders used in these studies are relatively large and easy to dispense, and none of the studies are focused on the application to the BJ process.

Powders of fine particle sizes can be dispensed using ultrasonic vibration [31-34]. However, no study on how dispensing parameters, especially ultrasonic frequency ramping pattern and speed would affect dispensing behaviors of fine powders. In addition,

no reported studies are found to investigate changes of powder dispensing behaviors over time, and little information can be found on how initial amount of powders in hopper affects powder dispensing behaviors.

1.3. Dissertation Organization

The first chapter summarizes research gaps in the literature on PolyJet and BJ processes. The second to third chapters present two studies regarding characterization of the PolyJet process. The first study investigates the effects of print orientation and layer thickness on mechanical properties, and the second study characterizes the effects of finish type and Shore hardness on surface roughness and dimensional accuracy. Color accuracy of the PolyJet process is investigated in the fourth to sixth chapters. Chapter 4 examines the effects of material color and finish type on color appearance. Chapter 5 utilizes a machine learning technique to predict printed color given specified color and finish type. Chapter 6 uses response surface methodology to compensate specified color to achieve target printed color. Chapter 7 characterizes ultrasonic hopper powder dispensing process in the BJ process. The last chapter summarizes the contributions of the dissertation.

1.4. References

[1] Cazón, A., Morer, P., and Matey, L., 2014, "Polyjet Technology for Product Prototyping: Tensile Strength and Surface Roughness Properties," Proceedings of the Institution of Mechanical Engineers, Part B: Journal of Engineering Manufacture, 228(12), 1664–1675.

[2] Barclift, M., and Williams, C., 2012, “Examining Variability in The Mechanical Properties of Parts Manufactured Via PolyJet Direct 3d Printing,” International Solid Freeform Fabrication Symposium, pp. 876–890.

[3] Mueller, J., Shea, K., and Daraio, C. ,2015, “Mechanical Properties of Parts Fabricated with Inkjet 3D Printing Through Efficient Experimental Design” Materials and Design, vol. 86, no. 4, pp. 902–912.

[4] Kęsy, A., and Kotliński, J.,2010, “Mechanical Properties of Parts Produced by Using Polymer Jetting Technology,” Archives of Civil and Mechanical Engineering, vol. 10, no. 3, pp.37–50.

[5] Kumar, K., and Kumar, G., 2015, “An Experimental and Theoretical Investigation of Surface Roughness of Poly-Jet Printed Parts: This Paper Explains How Local Surface Orientation Affects Surface Roughness in A Poly-Jet Process,” Virtual and Physical Prototyping, vol. 10, no.1, pp. 23-34.

[6] Singh, R., Singh, V., and Saini, M., 2010, “Experimental Investigations for Statistically Controlled Rapid Moulding Solution of Plastics Using PolyJet Printing,” Proc. ASME 2010 International Mechanical Engineering Congress and Exposition, IMECE2010-37047, pp. 1049-1053.

[7] Haghighi, A., Yang, Y., and Li, L., “Dimensional Performance of As-Built Assemblies in PolyJet Additive Manufacturing Process,” Proc. ASME 2017 12th International Manufacturing Science and Engineering Conference, MSEC2017-2983, V002T01A039.

[8] Ludwig, M., Moroney, N., Tastl, I., Gottwals, M., and Meyer, G., 2018, “Perceptual Appearance Uniformity in 3D Printing,” Electronic Imaging, Material Appearance, vol. 2018, no. 8, pp. 209-221.

[9] Xiao, K., Sohiab, A., Sun, P., Yates, J., Li, C., and Wuerger, S., 2016, “A Colour Image Reproduction Framework for 3D Colour Printing,” Proceedings of the Society of Photographic Instrumentation Engineers, vol. 10153, Advanced Laser Manufacturing Technology, 1015318.

[10] Thakare, K, Wei, X, and Pei, Z., 2019, “Dimensional Accuracy in PolyJet Printing: A Literature Review," Proceedings of the ASME 2019 14th International Manufacturing Science and Engineering Conference, MSEC2019-3018, V001T01A037.

[11] Kechagias, J., Stavropoulos, P., Koutsomichalis, A., Ntintakis, I., and Vaxevanidis, N., 2014, “Dimensional Accuracy Optimization of Prototypes produced by PolyJet Direct 3D Printing Technology,” Proceedings of the International Conference on Industrial Engineering, INDE 2014, pp. 61-65.

[12] Kechagias, J., Iakovakis, V., Giorgo, E., Stavropoulos, P., Koutsomichalis, P., and Vaxevanidis, M, 2014, “Surface Roughness Optimization of Prototypes Produced by PolyJet,” An International Conference on Engineering and Applied Sciences Optimization, pp. 2877–2888.

[13] Pugalendhi, A., Ranganathan, R. and Chandrasekaran, M., 2020, “Effect of Process Parameters on Mechanical Properties of Veroblue Material and Their Optimal Selection in Polyjet Technology,” Int J Adv Manuf Technol vol.108, pp.1049–1059.

[14] Udroiu, R., and Mihail, L., 2009, “Experimental Determination of Surface Roughness of Parts Obtained by Rapid Prototyping,” Proceedings of the 8th WSEAS International Conference on Circuits, Systems, Electronics, Control & Signal Processing, pp.283–286.

[15] Yap, Y., Wang, C., Sing, S., Dikshit, V., Yeong, W., and Wei, J., 2017, “Material Jetting Additive Manufacturing: An Experimental Study Using Designed Metrological Benchmarks,” Precision Engineering, vol. 50, pp. 275–285.

[16] Xiao, B., and Brainard, D., 2008, “Surface Gloss and Color Perception of 3D Objects,” Visual Neuroscience, vol. 25, no. 3, pp. 371–385.

[17] Mostafaei, A., Elliott, A.M., Barnes, J.E., Cramer, C.L., Nandwana, P., and Chmielus, M., 2020, “Binder Jet 3D Printing – Process Parameters, Materials, Properties, and Challenges,” Progress in Materials Science, 100707

[18] Du, W., Ren, X., Pei, Z., and Ma, C., 2020, "Ceramic Binder Jetting Additive Manufacturing: A Literature Review on Density." ASME. J. Manuf. Sci. Eng., vol.142, no.4, 040801.

[19] Li, M., Du, W., Elwany, A., Pei, Z., and Ma, C., 2020, “Metal Binder Jetting Additive Manufacturing: A Literature Review,” ASME. J. Manuf. Sci. Eng., vol. 142, no.9, 090801.

[20] Mendoza, E., Ding, D., Su, L., Joshi, A., Singh, A., Jayan, R., and Beuth, J., 2019, “Parametric Analysis to Quantify Process Input Influence on the Printed Densities of Binder Jetted Alumina Ceramics,” Additive Manufacturing, vol. 30, 100864

[21] Myers, K., 2018, “Smooth, Knurled, Steel, and Dual Roller Testing”, ExOne

[22] Miyanaji, H., Rahman, K., Ma, D., and Williams, C., 2020, “Effect of Fine Powder Particles on Quality of Binder Jetting Parts”, Additive Manufacturing, vol. 36, 101587

[23] Hilton, J., and Cleary, P., 2011, “Granular flow during hopper discharge,” Phys. Rev. E - Stat. Nonlinear, Soft Matter Phys., vol. 84, no. 1, pp. 1–10.

[24] Anand, A., Curtis, J., Wassgren, C., Hancock, B., and Ketterhagen, W., 2008, “Predicting discharge dynamics from a rectangular hopper using the discrete element method (DEM),” Chem. Eng. Sci., vol. 63, no. 24, pp. 5821–5830.

[25] Ketterhagen, W., Curtis, J., Wassgren, C., Kong, A., Narayan, P., and Hancock, B., 2007, “Granular segregation in discharging cylindrical hoppers: A discrete element and experimental study,” Chem. Eng. Sci., vol. 62, no. 22, pp. 6423–6439.

[26] Kumar, R., Patel, C., Jana, A., and Gopireddy, S., 2018, “Prediction of hopper discharge rate using combined discrete element method and artificial neural network,” Adv. Powder Technol., vol. 29, no. 11, pp. 2822–2834.

[27] Liu, S., Zhou, Z., Zou, R., Pinson, D., and Yu, A., 2013, “Flow characteristics and discharge rate of ellipsoidal particles in a flat bottom hopper,” Powder Technol., vol. 253, pp. 70–79.

[28] Albaraki S., and Antony, S., 2014, “How does internal angle of hoppers affect granular flow? Experimental studies using digital particle image velocimetry,” Powder Technol., vol. 268, no. 1, pp. 253–260, 2014.

[29] Engisch, W., and Muzzio, F., 2015, “Feedrate deviations caused by hopper refill of loss-in-weight feeders,” Powder Technol., vol. 283, pp. 389–400.

[30] Uñac, R., Vidales, A., Benegas, O., and Ippolito, I., 2012, “Experimental study of discharge rate fluctuations in a silo with different hopper geometries,” Powder Technol., vol. 225, pp. 214–220.

[31] Lu, X., Yang, S., and Evans, J., 2006, “Studies on ultrasonic microfeeding of fine powders,” J. Phys. D. Appl. Phys., vol. 39, no. 11, pp. 2444–2453.

[32] Matsusaka, S., Urakawa, M., and Masuda, H., 1995, “Micro-feeding of fine powders using a capillary tube with ultrasonic vibration,” Adv. Powder Technol., vol. 6, no. 4, pp. 283–293.

[33] Wei, C., Gu, H., Zhang, X., Chueh, Y., and Li, L., 2019, “Hybrid ultrasonic and mini-motor vibration-induced irregularly shaped powder delivery for multiple materials additive manufacturing,” Addit. Manuf., vol. 33, no. November 2019, p. 101138.

[34] Yang, Y., and Li, X., 2003, “Experimental and analytical study of ultrasonic micro powder feeding,” J. Phys. D. Appl. Phys., vol. 36, no. 11, pp. 1349–1354.

2. EXPERIMENTAL INVESTIGATION OF POLYJET 3D PRINTING PROCESS: EFFECTS OF ORIENTATION AND LAYER THICKNESS ON MECHANICAL PROPERTIES

Paper title:

Experimental Investigation of Stratasys J750 PolyJet Printer: Effects of Orientation and Layer Thickness on Mechanical Properties

Published in:

Proceedings of the ASME 2019 Manufacturing Science and Engineering Conference (MSEC 2019), June 10-14, 2019, Erie, Pennsylvania, USA

Authors' names:

Wei, X.[1], Bhardwaj, A.[1], Shih, C.[2], Tai, B.[2], Zeng, L.[3], Pei, Z.[1]

Authors' affiliations:

1. Department of Industrial and Systems Engineering, Texas A&M University, College Station, Texas 77843, USA
2. Department of Mechanical Engineering, Texas A&M University, College Station, Texas 77843, USA
3. School of Data Science, City University of Hong Kong, Kowloon Tong, Hong Kong SAR, China

2.1. Introduction

In material jetting additive manufacturing processes, droplets of material are selectively deposited [1]. Stratasys PolyJet technology is one type of such processes. Stratasys J750 (Stratasys, Eden Prairie, MN) was released in 2016, and is capable of printing multi materials and multi colors simultaneously. It is worth clarifying the different names of this technology. PolyJet technology was originally invented by Objet Geometries (an Israel based company) in early 2000s, and Stratasys acquired the company in 2012. 3D Systems calls the technology MultiJet printing. Thus, material jetting includes both PolyJet and MultiJet printing.

The J750 printer has several improvements over its predecessor. These improvements include; increased material capacities from 3 to 6 types to accomplish 500,000 different colors in addition to a capability of adjusting material hardness; smaller layer thickness down to 14 μm instead of 16 μm; reduced diameters of nozzles from 50 μm to 10 μm; increased size of build platform to 490 mm × 390 mm × 200 mm; and new E6 print heads with up to 40% longer lifespan. However, information on how orientation and layer thickness affect the mechanical properties of parts printed by J750 is not available in the literature.

Table 2.1 summarizes reported studies about effects of orientation on elastic modulus when printing samples using PolyJet. Note that the model of the printer, model material, and orientations used differ among the studies, and none of the studies were conducted using J750. There is a consensus in the reported studies that orientation XZ produced the highest elastic modulus. Cazon et al. showed that orientation XZ had the

highest elastic modulus among 6 orientations, and the difference was statistically significant [4]. However, Barclift et al. and Mueller et al. draw a conclusion that effect of orientation on elastic modulus was insignificant [5,6].

Table 2.1 Summary of reported studies about effects of orientation on elastic modulus

Ref	Printer	Material	Result
[4] Cazon (2014)	Eden 330	FullCure 720	Samples printed using orientation XZ have the highest UTS
[5] Barclift (2012)	Connex 250	VeroWhite	Insignificant difference between orientations XZ and YZ Insignificant difference between orientations YZ and YX
[6] Mueller (2015)	Objet500 Connex3	VeroWhitePlus	No significant difference between orientations XZ and YZ
[8] Kesy (2010)	Eden 260	FullCure 720	Samples printed using orientation XY have higher than these of XZ
[9] Sai (2018)	Objet260 Connex	VeroWhitePlus	Samples printed using orientation XZ have the highest UTS
[10] Sugavaneswaran (2014)	-	VeroWhite TangoBlackPlus	No significant difference between horizontal, inclined and vertical orientations

Table 2.2 presents the results about effects of orientation on UTS in literatures, which is not consistent in reported studies. Cazon et al. concluded that orientation significantly affected UTS, and orientation XZ produced the highest UTS. Nevertheless, statistical analysis by Barclift et al. and Mueller et al. concluded that the effect of orientation on UTS was insignificant [5,6]. On the contrary, Kesy et al. observed that orientation XY had the highest UTS [8].

Table 2.2 Summary of reported studies about effects of orientation on UTS

Ref	Printer	Material	Result
[4] Cazon (2014)	Eden 330	FullCure 720	Samples printed using orientation XZ have the highest UTS
[5] Barclift (2012)	Connex 250	VeroWhite	Insignificant difference between orientations XZ and YZ Insignificant difference between orientations YZ and YX
[6] Mueller (2015)	Objet500 Connex3	VeroWhitePlus	No significant difference between orientations XZ and YZ
[8] Kesy (2010)	Eden 260	FullCure 720	Samples printed using orientation XY have higher than these of XZ
[9] Sai (2018)	Objet260 Connex	VeroWhitePlus	Samples printed using orientation XZ have the highest UTS
[10] Sugavaneswaran (2014)	-	VeroWhite TangoBlackPlus	No significant difference between horizontal, inclined and vertical orientations

Lastly, samples printed using orientations XY and XZ had similar elongations, and they were larger than these of orientations YX and YZ. This finding is consistent with the results from Mueller et al. where they found that samples printed using orientations XY or XZ produced highest elongation, as shown in Table 2.3.

Table 2.3 Summary of reported studies about effects of orientation on elongation

Ref	Printer	Material	Result
[4] Cazon (2014)	Eden 330	FullCure 720	Significant difference of orientation XZ
[6] Mueller (2015)	Objet500 Connex3	VeroWhitePlus	Significant difference between orientations XZ and YZ Insignificant difference between orientations XY and XZ
[8] Kesy (2010)	Eden 260	FullCure 720	Highest elongation in orientation XY
[9] Sai (2018)	Objet260 Connex	VeroWhitePlus	Highest elongation in orientation XY

In this study, two control factors are investigated: orientation and layer thickness. Mechanical properties studied are elastic modulus, ultimate tensile strength (UTS), and elongation. The rest of the paper is organized as follows. Experimental setups are described in the next section. Then, results of the tensile tests are summarized and

statistical analysis of the results is presented. The effects of orientation and layer thickness are discussed using main effects and interaction effects plots. Statistical analysis of the results is also presented. The final section includes conclusions and future research directions.

2.2. Experimental Setup

2.2.1. Mechanism

The PolyJet AM process is schematically illustrated in Figure 2.1(a), and the Stratasys J750 PolyJet printer (Minnesota, USA) is shown in Figure 2.1(b). J750 is a multi-material printer, and distinguishes itself from its predecessors by increasing material capacities from 3 to 6 types, enabling it to print 500,000 different colors. In the PolyJet printing process, two types of photocurable resins in liquid form, i.e., base model material and support material, are selectively deposited from the print heads. The base model material is used for constructing the object, while the support material is used to temporarily build foundations for the base model material to be printed. After a layer is cured by UV lights attached to both sides of the print heads, the build platform goes down by the height of one layer, and the materials are deposited again. These steps are repeated until the object is completed.

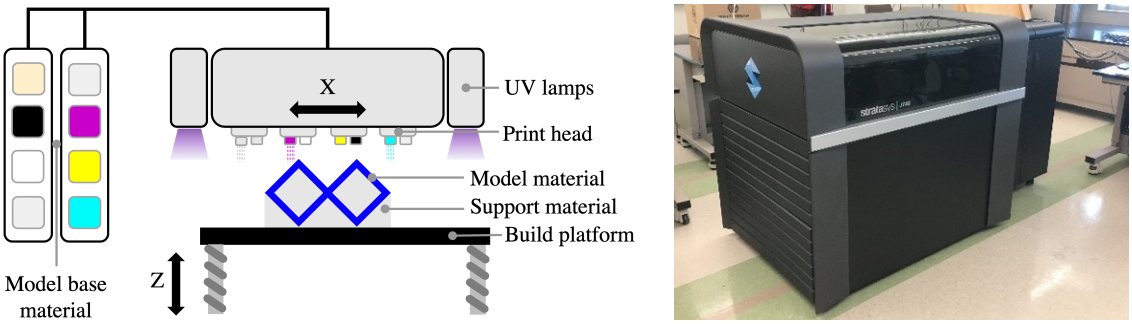

(a) (b)

Figure 2.1 PolyJet AM process. (a) Illustration of the PolyJet printing process, and (b) picture of the Stratasys J750 PolyJet printer

2.2.2. Sample generation

Dimensions of tensile samples were in accordance with ASTM D638-14 type 1 standard [2]. The dimensions of the samples were drawn in SolidWorks, and exported as a binary STL file. The defined axes are corresponding to those set by the printer manufacturer, and the X and Z axes are shown in Figure 2.1(a). The Y axis is perpendicular to the surface of this paper. The STL file was imported to a software interface called GrabCAD Print. The user can also set control factors using it.

2.2.3. Printing conditions for samples

Different levels selected for the two control factors are presented in Table 2.4. There were six different orientations illustrated in Figure 2.2, and two levels of layer thickness: 14 μm (1800 dpi) and 27 μm (900 dpi). Nomenclature of the orientations is defined as follows: the first letter represents the direction that the longest dimension of the sample is parallel to, the second letter represents the direction that the largest surface of

the sample is perpendicular to. For example, “orientation XZ” means that the sample is parallel to the X axis, and its largest surface is perpendicular to the Z axis.

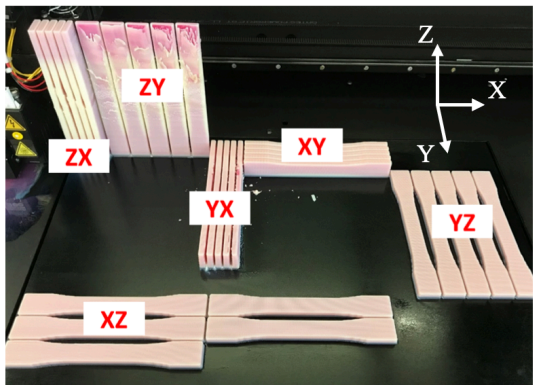

Figure 2.2 Printed samples in 6 orientations

Table 2.4 Levels of control factors

Control factor	*Level 1*	*Level 2*	*Level 3*	*Level 4*	*Level 5*	*Level 6*
Orientation	XY	XZ	YX	YZ	ZX	ZY
Layer thickness	14 μm	27 μm	-	-	-	-

Other parameters are kept the same for all samples. The resolutions of the printer in the XY plane are 42 μm (600 dpi). All the samples were made by the same model material called VeroMagenta RGD 851. According to Stratasys’s mechanical property datasheet, all materials in the Vero family have similar properties, so the color of the material is not considered in this study [3]. SUP705 was used for support material. Matte is selected as finish type, and Shore hardness value is set to 100 for all samples. Under each of the 6 orientations, 5 samples were replicated, making 30 samples in total per printing under each layer thickness. The samples were printed after 2 months of the machine installation, and maintenances such as cleaning were carried out on the daily basis.

Orientations ZX and ZY used for tensile testing were printed separately. When these samples were printed together with samples of other orientations, the surfaces of the samples were extremely inferior, as illustrated in the bottom of Figure 2.3, perhaps due to their small contact area at the bottom of the samples with the build platform. Thus, an alternative approach was adopted to print them. Specifically, two thin rectangular parts (163.6 mm × 18.75 mm × 3mm) were leaning toward both sides of the sample as close as possible without touching. The parts were printed together with each sample to allow support materials to fill up between the sample and the support parts. Therefore, the contact area at the bottom of the samples with the build platform was increased, and the samples were stabilized. The resulting printed samples, as shown in the top side of Figure 2.3, become much smoother.

Figure 2.3 Printed sample without support parts (bottom), and printed sample with support parts (top)

2.2.4. Post-processing of samples

After the completion of a printing, wax-like support materials (SUP705) on every surface of samples were manually removed by a scraper. Then, pressurized water was blasted to the samples to further remove the support materials. Caution must be taken while using the pressurized water because high pressure could break the samples. Also, it

is optional to immerse the cleaned samples into caustic solution to further clean it, but immersing the samples for a long time may corrode it and make it brittle. Caustic solution was not used because it could affect the mechanical properties of the samples.

2.2.5. Measurement of mechanical properties

To measure the mechanical properties of printed samples, an Instron 4411 tensile testing machine was used, as shown in Figure 2.4. The testing machine is equipped with a 5 kN load cell. The test speed of 5.08 mm/min was used for all samples. Engineering stress-strain curves were obtained from the machine, and mechanical properties (elastic modulus, ultimate tensile strength, and elongation) were extracted from the stress-strain curve for each sample. Each mechanical property is defined as follows:

- *Elastic modulus:* the stress applied on a body to the resulting strain within the elastic limit, measured in ksi. First 30 data points are used to calculate the modulus.
- *Ultimate tensile strength (UTS):* the maximum strength that a material can withstand before rupture, measured in ksi. The highest value of each stress-strain curve is recorded.
- *Elongation:* the ratio between changed length and initial length after the sample breaks, measured in percentage.

Figure 2.4 Instron 4411 tensile testing machine

2.3. Results and Discussions

2.3.1. Main effects of orientation

Table 2.5 summarizes the measured mechanical properties under six levels of orientations, where “Std. Dev” is standard deviation of the measurements at one level of orientation, and each level of orientation has 10 samples. The largest values in the mean column are in bold, and the smallest values in the standard deviation column are in bold. Figure 2.5, Figure 2.6, and Figure 2.7 show the main effects of orientation on elastic modulus, UTS, and elongation, respectively. The effects of orientations on UTS and elongation are larger than those for elastic modulus. Orientation XY led to the largest elastic modulus and elongation, while orientation YZ produced the highest UTS. On the other hand, orientations ZX and ZY resulted in much lower UTS and elongation than other

orientations. From Figure 2.7, it can be observed that the samples printed with their longest dimension aligned with the X axis (orientations XY or XZ) exhibited larger elongation than these aligned with the Y axis (orientation YX or YZ).

Table 2.5 Results of measured mechanical properties under six levels of orientation

Orientation	*Elastic Modulus (ksi)*		*UTS (ksi)*		*Elongation (%)*	
	Mean	*Std. Dev*	*Mean*	*Std. Dev*	*Mean*	*Std. Dev*
XY	**232**	13.9	7.8	0.16	**11.3**	0.82
XZ	228	**7.3**	7.9	**0.09**	11.2	1.40
YX	216	21.5	6.5	1.90	7.4	2.95
YZ	229	13.9	**8.1**	0.22	9.8	0.72
ZX	213	10.1	3.9	0.63	3.0	0.45
ZY	208	15.8	3.9	0.22	3.1	**0.21**

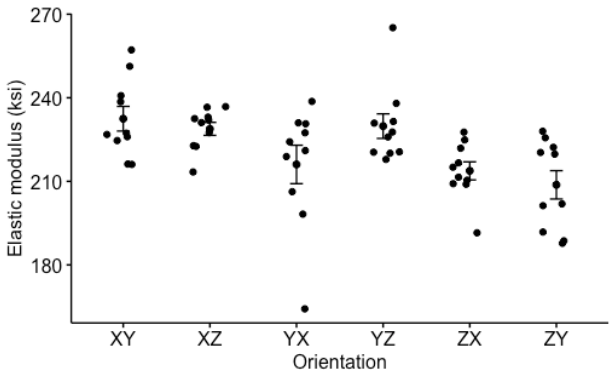

Figure 2.5 Main effects of orientation on elastic modulus

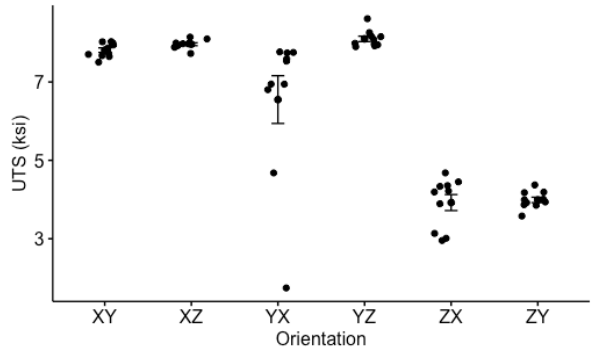

Figure 2.6 Main effects of orientation on UTS

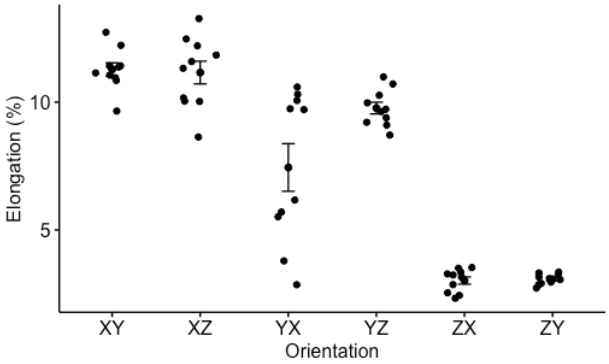

Figure 2.7 Main effects of orientation on Elongation

2.3.2. Main effects of layer thickness

Table 2.6 summarizes the measured mechanical properties under the two levels of layer thickness, and each level of layer thickness has 30 samples. All mechanical properties under the larger layer thickness surpassed those under the smaller layer thickness. Figure 2.8, Figure 2.9, and Figure 2.10 show the main effects of layer thickness on elastic modulus, UTS, and elongation, respectively. Elastic modulus was the only response where the two layer thicknesses had similar means. For UTS and elongation, larger layer thickness led to higher values. Moreover, a clear clustering patterns can be observed within each layer thickness in the plots of UTS and elongation: the lower cluster

of points were from samples printed with their longest dimension parallel to the Z axis, and the higher cluster were from the samples aligned with X or Y axis. Note that no study was found to have investigated the effects of layer thickness on the mechanical properties.

Table 2.6 Results of measured mechanical properties under two levels of layer thickness

Layer thickness (μm)	*Elastic Modulus (ksi)*		*UTS (ksi)*		*Elongation (%)*	
	Mean	*Std. Dev*	*Mean*	*Std. Dev*	*Mean*	*Std. Dev*
27	**221.8**	**15.3**	**6.7**	**1.82**	**8.4**	3.78
14	221.3	17.5	6.0	2.12	6.9	**3.65**

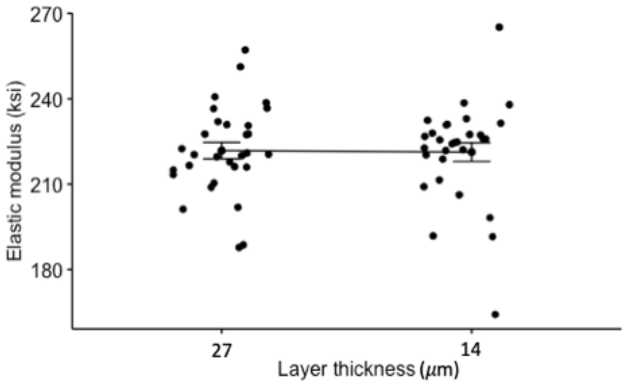

Figure 2.8 Main effects of layer thickness on elastic modulus

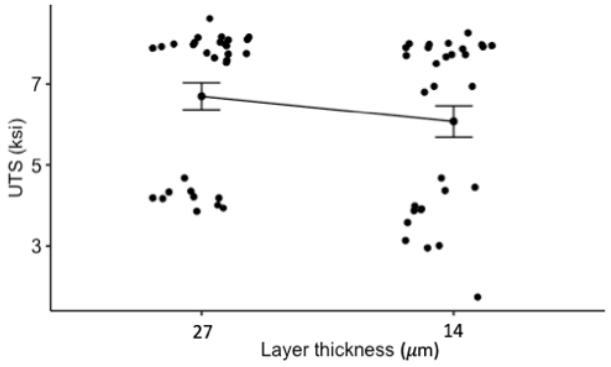

Figure 2.9 Main effects of layer thickness on UTS

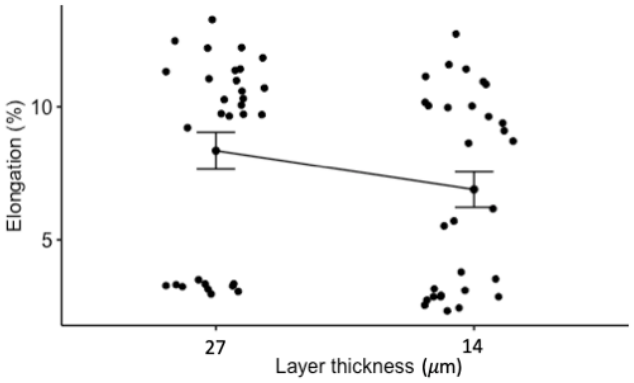

Figure 2.10 Main effects of layer thickness on elongation

2.3.3. Interaction effects of orientation and layer thickness

Figure 2.11 shows the interaction effects of orientation and layer thickness for elastic modulus. It can be seen that significant interaction effects exist. For example, changing layer thickness from 14 μm to 27 μm increased elastic modulus for samples printed using orientations XY, YX, and ZX. However, changing layer thickness from 14 μm to 27 μm decreased elastic modulus for samples printed using orientations XZ, YZ and ZY.

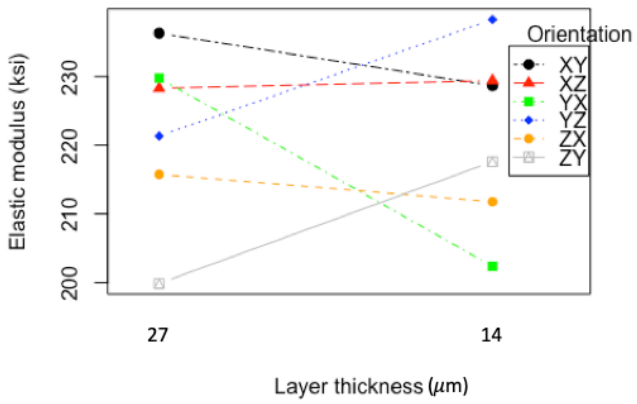

Figure 2.11 Interaction effect plots of orientation and layer thickness for elastic modulus

Figure 2.12 shows the interaction effects of orientation and layer thickness for UTS. Significant interaction effects can be observed. For example, changing layer thickness from 14 μm to 27 μm did not cause observable changes in UTS for samples printed using orientations XY, XZ, YZ, ZX, and ZY. However, changing layer thickness from 14 μm to 27 μm caused significant change in UTS for samples printed using orientation YX (from about 5.4 ksi to 7.7 ksi).

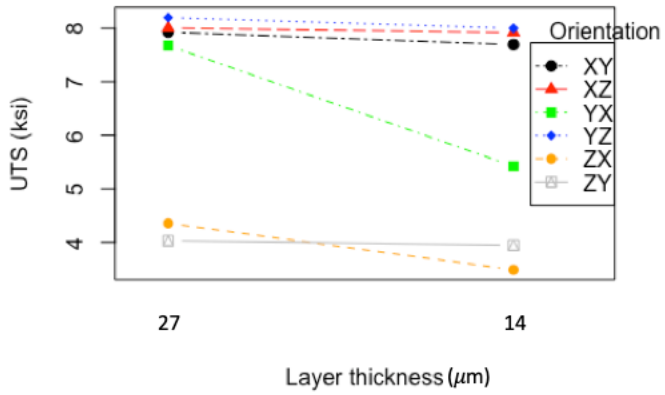

Figure 2.12 Interaction effect plots of orientation and layer thickness for UTS

Figure 2.13 shows the interaction effects of orientation and layer thickness for elongation. Significant interaction effects can be observed. For example, changing layer thickness from 14 μm to 27 μm did not cause observable changes in elongation for samples printed using orientations XY, YZ, ZX, and ZY. However, changing layer thickness from 14 μm to 27 μm caused significant change in elongation for samples printed using orientations XZ and YX.

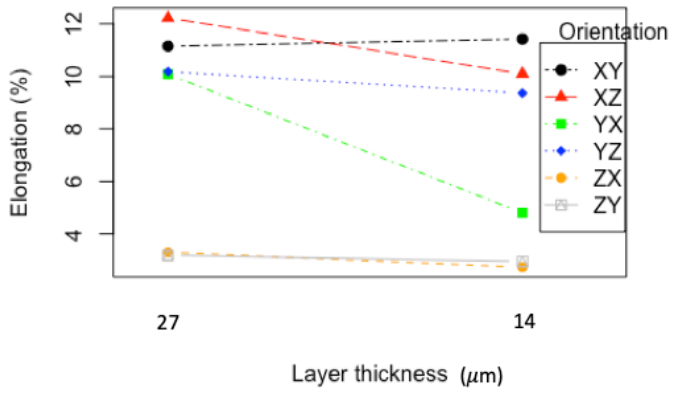

Figure 2.13 Interaction effect plots of orientation and layer thickness for elongation

2.3.4. ANOVA for orientation and layer thickness

Analysis of variance (ANOVA) was carried out to determine statistical significance of the differences caused by the two control factors: orientation and layer thickness. The ANOVA results are shown in Table 2.7, Table 2.8, and Table 2.9 for elastic modulus, UTS, and elongation, respectively. The main effects of orientation are significant for all mechanical properties, the main effects of layer thickness are significant only for UTS and elongation, and their interaction effects is also significant for all mechanical properties.

Table 2.7 Results of ANOVA for elastic modulus

	DoF	*Sum Sq*	*Mean Sq*	*F value*	*Pr(>F)*
Orientation	5	4.95E+9	9.91E+8	5.95	**0.0002**
Layer thickness	1	4.28E+6	4.28E+6	0.03	0.8733
Interaction	5	3.56E+9	7.13E+8	4.28	**0.0027**
Residuals	48	7.99E+9	1.66E+8		

Table 2.8 Results of ANOVA for UTS

	DoF	*Sum Sq*	*Mean Sq*	*F value*	*Pr(>F)*
Orientation	5	1.93E+8	3.86E+7	78.63	**<0.0001**
Layer thickness	1	5.79E+6	5.79E+6	11.79	**0.0012**
Interaction	5	9.07E+6	1.81E+6	3.70	**0.0065**
Residuals	48	2.36E+7	4.91E+5		

Table 2.9 Results of ANOVA for elongation

	DoF	*Sum Sq*	*Mean Sq*	*F value*	*Pr(>F)*
Orientation	5	724.0	144.8	276.15	**<0.0001**
Layer thickness	1	31.9	31.9	60.87	**<0.0001**
Interaction	5	51.8	10.4	19.74	**<0.0001**
Residuals	48	25.2	0.5		

2.4. Conclusion

The effects of two control factors, orientation and layer thickness, of Stratasys J750 PolyJet printer on mechanical properties (elastic modulus, ultimate tensile strength, and elongation) of printed samples were investigated. As to orientation, samples printed with their longest dimension aligned with the X axis had higher elastic modulus and elongation, samples aligned with the Y axis had higher UTS, and samples aligned with the Z axis had the lowest mechanical properties. With respect to layer thickness, it was found that larger layer thickness led to slightly higher elastic modulus, UTS, and elongation than smaller layer thickness. In short, the highest mechanical properties can be achieved by putting the longest dimension of a part along the X axis and the largest surface perpendicular to either the Y or Z axis.

2.5. References

[1] ASTM ISO/ASTM52900-15 Standard Terminology for Additive Manufacturing (2015), General Principles Terminology, ASTM International

[2] ASTM D638-14 Standard Test Method for Tensile Properties of Plastics (2014), ASTM International

[3] Stratasys PolyJet Materials Data Sheet

[4] Cazón, A., Morer, P., & Matey, L. (2014). PolyJet technology for product prototyping: Tensile strength and surface roughness properties. Proceedings of the Institution of Mechanical Engineers, Part B: Journal of Engineering Manufacture, 228(12), 1664–1675.

[5] Barclift, M. W., & Williams, C. B. (2012). Examining Variability in The Mechanical Properties of Parts Manufactured Via PolyJet Direct 3d Printing, 876–890.

[6] Mueller, J., Shea, K., & Daraio, C. (2015). Mechanical properties of parts fabricated with inkjet 3D printing through efficient experimental design. Materials and Design, 86, 902–912.

[7] Sugavaneswaran, M., & Arumaikkannu, G. (2015). Analytical and experimental investigation on elastic modulus of reinforced additive manufactured structure. Materials and Design, 66(PA), 29–36.

[8] Kęsy, A., & Kotliński, J. (2010). Mechanical properties of parts produced by using polymer jetting technology. Archives of Civil and Mechanical Engineering, 10(3), 37–50.

[9] Sai C. D., Rajesh R., & Murugan N. (2018). Effect of build orientation on the strength and cost of PolyJet 3D printed parts, Rapid Prototyping Journal

[10] Sugavaneswaran, M., & Arumaikkannu, G. (2014). Modelling for randomly oriented multi material additive manufacturing component and its fabrication. Materials and Design, 54, 779–785.

3. EXPERIMENTAL INVESTIGATION OF POLYJET 3D PRINTING PROCESS: EFFECTS OF FINISH TYPE AND SHORE HARDNESS ON DIMENSIONAL ACCURACY AND SURFACE FINISH OF POLYJET PROCESS

Paper title:

Experimental Investigation of Stratasys J750 PolyJet Printer: Effects of Finish Type and Shore Hardness on Surface Roughness

Experimental Investigation of Stratasys J750 PolyJet Printer: Effects of Finish Type and Shore Hardness on Dimensional Accuracy

Published in:

Proceedings of the ASME 2019 Manufacturing Science and Engineering Conference (MSEC 2019), June 10-14, 2019, Erie, Pennsylvania, USA

Authors' names:

Wei, X.[1], Bhardwaj, A.[1], Thakare, K.[1], Zeng, L.[2], Pei, Z.[1]

Authors' affiliations:

1. Department of Industrial and Systems Engineering, Texas A&M University, College Station, Texas 77843, USA
2. School of Data Science, City University of Hong Kong, Kowloon Tong, Hong Kong SAR, China

3.1. Introduction

3D printing, also known as additive manufacturing, is an emerging manufacturing method where a thin layer of material is selectively and repeatedly bonded together to form a 3D shape [1]. There are some obvious advantages that 3D printing possesses over traditional manufacturing methods: shorter lead-time, reduced tooling costs, freedom of part complexity, and reduced waste, to name a few. However, quality control has been a large factor that have hindered 3D printing from being broadly implemented in practice; it still has majority of occasions where it can only be used as a rapid prototyping method. The main reason of that is complicated phenomenon and abundant process parameters involved during the building process that affects a final quality of a 3D printed part. Although research community and commercial industry have been improving quality control aspects of 3D printing processes, and such efforts require further attentions.

In the reported studies of the PolyJet process, a lot of studies have been conducted to investigate the effects of process parameter on surface roughness. The examples of process parameters include layer thickness, finish type, Shore hardness, material combinations, orientation, and post-processing method. First, the effects of finish type on surface roughness are reviewed here. Kumar et al. considered three process parameters: finish type, orientation, and layer thickness. They developed a mathematical model to predict surface roughness, and their prediction errors were under 3 μm compared to the actual measurements [2]. Kechagias et al. also considered three factors that affect surface roughness: finish type, layer thickness, and sample size [3]. The results show that finish type significantly affects surface roughness, more than the other two factors. Cazon et al.

studied effects of orientation and finish type on surface roughness, and the effect of finish type is statistically significant [4]. Udroiu et al. measured vertical direction of samples printed using two finish types, and concluded that glossy finish produces lower surface finish than matte finish [5]. Despite the differences in printer and material used among the reported studies, there is a consensus that glossy finish leads to lower surface roughness than matte finish [2-5]. However, information on how Shore hardness, which is one of the unique process parameters exist for the PolyJet process, would affect surface roughness has not been studied in the literature at our best knowledge, and whether or not Shore hardness could have an interaction effect with finish type is unknown.

Abundant research has investigated dimensional accuracy of the PolyJet process. Kechagais et al. considered three factors: finish type, layer thickness, and sample size. They found that glossy finish led to better accuracies [2]. They also concluded that finish type plays a more significant role than layer thickness in the Z axis, but layer thickness is more significant in the X and Y axes. On the contrary, Yap et al. found that matte finish offers better dimensional accuracy because every surface of the part is covered with support materials to preserve its original geometry such that deviations from nominal dimensions are less [3]. Thakare et al reviewed literatures that studied dimensional accuracy related to PolyJet [9]. It was summarized that part orientation is control variable whose effects on dimensional accuracy has been studied the most in comparison to layer thickness, surface finish type or material. Out of the 37 related studies, 12 had evaluated the effect of process parameters on dimensional accuracy. The reported studies contain inconsistent results on which part orientation is better for dimensional accuracy. However,

the studies are consistent that smaller layer thickness gives better dimensional accuracy than the larger one. Additionally, glossy surface finish type is better than matte finish. Nevertheless, information on how Shore hardness would affect dimensional accuracy has not been studied in the literature, and whether or not Shore hardness could have an interaction effect with finish type is unknown.

In this study, the effects of the two process parameters, finish type and Shore hardness, on surface roughness and dimensional accuracy are investigated. The other process parameters, such as layer thickness, print orientation, and materials are kept constant. The rest of the paper is organized as follows. Experimental setups are described in the next section. Then, experimental results are summarized, and the effects of finish type and Shore hardness are discussed using main effects and interaction effects plots. Statistical analysis of the results is also presented by using analysis of variance (ANVOA) and pairwise comparison. The final section includes conclusions and future research directions.

3.2. Experimental Setup

3.2.1. Sample generation

Rectangular prism is designed to study the effects of finish type and Shore hardness on surface roughness and dimensional accuracy. The geometry of the prism was generated in SolidWorks with slightly different dimensions in each of three sides: 0.49″ in the X axis, 0.50″ in the Z axis, and 0.51″ in the Y axis. Here, the defined axes are corresponding to those set by the printer manufacturer; the X and Z axes are shown in

Figure 2.1 (a), and the Y axis is perpendicular to the surface of this paper. The file was exported as a binary STL file. Then, it was imported to the GrabCAD Print software in which the process parameters were assigned to the prisms.

3.2.2. Experimental conditions

A two factor design of experiment is conducted for this study, and selected levels for each control factors are presented in Table 3.1. For finish type, two options are available: glossy and matte. When glossy finish is selected, support materials will not cover the sample surfaces except for the bottom and overhanging surfaces. When matte finish is selected, support materials will cover all surfaces of the samples. For Shore hardness, four levels of Shore-A values out of available eight levels are selected. All the samples were produced by either model materials called VeroYellow RGD 836 or Agilus 30 FLX 935. VeroYellow is a rigid material whereas Agilus is a flexible rubber-like material. By depositing the two materials at different ratios, 8 different values of Shore hardness can be set through GrabCAD Print software. For example, Agilus is only used for generating samples of Shore hardness of 30, and VeroYellow is only used for making samples of Shore hardness of 100.

Table 3.1 Levels of control factors

Process Parameter	Level 1	Level 2	Level 3	Level 4
Finish type	Matte	Glossy	-	-
Shore hardness	30	50	85	100

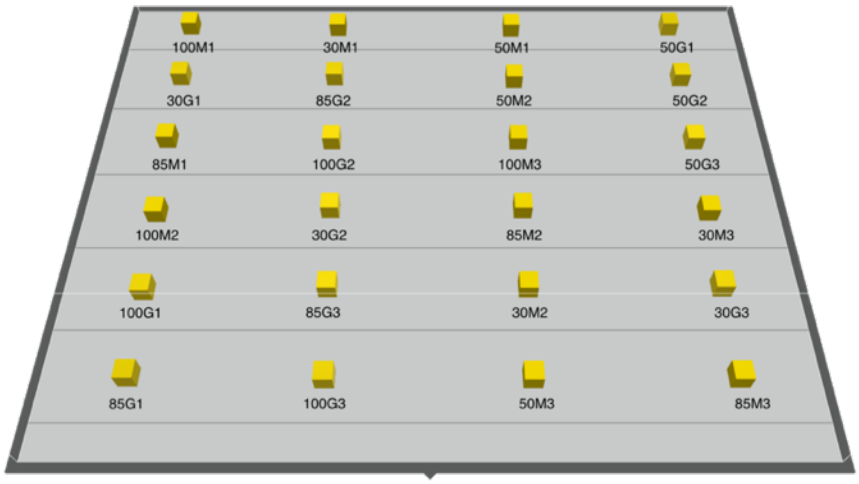

Figure 3.1 Sample locations on the build platform

Other process parameters were kept the same for all samples. Specifically, between the two types of available support materials, the wax-like SUP705 is harder than the gel-like SUP706 and thus not easily removed. Therefore, SUP706 was used in this study to reduce influence of support materials on surface quality. Larger layer thickness of 27 μm (900 dpi) was used, and the resolution of the printer in the XY plane is 42 μm (600 dpi) by default. The 8 treatments (i.e., 2 options of finish type combined with 4 options of Shore hardness) with 3 replications for each treatment were randomly placed on the build platform, as shown in Figure 3.1. Randomizing sample locations can eliminate or minimize potential confounding effects. Nomenclature of the samples used in Figure 3.1 is defined as follows: the number in front of the letter represents the value of Shore hardness. The letter designates the finish type used; “M” denotes matte finish, and “G” denotes glossy finish. The second number after the letter signifies sample identifications. For example, “50M1” indicates a Shore hardness of 50, matter finish and the first sample.

The samples were printed after 7 months of the machine installation, and maintenances such as cleaning were carried out on the daily basis.

3.2.3. Post-processing of samples

After the completion of a printing, gel-like support materials (SUP706) were manually removed by a scraper. Then, pressurized water was blasted to the samples to further remove the support materials. Caution has been taken while using the pressurized water because the high pressure could affect the surface finish. Also, it was optional to immerse the cleaned samples into caustic solution to further clean it, but immersing the samples for a long time may corrode it and make it brittle. Caustic solution was not used because it could affect the surface qualities of the samples.

3.2.4. Measurement of surface roughness

The samples were measured by Mitsutoyo surface roughness profilometer SJ-210 (Mitsutoyo, Japan). Table 3.2 shows parameter settings for the profilometer. ISO 1997 was selected as the standard, and arithmetic mean deviations of roughness (Ra) was obtained, and Gaussian filter was used. λc denotes the cut-off wavelength used to filter out higher frequencies of the primary profile. λs is the cut-off wavelength used to filter out lower frequencies of the measured profile. Hence, a roughness profile between the values of λc and λs is obtained. The measurement speed and the number of sampling length are set to 0.5 mm/s and 5, respectively. The type of detector used was standard drive unit in which the detector tip only moves in the axial direction. Measuring force of the detector was 0.75 mN.

Table 3.2 Parameter settings of Mitutoyo surface profilometer to measure Ra

Setting	**Value**
Standard	ISO 1997
Profile	Ra
Filter	Gaussian
λc	0.8mm
λs	2.5μm
Measuring speed	0.5 mm/s
Number of sampling lengths	5
Drive unit type	Standard
Detector type	0.75 mN

Figure 3.2 shows how the printed samples were measured by the profilometer. The sample was fixed by hand and the device was hold by a clamp. Human hand was used to fix the samples because the high friction of samples with low Shore hardness made it difficult to fix the samples by fixtures. The sequence of measurement was the same as the order of samples printed on the build platform, starting from top left to bottom right (Figure 3.1). Top surfaces of the samples were measured, in horizontal direction, which corresponding to the X axis direction of the printer. The moving direction of the detector tip was placed parallel to the direction of measurements before the measurement.

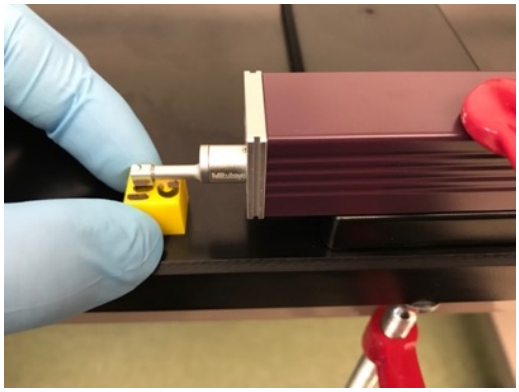

Figure 3.2 Surface roughness measurement by Mitsutoyo SJ-210

3.2.5. Measurement of dimensional accuracy

Figure 3.3 shows how printed samples were measured by Mitsutoyo digital caliper (Mitsutoyo, Japan). The sequence of measurement was the same as the order of samples printed on the build platform, starting from top left to bottom right (Figure 3.1). Each sample was held by an operator, and lengths along the X and the Y axes were measured at the center of each surface by the caliper. Thus, three measurements were obtained from each sample.

Figure 3.3 Dimensional measurement along the X axis for “100G1”

3.3. Results and Discussions

Table 3.3 presents measurement results for surface roughness of top surface and dimensions along the X and the Y axes. It can be observed that glossy finish has lower surface roughness than matte finish in both directions. Another trend is that surface roughness in horizontal direction is always lower than that in vertical direction. This is because the way that PolyJet process deposits the model materials creates peaks and valleys in horizontal direction. As a result, measurements in vertical direction need to traverse these grooves, while measurements in horizontal direction are parallel to either a peak or a valley and thus have lower surface roughness.

Table 3.3 Measurement results

Finish type	Shore hardness	Sample	Ra (μm)	Deviation in X (μm)	Deviation in Y (μm)
Matte	30	1	3.446	-25.4	-190.5
		2	3.522	50.8	-419.1
		3	2.965	114.3	-368.3
	50	1	3.539	-50.8	-101.6
		2	2.503	0.0	-12.7
		3	2.748	-38.1	0.0
	85	1	2.694	76.2	76.2
		2	2.325	76.2	88.9
		3	2.183	63.5	38.1
	100	1	1.860	406.4	152.4
		2	1.814	495.3	165.1
		3	1.670	342.9	114.3
Glossy	30	1	1.933	-12.7	-139.7
		2	2.163	-114.3	-88.9
		3	2.306	-190.5	-101.6
	50	1	1.984	-76.2	-38.1
		2	1.974	-25.4	-38.1
		3	1.871	-63.5	-50.8
	85	1	1.848	63.5	114.3
		2	1.658	63.5	114.3
		3	1.847	101.6	152.4
	100	1	0.645	25.4	50.8
		2	0.766	25.4	12.7
		3	0.693	25.4	25.4

3.3.1. Effects of finish type and Shore hardness on surface roughness

Figure 3.4 shows the main effect and interaction effect plots. From Figure 3.4(a) can be observed that surface roughness decreased as the value of Shore hardness increased. As for finish type, Figure 3.4(b) indicates that the means of surface roughness for glossy finish were lower than those of matte finish, which coincide with the conclusions in the literatures. Looking at the interaction effect plots of finish type and Shore hardness in Figure 3.4(c), the two lines are close to parallel, indicating that the interaction effects between the two factors are rather weak.

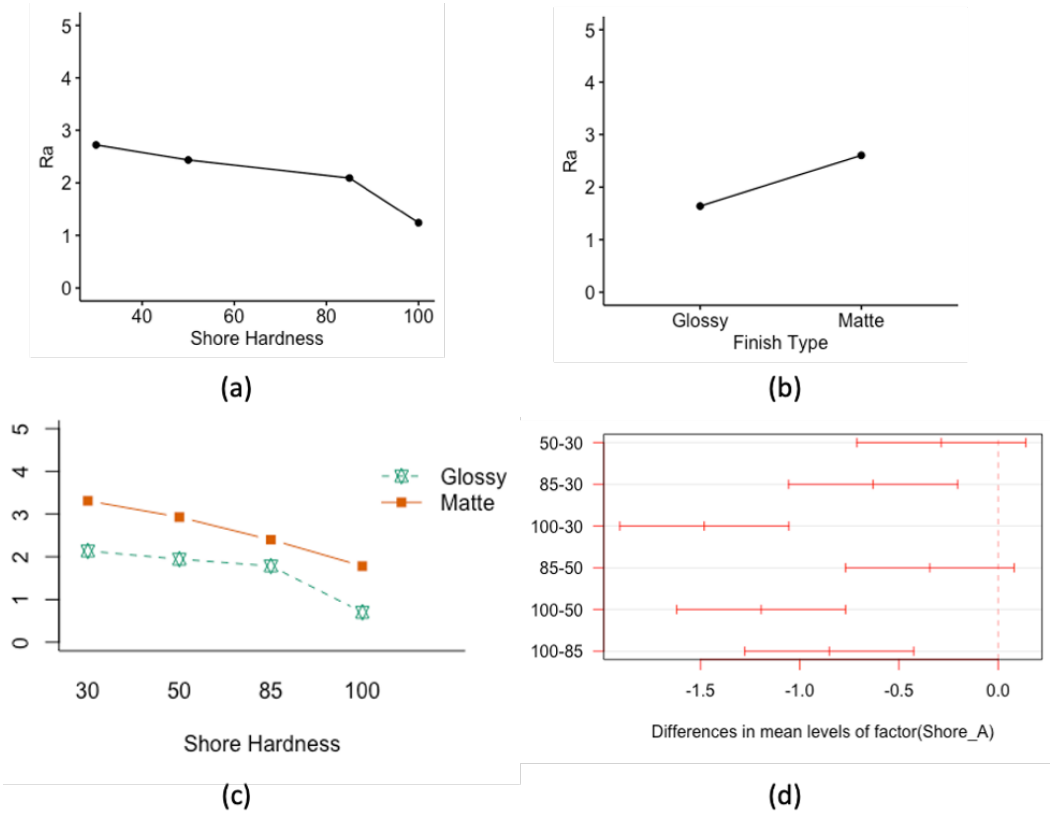

Figure 3.4 Main effect and interaction effect plots

ANOVA is carried out to determine the statistical significance of the differences caused by the two process parameters at the significance level $\alpha = 0.05$. Table 3.4 show the results of ANOVA. Based on the small p-values, the main effects of both factors are significant, while the interaction effects are not significant. Pairwise comparison was carried out for Shore hardness by Tukey honest significance test in order to understand which value of Shore hardness are different from another. Figure 3.4(d) shows that Shore hardness 100 are statistically different Shore hardness 85. However, Shore hardness 85 is not different from Shore hardness 50, and Shore hardness 50 is not different from Shore hardness 30. Therefore, Shore hardness 100 is the one that caused ANOVA to be significant.

Table 3.4 ANOVA for Ra

Source	*DoF*	*Sum Sq*	*Mean Sq*	*F Ratio*	*Pr(> F)*
Finish type	1	5.588	5.588	86.172	**<.001**
Shore Hardness	3	7.416	2.472	38.117	**<.001**
Interaction	3	0.270	0.090	1.390	0.282
Error	16	1.038	0.065		
Total	23	14.312			

3.3.2. Effects of finish type and Shore hardness on dimensional accuracy

Figure 3.5 shows the main effects of finish type for the X axis. According to Figure 3.5(a), it can be observed that Shore hardness 100 does not lead to the best accuracy in the X axis. Instead, Shore hardness of 30 had the smallest dimensional errors, and the actual dimensions in the X axis were larger than the nominal dimension as the value of Shore hardness increased. On the other hand, increases in dimensional accuracies can be seen with increasing Shore hardness value for the Y axis. Like the X axis, the larger value of

Shore hardness yielded oversized dimension than the nominal dimension for the Y axis, whereas the smaller value of Shore hardness led to undersized dimension than the nominal value. From Figure 3.5(b), it can be observed that glossy finish offers more accurate dimensions than matte finish, and the samples with matte finish have larger dimensions than the nominal value. On the other hand, Figure 3.6 (b) suggests that the means of the dimensions are almost identical regardless of the finish type for the Y axis.

Figure 3.5(c) and Figure 3.6(c) show the interaction effects of finish type and Shore hardness for the X and Y axes, respectively. It can be observed that significant interaction effects exist for the X axis. For example, changing finish type from matte finish to glossy finish increased dimensional accuracy for samples printed using Shore hardness of 100. However, changing finish type from matte finish to glossy finish does not affect dimensional accuracy for samples printed using Shore hardness of 50. Regarding the Y axis, it can be seen that significant interaction effects also exist. For example, changing finish type from matte finish to glossy finish increased dimensional accuracy for samples printed using Shore hardness of 30 and 100. However, changing finish type from matte finish to glossy finish decreased dimensional accuracy for samples printed using Shore hardness of 85.

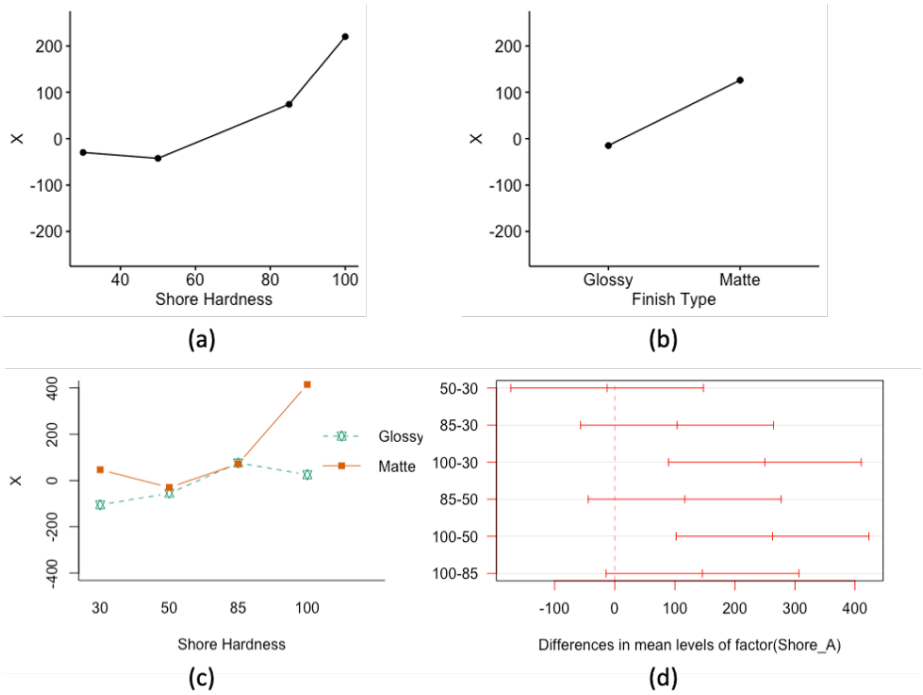

Figure 3.5 Main effect and interaction effect plots for X axis

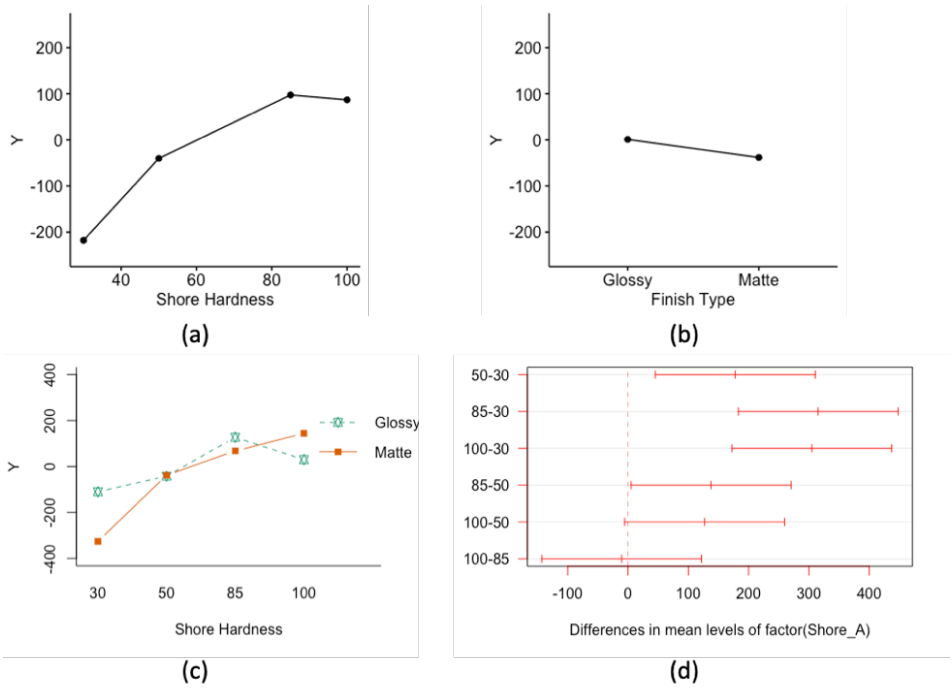

Figure 3.6 Main effect and interaction effect plots for Y axis

ANOVA was carried out to determine statistical significance of the differences caused by the two process parameters at the significance level $\alpha = 0.05$. Table 3.5 shows the results of ANOVA for the X and Y axes. Based on the small *p*-values, for the X axis, the mains effects of both process parameters are significant. The interaction effect is also significant. For the Y axis, finish type was not significant, but Shore hardness is, but its interaction with finish type is significant. Figure 3.5(d) shows that only Shore hardness of 100 was declared to be significantly different from Shore hardness of 50 and 30. Therefore, it reinforced the conclusion where smaller values of Shore hardness led to higher dimensional accuracy for the X axis. Figure 3.6(d) indicates that only Shore hardness of 85 is different from Shore hardness of 100, and thus, it can be concluded that Shore hardness of 50 statistically achieved the best dimensional accuracy in the Y axis.

Table 3.5 ANOVA for the X and Y axes

Source	*Axis*	*DoF*	*Sum Sq*	*Mean Sq*	*F Ratio*	*p-value*
Finish type	X	1	118877	118877	46.065	**<.001**
	Y		9200	9200	3.593	0.076
Shore hardness	X	3	265611	88537	34.308	**<.001**
	Y		388729	129576	50.606	**<.001**
Interaction	X	3	144482	48161	18.662	**<.001**
	Y		85611	28537	11.145	**<.001**
Error	X	16	41290	2581		
	Y		40968	2560		
Total	X	23	570260			
	Y		524508			

3.4. Conclusion

The effects of two process parameters, finish type and Shore hardness, on surface roughness and dimensional accuracy for PolyJet 3D printing process were investigated. It

was found that, with respect to finish type, samples printed using glossy finish had statistically lower surface roughness than matte finish, and glossy finish had more accurate dimensions than matte finish for the X and Y axes. That being said, matte finish is often unavoidable, especially for overhang structures. For Shore hardness, higher Shore hardness values have lower surface roughness, and larger value of Shore hardness led to better dimensional accuracy in the Y, whereas smaller value of Shore hardness provided more accurate dimension in the X axis. Also, as there were interaction effects between finish type and Shore hardness on surface roughness and dimensional accuracy. It can be concluded that the combination of glossy finish and Shore hardness 100 will achieve lowest surface roughness and highest dimensional accuracy.

3.5. References

[1] ASTM ISO/ASTM52900-15 Standard Terminology for Additive Manufacturing (2015), General Principles Terminology, ASTM International

[2] Kumar, K., & Kumar, G. (2015). An experimental and theoretical investigation of surface roughness of poly-jet printed parts: This paper explains how local surface orientation affects surface roughness in a poly-jet process. Virtual and Physical Prototyping, 10(1), 23–34.

[3] Kechagias, J., Iakovakis, V., Giorgo, E., Stavropoulos, P., Koutsomichalis, P., & Vaxevanidis, M. (2014). Surface Roughness Optimization of Prototypes Produced by PolyJet. An International Conference on Engineering and Applied Sciences Optimization.

[4] Cazón, A., Morer, P., & Matey, L. (2014). PolyJet technology for product prototyping: Tensile strength and surface roughness properties. Proceedings of the Institution of Mechanical Engineers, Part B: Journal of Engineering Manufacture, 228(12), 1664–1675.

[5] Udroiu, R., & Mihail, L. (2009). Experimental determination of surface roughness of parts obtained by rapid prototyping. Proceedings of the 8th WSEAS International Conference on Circuits, Systems, Electronics, Control & Signal Processing, 283–286.

[6] ISO/ASTM 52900:2015(E), Standard Terminology for Additive Manufacturing: General Principles and Terminology

[7] Kechagias, J., Stavropoulos, P., Koutsomichalis, A., Ntintakis, I., and Vaxevanidis, N. (2014), Dimensional Accuracy Optimization of Prototypes produced by PolyJet Direct 3D Printing Technology, Advances in Engineering Mechanics and Materials

[8] Yap, Y. L., Wang, C., Sing, S. L., Dikshit, V., Yeong, W. Y., & Wei, J. (2017), Material jetting additive manufacturing: An experimental study using designed metrological benchmarks, Precision Engineering, 50, 275–285.

[9] Thakare, K, Wei, X, and Pei, Z., 2019, “Dimensional Accuracy in PolyJet Printing: A Literature Review," Proceedings of the ASME 2019 14th International Manufacturing Science and Engineering Conference, MSEC2019-3018, V001T01A037.

4. EXPERIMENTAL INVESTIGATION OF POLYJET 3D PRINTING PROCESS: EFFECTS OF FINISH TYPE AND MATERIAL COLOR ON PRINTED COLOR

Paper title:

Experimental Investigation of PolyJet 3D Printing Process: Effects of Finish Type and Material Color on Color Appearance

Published in:

Proceedings of the ASME 2019 International Mechanical Engineering Congress & Exposition (IMECE-2019), November 11-14, 2019, Salt Lake City, Utah, USA

Authors' names:

Wei, X.[1], Zeng, L.[2], Pei, Z.[1]

Authors' affiliations:

1. Department of Industrial and Systems Engineering, Texas A&M University, College Station, Texas 77843, USA
2. School of Data Science, City University of Hong Kong, Kowloon Tong, Hong Kong SAR, China

4.1. Introduction

In material jetting additive manufacturing (AM) processes, droplets of material are selectively deposited [1]. Such processes include PolyJet by Stratasys (Eden Prairie, MN), MultiJet Printing (MJP) by 3D Systems (Rock Hill, SC), and Jet Fusion by HP (Palo Alto, CA). The latest Stratasys PolyJet printer features combinations of multi-colors and multi-material, which broadens the possibilities of 3D printing, especially for the purpose of prototyping.

An ability to fabricate full color objects helps product designers to create a prototype similar to an actual product. Naturally, it is desirable to have colors of the prototype as close to those of the actual product as possible. However, there are more factors involved in controlling color in a 3D printing process, compared to traditional 2D color printing [2]. Moreover, the framework for color 3D printers has not yet been established by the International Color Consortium because factors that affect the appearance of 3D printed objects still require further investigations [3].

Color appearances of 3D printed parts under different surface finishes have been studied. Wang et al. investigated a powder-based color 3D printing process [4]. They found that post-processing of 3D printed objects led to higher saturation and smaller chromatic aberration, and soakage increased brightness of the color surface. In addition, transparency of coating materials reduced surface roughness, and thus effectively enhanced color accuracy. Sun and Lai compared appearances of glossy and matte objects on RGB camera and established a regression model to estimate color differences of two objects [5]. Xiao and Brainard studied effects of glossy finish on color appearance of 3D

objects in 2D images [6]. They concluded that changing surface glossiness had only small effects on color appearance.

Effects of printing orientation on color appearance are also reported in the literature. Xiao et al. developed a multi-directional color management system based on printer RGB values and tristimulus values to minimize color variation across different orientations for a powder-binder based MJP [2]. Sun and Sie also developed a method for MJP to improve color uniformity across different orientations [7]. Ludwig et al. built a perceptual model of color uniformity for 3D printing. They found that color uniformity depends on orientations within the printer, and post-processing also plays an important role in color uniformity [8]. In short, although several studies investigated powder-based 3D printing processes, studies on how the PolyJet process affects color accuracy are not available in the literature. Therefore, the effects of two factors, finish type and material color, on color appearance of PolyJet printed parts are studied here.

The rest of the paper is organized as follows. Experimental setups are described in the next section. After that, experimental results are summarized, and the effects of finish type and material color are statistically tested. Post-hoc analysis is also performed, and the results are then compared with CIEDE2000 color differences, a popular formula to compare two colors. The final section includes conclusions and future research directions.

4.2. Experimental Setup and Procedure

4.2.1. Sample generation

A thin rectangular prism was designed for the study. The sample geometry was generated in Autodesk Fusion 360 with dimensions of 1″ in the X axis and the Y axis and 0.1″ in the Z axis. Here, the defined axes are corresponding to those set by the printer manufacturer; the X and Z axes are shown in Figure 2.1 (a). The Y axis is perpendicular to the XZ surface. The design file was exported as a STL file. Then, the STL file was imported to the GrabCAD Print software in which users can assign different finish types and material colors to the prisms.

4.2.2. Experimental conditions

Different levels selected for the two factors are presented in Table 4.1. For finish type, two levels are available: glossy and matte. When glossy finish is selected, support material will not cover the sample surfaces except for the bottom surface of the sample and the surfaces of overhanging structures. When matte finish is selected, support material will cover entire surfaces of the sample. For material color, four levels are selected: cyan, magenta, yellow and black.

Table 4.1 Selected levels for two factors

Factor	Level 1	Level 2	Level 3	Level 4
Finish type	Glossy	Matte	-	-
Material color	Cyan	Magenta	Yellow	Black

Other factors were kept constant for all samples. Two types of support materials are available for the PolyJet J750 printer: the wax-like SUP705 and the gel-like SUP706B.

SUP706B was used in this study to minimize the impact of support material on surface finish since SUP705 is more difficult to remove from printed samples. A layer thickness of 27 μm (900 dpi) was used, and the resolution of the printer in the XY plane was 42 μm (600 dpi) by default. “Natural shells” and “Natural texture” were selected as the color profile and texture profile, respectively. They dictate how the GrabCAD Print software convert RGB values to CMYK values with approximations because the CMYK system does not cover the full spectrum of colors of the RGB system [9].

Combinations of two finish type levels and 4 material color levels produced 8 unique treatments. Each treatment had 3 replicates, resulting in a total of 24 samples. These 24 samples were randomly placed on the build platform, as shown in Figure 4.1. Randomizing sample locations can eliminate or minimize potential confounding effects. Nomenclature of the samples used in Figure 4.1 was defined as follows: the first letter represents the finish type; “G” denotes glossy finish, and “M” denotes matte finish. The second letter signifies material color; “C” for cyan, “M” for magenta, “Y” for yellow, and “K” for black. The number after the letters is sample index. For example, “MC1” means the first replicate of matte finish and cyan color.

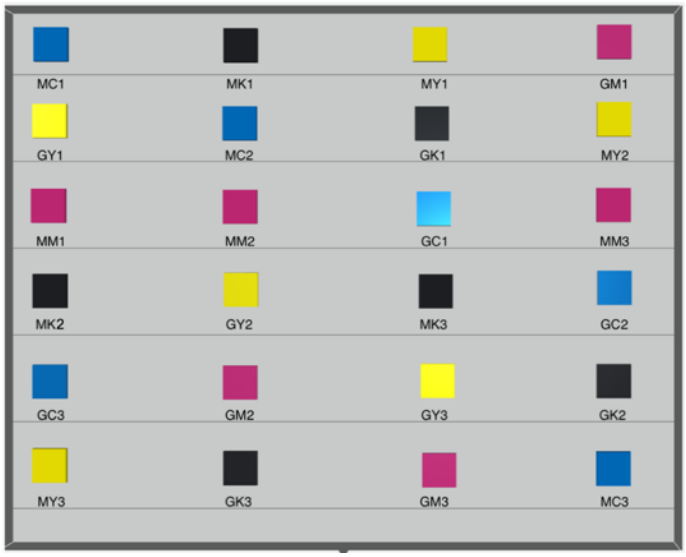

Figure 4.1 Sample locations on the build platform

The samples were printed after one year since the machine installation, and maintenances such as cleaning had been carried out on the daily basis. Right before the printing, cleaning wizard and head optimization were performed to reduce the amounts of color contaminations on the print head caused by previous prints.

4.2.3. Post-processing of printed samples

After the completion of printing, gel-like support material (SUP706B) on every surface of samples was manually removed using a scraper. Then, pressurized water was blasted to the samples to further remove the support material.

4.2.4. Measurement of color

The color of the samples was measured by a colorimeter, the Nix Pro color sensor (Nix Sensor, Ontario, Canada). Table 4.2 summarizes parameter settings of the color sensor. The illuminant used was D50 that emulates horizon daylight with a color temperature of 5000 Kelvin [10]. The receiver of the illuminant is called observer. It is

often set to 2° field of view because cones in fovea of human eyes also have 2° arc [10]. Here, both illuminant and observer are the sensor itself. The scanning area of the sensor is 15 mm^2. It measures reflectance factors to calculate the tristimulus values which are then converted to other color systems such as the CIELAB color system [11]. The CIELAB system was selected as the responses because it was known to have close matches with human vision. In this system, L* means lightness, a* denotes red (+) / green (−) value, and b* signifies yellow (+) / blue (−) value [12]. Figure 4.2 shows the actual samples and the sensor. The measurements were taken according to a random order specified in Table 4.3. Three measurements were taken on each sample. The average value of the three measurements was used as the reported color value for the sample.

Table 4.2 Parameter settings of Nix Pro color sensor

Parameter	**Value**
Illuminant	D50
Observer	2°
Scanning area	15 mm^2
Color system	CIELAB

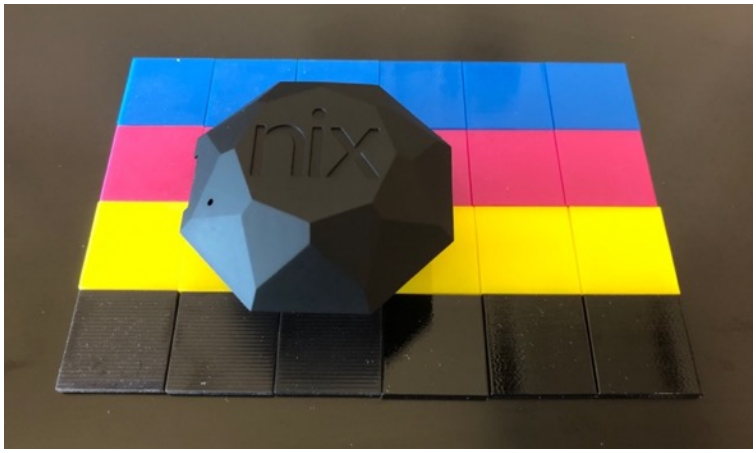

Figure 4.2 Nix Pro color sensor and printed samples

Table 4.3 Design matrix and measurement results

Test order	*Color*	*Finish*	*Replication*	*L*	*a*	*b*
2	Cyan	Matte	1	38.14	-7.54	-48.69
19			2	38.05	-7.32	-47.94
16			3	38.09	-7.16	-48.15
5		Glossy	1	35.44	-7.73	-50.34
14			2	35.46	-7.54	-50.91
20			3	35.50	-7.90	-50.70
3	Magenta	Matte	1	38.56	44.79	-10.97
7			2	38.46	45.15	-10.84
23			3	39.01	43.83	-10.76
4		Glossy	1	36.58	47.33	-10.91
8			2	36.38	48.88	-10.57
12			3	36.47	47.28	-11.04
9	Yellow	Matte	1	69.87	-9.75	66.59
15			2	69.31	-9.84	68.76
24			3	68.84	-9.69	67.43
21		Glossy	1	67.86	-8.74	76.08
6			2	68.15	-9.45	76.73
18			3	68.28	-9.52	77.08
1	Black	Matte	1	17.21	-0.98	-1.06
13			2	17.03	-1.04	-1.54
11			3	21.13	-1.01	-1.07
17		Glossy	1	10.66	-0.86	1.64
10			2	10.44	-0.75	1.23
22			3	10.22	-0.97	1.48

4.3. Results and Discussions

4.3.1. ANOVA for finish type and material color

Analysis of variance (ANOVA) was carried out for each CIELAB value to determine the statistical significance of the differences caused by the two factors at the significance level $\alpha = 0.05$. Table 4.4 shows the results of ANOVA for the CIELAB "L", "a", and "b". According to the p-values, the main effects of finish type and material color are significant; and the interaction effects of the two factors are also significant for all the three CIELAB values. Note that significance of the main effects of material color is obvious.

Table 4.4 ANOVA for CIELAB values

Source	*DoF*	*CIELAB*	*Sum Sq*	*Mean Sq*	*F Ratio*	*p-value*
Finish	1	*L*	74.41	74.413	102.15	<.0001*
		a	4.67	4.673	23.86	.0002*
		b	32.69	32.69	139.43	<.0001*
Color	3	*L*	8954.03	2984.676	4097.37	<.0001*
		a	12502.43	4167.475	21278.01	<.0001*
		b	46368.34	15456.11	65924.99	<.0001*
Finish*Color	3	*L*	41.92	13.972	19.18	<.0001*
		a	11.74	3.913	19.98	<.0001*
		b	109.09	36.36	155.10	<.0001*
Error	16	*L*	11.66	0.73		
		a	3.13	0.20		
		b	3.75	0.23		
Total	23	*L*	9082.01			
		a	12521.97			
		b	46513.88			

4.3.2. Main effects of finish type

Table 4.5 presents the results of measured CIELAB values under the two levels of finish type, where "Std. Err." is the standard error of all the measurements at the given

level of finish type. It can be observed that glossy finish has a lower "L" value (lightness) than matte finish on average. On the other hand, matte finish has lower "a" and "b" values compared to glossy finish. Figure 4.3 shows the main effects of finish type on "L", "a", and "b", respectively. The dot represents the mean of measured values at each level.

Table 4.5 Measured CIELAB values under two levels of finish type

Level	*L*		*a*		*b*	
	Mean	*Std. Err.*	*Mean*	*Std. Err.*	*Mean*	*Std. Err.*
Glossy	37.62	6.17	7.50	7.09	4.15	13.89
Matte	41.14	5.50	6.62	6.68	1.81	12.62

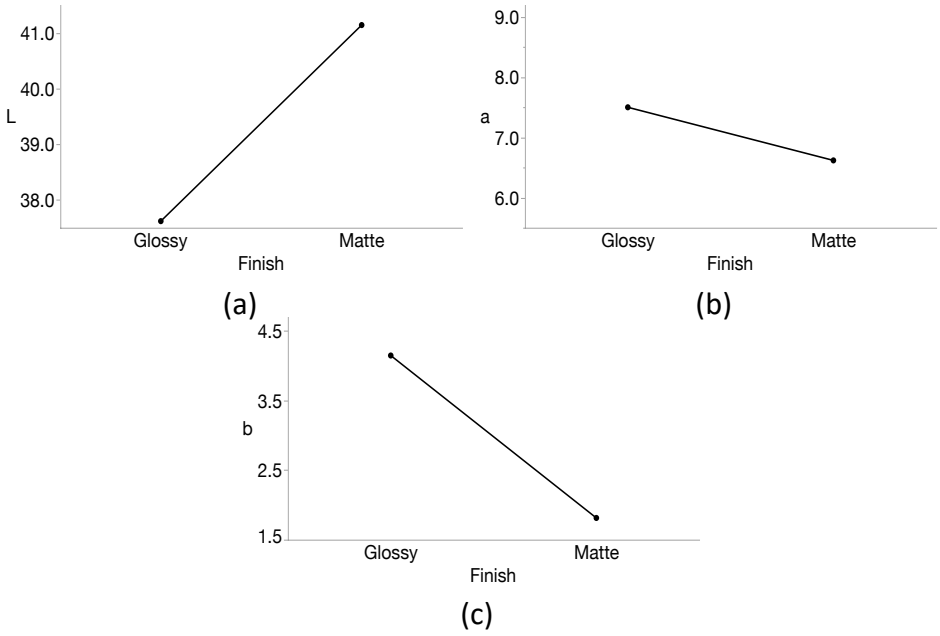

Figure 4.3 Main effects of finish type on CIELAB (a) L, (b) a, and (c) b values

4.3.3. Interaction effects of finish type and material color

Figure 4.4 shows the interaction effects of finish type and material color on "L", "a", and "b", respectively. For "L", the effects of finish type on black material is stronger than other three materials, which indicates the interaction effects. For "a", the effects of

finish type on magenta material is stronger than other three materials, which also suggests that the interaction effects between finish type and material color exists. The same observation can be made for "b" where the effects of finish type on yellow material is more prominent than other material colors.

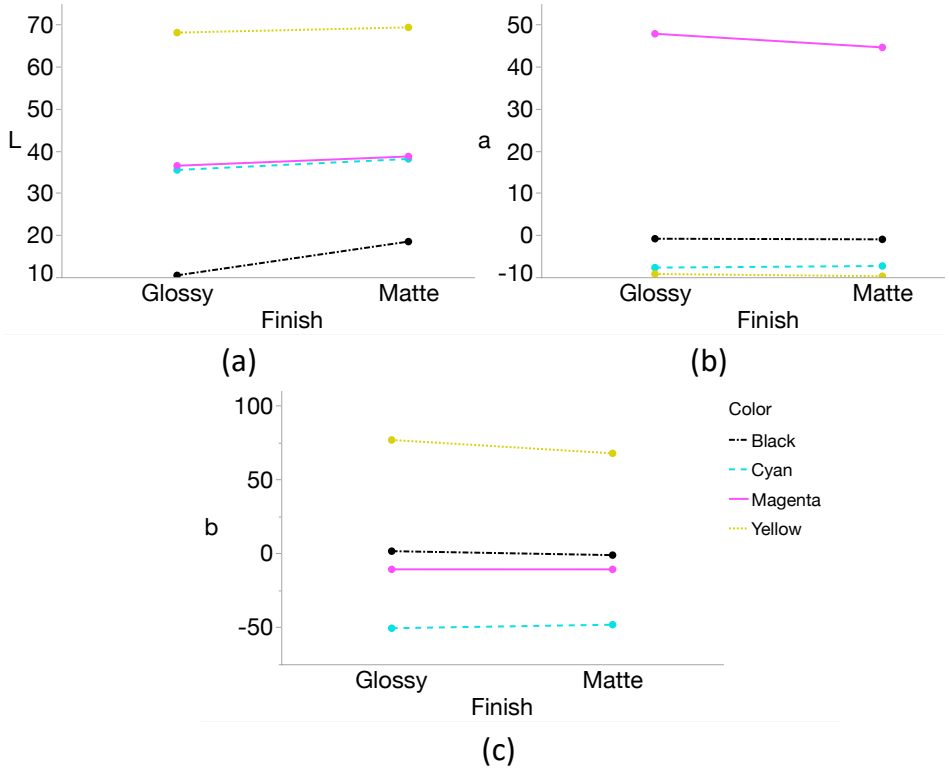

Figure 4.4 Interaction effects of finish type and material color on CIELAB (a) L, (b) a, and (c) b values

4.3.4. Pairwise comparisons for the CIELAB values

Interpretations from Figure 4.4 do not provide statistical significances of the means of the interaction effects. Alternatively, Tukey's honest significant difference (HSD) test can determine statistical significances of any pairs of means. Thus, it can be used to determine the effects of finish type on a CIELAB value for a given material color, and the

interaction effects of finish type and material color are effectively decomposed into three CIELAB values.

Table 4.6 summarizes the results of Tukey's HSD tests for four material color and three CIELAB values, where "Different" means that the effects of finish types on a CIELAB value are significantly different for a material color. The results for cyan material suggest that the finish types significantly affect the lightness component ("L" value) and the blue component ("b" value). Only the effects of finish type on red component ("a" value) is significant for magenta material, and the yellow component ("b" value) is significantly affected by the finish types for yellow material. Regarding black material, it is expected that only the lightness component ("L" value) plays a significant role because black should not possess any color component, but it turned out that the effects of finish type on "b" value is also significantly different.

Table 4.6 Tukey's HSD test for the interaction effects of finish type and material color

CIELAB	Cyan	Magenta	Yellow	Black
L (lightness)	●	○	○	●
a (red/green)	○	●	○	○
b (yellow/blue)	●	○	●	●

*●: Different, ○: Same

Two observations can be made by the results of Tukey's HSD. First, lightness component, namely "L" value is prone to be "Different" for darker color because the effects of finish type lead to larger contrast between glossy and matte finish. Second, color components, i.e., "a" and "b" values, tend to be "Different" for the color that are more representative of the color, e.g., "b" value for yellow because finish types particularly

affect such color components. To be aware of the effects of finish type on each CIELAB value for a material color can be beneficial for an observer of a 3D object.

4.3.5. Using CIEDE2000 to compare color differences

CIEDE2000 is the most accurate formula to calculate color differences between two colors [13]. While the above pairwise comparisons are conducted for each CIELAB value, this formula is introduced to combine all CIELAB values and to examine the effects of finish type on each material color. Table 4.7 summarizes the results of ΔE2000 (outputs from CIEDE2000). The mean values are the average of Delta E2000 from the 9 combinations of 3 replicates and 2 finish types. The small p-value suggests that at least one of the colors is significantly different from others. It is worth mentioning that a range from 1 to 2 in Delta E2000 indicates that the difference between the two colors is only perceptible through close observation, and a range from 2 to 10 indicates that the difference is perceptible at a glance [14]. Therefore, the difference between the two finish types for black can be detected at a glance, while the differences for other colors are not obvious without close looks. Figure 4.5 plots the means of Delta E2000 values for material colors. The dot represents the mean of Delta E2000 for the material color, and the vertical line gives the standard error.

Table 4.7 Delta E2000 for material colors

Color	*Mean*	*Std. Err.*	*p-value*
Cyan	2.33	0.02	
Magenta	2.18	0.11	<.0001
Yellow	2.52	0.11	
Black	5.88	0.38	

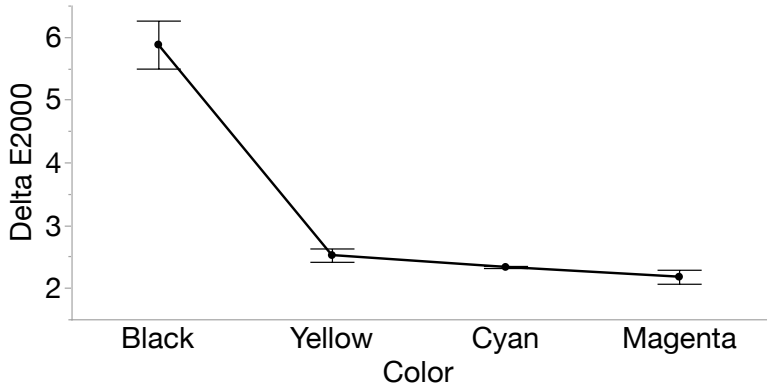

Figure 4.5 Effects of material color on Delta E2000

Similar to the previous section, significant differences of Delta E2000 in Table 4.8 only suggest that at least one of the means is different from other means. To find out which pairs mean of Delta E2000 differ from each other, Tukey's HSD tests were performed to Delta E2000, and summarized in Table 4.8. Small p-values indicate that the mean of Delta E2000 for black material is significantly different from those of other material colors. In other words, the effects of finish type on black material is statistically different from those on other material colors. Also, the effects of finish type between other material colors are not significant.

Table 4.8 Tukey's HSD test for all pairs of material colors

Color 1	*Color 2*	*Difference*	*Lower CL*	*Upper CL*	*p-value*
Black	Magenta	3.700	2.909	4.491	<.0001*
Black	Cyan	3.544	2.754	4.335	<.0001*
Black	Yellow	3.356	2.565	4.146	<.0001*
Yellow	Magenta	0.344	-0.446	1.135	0.644
Yellow	Cyan	0.189	-0.602	0.980	0.916
Cyan	Magenta	0.156	-0.635	0.946	0.950

4.3.6. Microscope images of the two finish types

Figure 4.6 compares top surfaces of glossy finish and matte finish through microscope with magnification of 10 using an Olympus microscope (Olympus BX51, Tokyo, Japan). It can be seen that glossy finish has smooth surfaces, while matte finish has repetitive lines with peaks and valleys. The characteristic of surface finish could play a significant role on how seriously support materials remain on the surface, and thus could affect reflectance and color appearances. It would be interesting to study if different post-processing methods change color appearances of the matte finish.

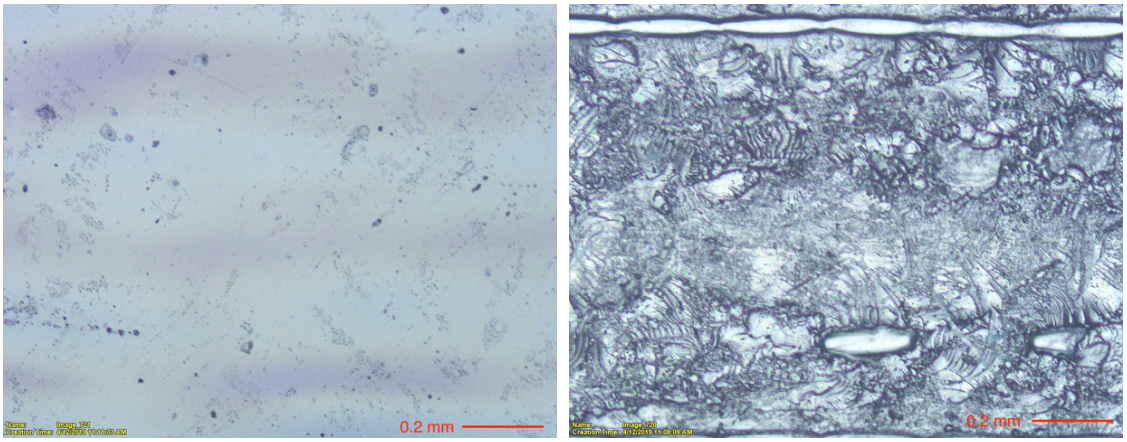

(a) (b)

Figure 4.6 Microscope images of surfaces of printed samples with black material using (a) glossy finish and (b) matte finish

4.4. Conclusion

In this study, the effects of two factors, finish type and material color, of Stratasys J750 PolyJet printer on color appearance of printed samples are investigated. It is found that both finish type and material color have significant effects on color appearance. Also, there are significant interaction effects of the two factors, which means that the effects of finish type on color appearance differ for different material colors.

4.5. References

[1] ASTM Standard 52900-15, 2015, "Standard Terminology for Additive Manufacturing - General Principles Terminology", ASTM International.

[2] Xiao, K., Sohiab, A., Sun, P., Yates, J., Li, C., and Wuerger, S., 2016, "A colour image reproduction framework for 3D colour printing," Advanced Laser Manufacturing Technology, vol. 10153, 1015318.

[3] Ronnenberg, M., and Farnand, S., 2019, "The Effect of Surface Texture on Color Appearance of 3D Printed Objects," Color Imaging Conference., vol. 2018, no. 1, pp. 128–133.

[4] Wang, X., Chen, C., Yuan, J., and Chen, G., 2019, "Color Reproduction Accuracy Promotion of 3D-Printed Surfaces Based on Microscopic Image Analysis," International Journal of Pattern Recognition Artificial Intelligence.

[5] Sun, P., and Lai, Y., 2017, "Estimating Appearance Differences of 3D Objects with an RGB Camera," Electron. Imaging, vol. 2017, no. 18, pp. 36–41.

[6] Xiao, B., and Brainard, D., 2008, "Surface gloss and color perception of 3D objects.," Visual Neuroscience., vol. 25, no. 3, pp. 371–385.

[7] Sun, P. and Sie, Y., 2017, “Color Uniformity Improvement for an Inkjet Color 3D Printing System,” Electron. Imaging, vol. 2016, no. 20, pp. 1–6.

[8] Ludwig, M., Moroney, N., Tastl, I., Gottwals, M., and Meyer, G., 2018, “Perceptual Appearance Uniformity in 3D Printing,” Electron. Imaging, vol. 2018, no. 8, pp. 209-1-12.

[9] Adjusting print settings, 2019, “Print settings for PolyJet printers”, GrabCAD, Available: https://help.grabcad.com/article/226-adjusting-print-settings#pj.

[10] Measure What You See, 2014, “Understanding CIE Illuminants and Observers”, WordPress.com, Available: https://measurewhatyousee.com/2014/10/10/understanding-cie-illuminants-and-observers/.

[11] Knowledge Base, 2019, “How do you Measure Color Accuracy?”, Nix color sensor, Available: https://www.nixsensor.com/measure-color-accuracy/.

[12] Paravina, R., 2018, “Understanding Color,” Ronald E. Goldstein’s Esthetics in Dentistry, pp. 270–294.

[13] Luo, M., Cui, G., and Rigg, B., 2001, “The development of the CIE 2000 colour-difference formula: CIEDE2000,” Color Research and Application, vol. 26, no. 5, pp. 340–350.

[14] Schuessler, Z., 2016, “Defining Delta E”, Delta E 101, Available: http://zschuessler.github.io/DeltaE/learn/.

5. POLYJET 3D PRINTING: PREDICTING COLOR BY MULTILAYER PERCEPTRON NEURAL NETWORK

Paper title:

PolyJet 3D Printing: Predicting Color by Multilayer Perceptron Neural Network

Published in:

Accepted by Annals of 3D Printed Medicine

Authors' names:

Wei, X.[1], Zou, Na[2], Zeng, L.[3], Pei, Z.[1]

Authors' affiliations:

1. Department of Industrial and Systems Engineering, Texas A&M University, College Station, Texas 77843, USA
2. Department of Engineering Technology and Industrial Distribution, Texas A&M University, College Station, Texas 77843, USA
3. School of Data Science, City University of Hong Kong, Kowloon Tong, Hong Kong SAR, China

5.1. Introduction

Medical models are physical models of anatomical structures such as skull and heart. They can be used for surgical simulation and planning in complex operations such as craniofacial surgeries, and for anatomy teaching in medical curricula. Medical models are traditionally made by plaster casting, and have recently been fabricated by 3D printing in some cases [1].

3D printing fabricates an object by selectively and repeatedly stacking materials layer by layer [2]. Color of 3D printed objects had been limited to the color of material itself in the past, until full color 3D printing became available. Color accuracy of 3D printed objects is important. For example, when 3D printing is used to produce medical models, it is desirable that 3D printed anatomies have the color as close to real anatomies as possible. Such precise representations of colors could enhance effectiveness of medical models used in surgical planning and medical education. In addition, when 3D printing is used for product prototyping, the ability to precisely represent the color of 3D printed objects is needed to determine the final color of designed products used for mass production. Furthermore, when 3D printing is used for making final products, the color of printed products has psychological effects on users' perception, and an inaccurate color representation can significantly change the attractiveness and impression of the products.

Figure 5.1 schematically illustrates PolyJet 3D printing. Stratasys J750 PolyJet printer (Minnesota, USA) is one of the commercially available full color 3D printers. Two types of photocurable resins in liquid form, base model material and support material, are deposited from the print heads. The base model materials are used to construct the object,

while the support material is used to build foundations to temporarily support some of the base model material after being deposited. The print heads move in both X and Y directions, and selectively jet materials according to the design of the object. The X and Z axes are shown in Figure 5.1; and the Y axis is perpendicular to the XZ plane. After each layer is printed and cured by UV lamps attached to both sides of the print heads, the build platform goes down by a distance equal to one layer thickness, and the next layer of materials are deposited. These steps are repeated until the object is completed. There are two types of surface finish (finish type): glossy and matte. When the glossy finish type is selected, the support material covers only the bottom surfaces (as well as the surfaces of overhangs) of the printed object. When matte finish type is selected, support material covers all surfaces of the printed object.

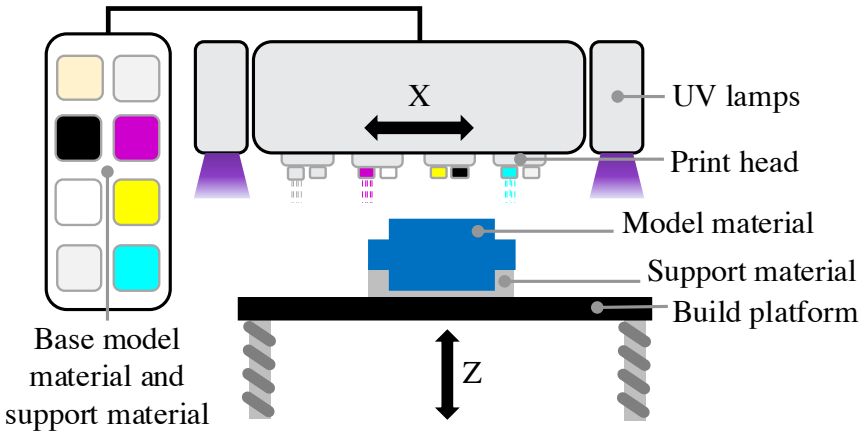

Figure 5.1 Illustration of PolyJet 3D printing

PolyJet can theoretically produce the full range of color. It places multiple base model materials (e.g., cyan and yellow) close to each other to make any color other than

the colors of base model materials [3]. To print full color, users can specify the color of a printed object using the RGB color system in the printer software. In the RGB color system, a color is represented by three integers, R, G, and B, each ranging from 0 to 255. For example, the pure black color is (0,0,0), and the pure white color is (255, 255, 255). In this paper, the measured RGB values (R_m, G_m, B_m) of a printed sample refer to the RGB values measured by a colorimeter on the printed sample, and the specified RGB values (R_s, G_s, B_s) for a printed sample are entered by the user in the printer software. Table 5.1 displays some data of specified RGB values and measured RGB values of samples printed by the Stratasys J750 PolyJet printer installed in the authors' lab. The data in the table show that the measured color of a printed sample does not always match the specified color of the sample very well.

Table 5.1 Comparison of specified RGB values and measured RGB values

Color	*Specified*			*Measured*		
	R_s	G_s	B_s	R_m	G_m	B_m
Black	0	0	0	26	28	26
White	250	250	250	198	211	213
Red	250	0	0	161	80	33
Green	0	250	0	123	174	47
Blue	0	0	250	72	63	125
Cyan	0	250	250	97	182	181
Yellow	250	250	0	195	194	32
Magenta	250	0	250	180	78	142

Table 5.2 summarizes reported studies regarding color of printed objects by PolyJet 3D printers. These studies cover a wide range of topics, from effects of control factors (finish type, sample thickness, etc.) on measured color, to methods for improving accuracy of color texture reproduction, to development of more accurate color

measurement techniques. A machine learning technique is also applied to predict relationships between control factors and mechanical properties of PolyJet printed anatomical models [4]. However, there is a lack of reports on the relationships between measured color and control factors (e.g., specified color and finish type) for PolyJet. This paper addresses the knowledge gap in the literature. The authors' preliminary study uses the conventional regression models, i.e., linear regression and cubic regression, to predict relationships between measured color and control factors (the results are presented in Section 5.4 Results and Discussion), but shows that the prediction accuracies are not satisfactory. It has been reported that applications of machine learning in 3D printing can produce positive results in process optimization, in-situ monitoring, and quality control [5-7]. Therefore, this study mainly reports the development of a multilayer perceptron (MLP) neural network model for the relationships between measured color and control factors. This model can be used to predict the color of a printed object with high accuracy.

Table 5.2 Summary of reported studies regarding color of printed objects by PolyJet

Topic	*Method*	*Ref.*
Main effects of finish type, and interaction effects between finish type and specified color on measured color	Experiment	[8]
Characterization of achievable range of color	Experiment	[9]
Effects of printed sample thickness on measurement of hue, brightness, and saturation	Experiment	[10]
Effects of subsurface structure on color appearance	Experiment	[11]
Establishment of a framework in color measurement of translucent resin to substitute traditional spectrophotometers	Modeling	[12,13]
Development of a compensation method to produce high-frequency color texture for translucent resin	Modeling	[14]
Controlling material placements along the layer stacking direction to achieve spatially varying color and translucency	Modeling	[15,16]
Adjusting subsurface material placements to smooth out color boundaries	Modeling	[17]

The rest of the paper is organized as follows. Section 5.2 describes the experimental design and setups used to collect experimental data. Section 5.3 presents the architecture of the multilayer perceptron neural network (MLP) model, as well as optimization algorithm and training strategy. Section 5.4 firstly shows the trends and correlations of the experimental data, and then compares the prediction performances of the MLP model and two alternative models, the linear regression model and the cubic regression model. Finally, Section 5.5 provides conclusions and directions of future research.

5.2. Experimental Procedure and Data Collection

5.2.1. Experimental design

A full factorial design of experiments is used to investigate four control factors related to measured color: specified RGB values (R_s, G_s, B_s) and finish type. Table 5.3 shows the selected levels for the four control factors. Six levels are selected for each of the specified RGB values, ranging from 0 to 250 with 50 increments. Both glossy and matte finish types are examined. Therefore, there is a total of 432 unique combinations from these four control factors, resulting in 432 experimental conditions. Under each experimental condition, only one sample is printed because a previous study [5] shows that the differences in measured RGB values for replicated samples are negligible.

Table 5.3 Control factors and their selected levels

Control factor	*Levels*
R_s	0, 50, 100, 150, 200, 250
G_s	0, 50, 100, 150, 200, 250
B_s	0, 50, 100, 150, 200, 250
Finish type	Glossy, Matte

5.2.2. Preparation of printed samples

The samples are printed on a Stratasys J750 PolyJet printer. The shape of the samples is a thin square plate with dimensions of 20 mm in the X and Y axes, and 2 mm in the Z axis. The designed STL file is generated in Autodesk Fusion 360 (California, USA), and imported to the Stratasys GrabCAD Print (Minnesota, USA) software of the printer. The specified RGB values and finish type are entered in the software. All samples are printed in glossy finish type. The bottom sides of the samples are used to obtain experimental data for matte finish type. Therefore, a total of 216 samples are printed for

the 432 experimental conditions. The layout of the samples on the build platform is shown in Figure 5.2.

Figure 5.2 Printed 216 samples and their layout on the build platform.

The combinations of a color profile and base model materials determine the range of achievable color of a printer [18]. A color profile in full color 3D printing converts RGB values used in digital monitors to CMYKW (abbreviation for cyan, magenta, yellow, black, and white) values used in physical printers [18]. In this study, “Natural shells” is set as the color profile. The following five types of base model materials are used: VeroPureWhite (RGD837), VeroBlackPlus (RGD875), VeroCyan (RGD843), VeroYellow (RGD836), and VeroMagenta (RGD851). Gel-like support material (SUP706B) is used as the support material, and the layer thickness is set as 27 μm. The samples are printed after one year since the printer’s installation in the lab, and regular maintenance such as cleaning has been carried out according to the maintenance manual of the printer. Right before the printing, cleaning wizard and head optimization are performed to eliminate or reduce potential color contamination caused by previous

printing. After the completion of printing, the support materials on the bottom sides of the samples are manually removed using a scraper. Then, pressurized water is blasted to the samples for further removal of the support material.

5.2.3. Measurement of color

Nix Pro colorimeter (Ontario, Canada) is used to measure the RGB values on the printed samples. Illuminant and observer are two parameters that need to be set for the colorimeter [19]. The illuminant used is D50 that emulates horizon daylight with a color temperature of 5000 Kelvin [20]. The observer (receiver of the illuminant) is set to 2° field of view, corresponding to the angle of cones in fovea of human eyes. For each experimental condition, three measurements are taken from the sample surface by the colorimeter, and the average of the three measurements is reported as the measured RGB values.

5.3. Multilayer Perceptron Neural Network

5.3.1. Model architecture

A neural network, formally called artificial neural network, is an interconnected group of artificial neurons, each of which functions as a mathematical operator to mimic the function of a biological neuron [21]. A network has multiple layers, including an input layer, an output layer, and one or multiple hidden layers in between. Each layer consists of a number of neurons. The connections between neurons at different layers are called edges. Each neuron has its own inputs and an output, where the inputs are weighted and then converted to an output through an activation function. As the activation function is

nonlinear, a neural network model can estimate nonlinear relationships between input variables and output responses. Multilayer perceptron (MLP) [22] is a widely used class of neural network model, which has a fully connected model architecture, meaning that every neuron in one layer, except the last layer, is connected to all the neurons in the next layer.

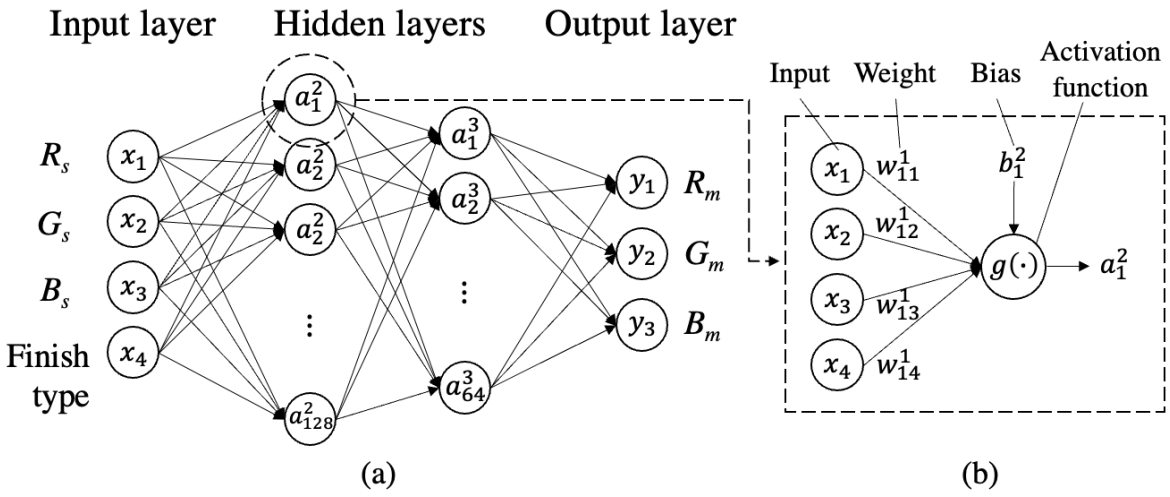

Figure 5.3 The developed multilayer perceptron neural network model: (a) overall model architecture, and (b) the relationship between input variables and the 1st neuron of the second layer

MLP is employed in this study to estimate relationships between control factors and the measured color of printed samples by PolyJet. The developed MLP model has four layers, i.e., one input layer, two hidden layers, and one output layer, as illustrated in Figure 5.3(a). There are 4 neurons in the input layer, $\{x_1, x_2, x_3, x_4\}$, corresponding to the four control factors (i.e., the specified RGB values R_s, G_s, B_s and finish type), and 3 neurons in the output layer, $\{y_1, y_2, y_3\}$, corresponding to the measured RGB values R_m, G_m, B_m. The second layer has 128 neurons, and the third layer has 64 neurons. When selecting the

number hidden layers and the number of neurons in each layer, there is a trade-off between model prediction accuracy and model training time. For example, it is preferred to have a large number of neurons, so the model can have more flexibility to adapt to the complex relationships between inputs and outputs. But, the training time would be too long if the number is too large. The number of hidden layers and the number of neurons used in this study are able to achieve a good balance.

In this model, the i^{th} neuron, $i = 1, \dots, 128$, in the second layer is calculated by

$$a_i^2 = g\left(\sum_j w_{ij}^1 x_j + b_i^2\right) \tag{1}$$

where $g(\cdot)$ is the rectified linear unit (ReLU) activation function, which takes a form of $g(z) = \max\{0, z\}$. w_{ij}^1 is the weight allocated to the edge between the j^{th} input and the i^{th} neuron, and x_j, $j = 1, \dots, 4$, is the j^{th} input. b_i^2 is the bias assigned to the neuron. The superscripts are the layer indices. To show the idea more clearly, Figure 5.3(b) schematically illustrates the steps involved in the calculation process using a_1^2 as an example. Essentially, a neuron in the second layer is obtained by first weighting the inputs, adding a bias, and then applying the activation function to the linear combination of the inputs. Similarly, a neuron in the third layer is calculated by

$$a_i^3 = g\left(\sum_j w_{ij}^2 a_j^2 + b_i^3\right) \tag{2}$$

where a_i^3, $i = 1, \dots, 64$, is the i^{th} neuron in the third layer, and a_j^2, $j = 1, \dots, 128$, is the j^{th} neuron in the second layer. Lastly, an output response in the output layer is calculated by

$$y_i = \sum_j w_{ij}^3 a_j^3 + b_i^4 \tag{3}$$

where y_i, $i = 1, 2, 3$, is the i^{th} output response, and a_j^3, $j = 1, \ldots, 64$, is the j^{th} neuron in the third layer. Note that the activation function is not applied at the output layer.

Using the collected experimental data, the MLP model is trained to estimate parameters in the model, including all the weights and biases in Equations (1) - (3). The trained model is then used to predict the color of a printed sample given a set of values for the control factors.

5.3.2. Optimization algorithm

The weights and biases in Equations (1) - (3) are obtained through an optimization algorithm. In this study, the adaptive moment estimation (ADAM) algorithm [23] is used, which is more efficient than the commonly used stochastic gradient descent algorithm [22]. It is also robust to the choice of hyperparameters. The learning rate in the algorithm is set to 0.01.

The initial values of the weights and biases are randomly generated. Then, the MLP model is trained by iteratively adjusting the weights and biases to minimize a loss function. In this study, the loss function used is the mean squared error (MSE), defined as the average of squared errors between predicted color and observed color,

$$MSE = \frac{1}{3k} \sum_k \sum_i (y_{ik} - \hat{y}_{ik})^2 \tag{4}$$

where y_{ik} is the i^{th} measured RGB values observed, $i = 1, 2, 3$, under the k^{th} experimental condition, and $\hat{y}_{ik}$ is the corresponding measured RGB values predicted from the MLP model.

5.3.3. Training strategy

Cross validation is used to assess the prediction performance of the MLP model. In a K-fold cross validation, the entire dataset is randomly and evenly split into K folds. In each iteration, one fold is held out as testing data, and the remaining folds are used to train the MLP model. Then, the trained model is used to make predictions using the conditions under which the testing data are obtained. Afterwards, the prediction error (i.e., deviation of predicted values from the testing data) is calculated. This process is repeated until every fold has been used as the testing data. The overall prediction performance of the MPL model is represented by the average of the K prediction errors. In this study, a 5-fold cross validation is used, and the 432 observations are divided into 5 folds. In each set of training data, training data is further split into a training set and a validation set. The training set is used to update weights and biases, and the validation set is used to calculate training error (MSE) [22]. 20% of the training data is allocated to validation set for each of the 5 folds of training data. Data normalization is applied to the entire dataset. The epochs (training iterations) are set to 100 since prediction accuracies are not improved after tens of epochs. The batch size (number of observations used to train the model at a time) of 32 is used [22].

Overfitting refers to a situation where a model performs well on validation set, but poorly on testing data [22]. Dropout is an effective regularization strategy to alleviate model overfitting [22]. Specifically, in each epoch, some randomly selected neurons are not updated during that epoch in order to reduce training bias and prevent the model from

being stuck in a local optimum. The dropout rate is set to 0.1 in the two hidden (second and third) layers.

5.3.4. Prediction performance

To quantify the performances of the trained MLP model, two measures are calculated: mean absolute error (MAE) and coefficient of determination (R^2). MAE [24] is defined as

$$MAE = \frac{1}{3k}\sum_k \sum_i |y_{ik} - \hat{y}_{ik}| \tag{5}$$

where y_{ik} is the i^{th} measured RGB values, $i = 1, 2, 3$, of k^{th} observation of the experimental condition, $k = 1, \dots, 432$. MAE is an average of the absolute differences (errors) between prediction and observation. R^2 is defined as

$$R^2 = 1 - \frac{RSS}{TSS} = 1 - \frac{\sum_k (y_{ik} - \hat{y}_{ik})^2}{\sum_k (y_{ik} - \bar{y}_i)^2} \tag{6}$$

where RSS is the residual sum of squares, and TSS is the total sum of squares. Coefficient of determination (R^2) [24] ranges from 0 to 1, indicating what proportion of variances in data can be explained by a model. A small MAE and a large R^2 usually mean that a model has good prediction performance.

It is also worth mentioning that training and testing results of the MLP model may vary in different runs, even if the same sets of training and testing data are used. When the training and testing data are split, the same split is insured every run by using the same random seed. However, random seeds are not fixed for the random numbers used in dropout and ADAM algorithm. As a result, the numbers shown in Table 5.5 could change for a different run, but the overall trends of the results are consistent.

5.4. Results & Discussion

This section presents and discusses the experimental and computational results. First, data trends of the experimental results are visualized by boxplots, and Pearson correlation coefficients are utilized to understand relationships between measured color and control factors. Second, prediction performances of the trained MLP model are assessed and compared with those of a linear regression model and a cubic regression model.

5.4.1. Characteristics of experimental results

The boxplots in Figure 5.4 show the trends between the measured RGB values and the specified RGB values. Each boxplot contains 72 data points, all of which have the same value for one of the specified RGB values (R_s, G_s, or B_s). For example, the boxplot of R_m given $R_s = 0$ in Figure 5.4(a) is plotted using all the measured R_m values from all the experimental conditions when R_s is 0, including both finish types. Hereafter, the six selected levels of each specified RGB value (i.e., from 0 to 250) are divided into three ranges, referred to as lower (0 and 50), middle (100 and 150), and upper (200 and 250) ranges, respectively. It can be noticed in Figure 5.4(a) that when R_s takes the values in lower or upper ranges (especially 0 and 250), the difference between R_s and R_m is larger. If R_s spans in the middle range (e.g., 150), the difference between R_s and R_m is smaller. Similar observations can be made for G_s and B_s, as shown in Figure 5.4(b) and (c). When specified RGB values are close to the upper and lower ranges, the differences between measured RGB values and specified RGB values are larger; when specified RGB values

are in the middle range, the differences are smaller. In other words, there are nonlinear trends between the measured RGB values and the specified RGB values.

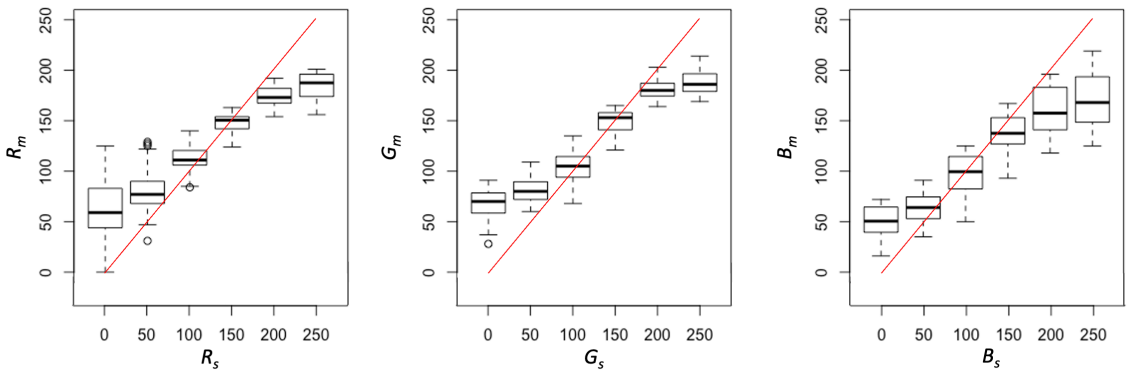

(a) (b) (c)

Figure 5.4 Boxplots of measured RGB values for each of the specified RGB values, (a) R_s vs. R_m, (b) G_s vs. G_m, and (c) B_s vs. B_m.

To check the correlation between control factors and measured RGB values, Pearson's correlation coefficients [23] are calculated and presented in Table 5.4. The coefficient values range from -1 to 1, where -1 indicates that the two variables are perfectly negatively correlated, and 1 means that they are perfectly positively correlated. The corresponding *p*-values are presented next to the coefficient values. The smaller a *p*-value is, the more statistically significant the correlation between the variables is. It can be observed that multiple specified RGB values are correlated with the measured RGB values, and the effects of finish type on measured RGB are different. For example, R_m is significantly and positively correlated with R_s and G_s, and the magnitude of correlation coefficient for R_s is much larger. The absolute value of the correlation coefficient between finish type and R_m is the smallest, compared with the correlations of finish type with G_m

and B_m. In fact, negative sign of the coefficient value means that glossy finish type tends to cause lower measured RGB values than matte finish type.

Table 5.4 Correlation coefficients between control factors and measured RGB values

	Correlation coefficient (p-value)			
	R_s	G_s	B_s	*Finish type*
R_m	0.930 (0.001)	0.155 (0.001)	-0.051 (0.289)	-0.054 (0.262)
G_m	0.065 (0.181)	0.950 (0.001)	-0.003 (0.957)	-0.089 (0.064)
B_m	-0.007 (0.892)	0.056 (0.246)	0.907 (0.001)	-0.157 (0.001)

In short, Figure 5.4 and Table 5.4 suggest that there are nonlinear trends between measured RGB values and specified RGB values, and more than one control factors are correlated with each of the measured RGB values. Therefore, a complex model such as MLP would be more suitable for predicting measured RGB values than simple models such as a linear regression model.

5.4.2. Prediction performances of the MLP model

In Figure 5.5, measured RGB values observed (experimental data) are plotted against measured RGB values predicted by 5-fold cross validation using the MLP model. There are 432 points in each plot because 5-fold cross validation allows all the experimental data to be treated as testing data (one fifth of the data are used as the testing data in each validation). The prediction performance is the best if all the points fall on the red line. It can be seen that the predicted R_m, G_m, and B_m are fairly close to the observed ones, indicating that the overall prediction performance of the MLP model is good.

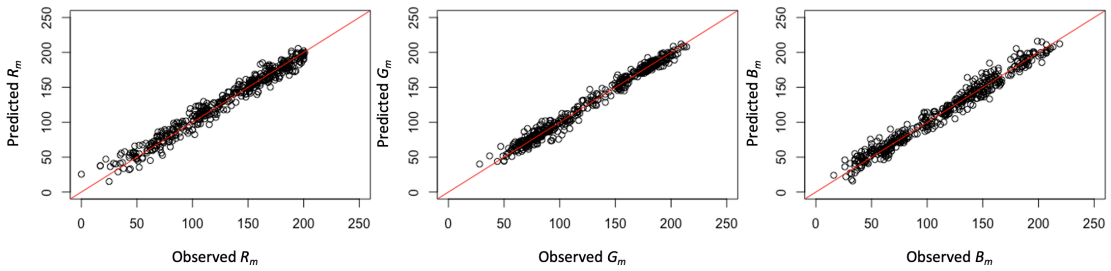

Figure 5.5 Measured RGB values observed vs. measured RGB values predicted by 5-fold cross validation, (a) observed R_m vs. predicted R_m, (b) observed G_m vs. predicted G_m, (c) observed B_m vs. predicted B_m

Table 5.5 presents the average MAE and R^2 of the MLP model from 5-fold cross validation for R_m, G_m, and B_m. 5-fold cross validation is also performed for a linear regression model and a cubic regression model, and their average MAE and R^2 values are also included in Table 5.5. The linear regression model includes the four main factors and their interactions as predictors. The cubic regression model contains quadratic terms and cubic terms of the four main factors, in addition to the terms included in the linear regression model. It can be observed that the MLP model outperforms the linear and cubic regression models for both performance measures, and the performance of the cubic regression model is better than the linear regression model. The prediction power of MLP has been demonstrated to be superior to linear regression in other applications when relationships between input variables and output responses are complex [21,25-27]. In practice, all the experimental data can be used for training, and the established model will be used for future predictions.

Table 5.5 Performance measures of three models.

Model	*MAE*			R^2		
	R	*G*	*B*	*R*	*G*	*B*
Linear regression	11.891	12.238	14.192	0.903	0.913	0.881
Cubic regression	10.440	8.825	11.143	0.926	0.948	0.928
MLP	6.082	6.008	6.093	0.973	0.974	0.976

5.5. Concluding Remarks

A multilayer perceptron (MLP) neural network model is established for predicting measured color of printed samples by PolyJet 3D printing given control factors (color specification and finish type). The developed MLP model is able to predict the measured color of printed samples with high accuracy. Also, the MLP model outperforms the linear regression model and the cubic regression model based on the two performance measures, MAE and R^2. This study applies MLP to the PolyJet 3D printing, but the methodology could be also implemented to other 3D full color printing processes (such as binder jetting, fused deposition modeling, or laminated object manufacturing) to predict measured color given control factors including color specification.

Data trends of the measured colors indicate that, when specified colors have larger or smaller RGB values (i.e., bright or dark in color), the difference between specified colors and measured colors of PolyJet printed samples could be large in the RGB color system. When specified colors span in the middle of the RGB color system, the difference between specified colors and measured colors could be small. It is also found that the relationships between control factors and measured color is nonlinear. In addition, matte finish type tends to produce higher measured B values than R and G values.

Although it has been shown that the MLP model performs adequately for predicting measured RGB values, this study has some limitations that will be addressed in future research. One limitation is that it lacks a color compensation scheme. The developed prediction model can predict output color well given color specification and process parameters. It would be more desirable to predict what values the control factors should be set in order to obtain a target output color. Ultimately, color compensation should be conducted before printing, with an optimization strategy to find the desired inputs to 3D printing, including color specification, in order to achieve a target output response, such as color, mechanical strength, dimension accuracy, and others. Another future direction is to use other advanced predictive models (such as Gaussian process regression) to achieve a good prediction accuracy with a small number of experimental samples.

5.6. References

[1] Wei, X., Zeng, L., and Pei, Z., 2017, "3D Printing of Medical Models: A Literature Review," Proceedings of the ASME International Mechanical and Engineering Congress and Exposition, vol. 14, V014T07A005.

[2] ASTM International, 2015, "Standard Terminology for Additive Manufacturing, General Principles Terminology," ASTM52900-15.

[3] Napadensky, E., 2009, "The Chemistry of Inkjet Inks," World Scientific, Singapore, pp. 249–261, Chap. 13.

[4] Goh, G., Sing, S., Lim, Y., Thong, J., Peh, Z., Mogali, S., and Yeong, W., 2021, "Machine Learning for 3D Printed Multi-Materials Tissue-Mimicking Anatomical Models," Materials & Design, vol. 211, 110125.

[5] Ng, W., Chan, A., Ong, Y., and Chua, C., 2020, "Deep Learning for Fabrication and Maturation Of 3D Bioprinted Tissues and Organs," Virtual and Physical Prototyping, vol. 15, no. 3, pp. 340–358.

[6] Goh, G., Sing, S., and Yeong, W., 2021, "A Review on Machine Learning in 3D Printing: Applications, Potential, and Challenges," Artificial Intelligence Review, vol. 54, no. 1, pp. 63–94.

[7] Sing, S., Kuo, C., Shih, C., Ho, C., and Chua, C., 2021, "Perspectives of Using Machine Learning in Laser Powder Bed Fusion for Metal Additive Manufacturing," Virtual and Physical Prototyping, vol. 16, no.3, pp. 372–386.

[8] Wei, X., Zeng, L., Pei, Z., 2019, "Experimental Investigation of PolyJet 3D Printing Process: Effects of Finish Type and Material Color on Color Appearance," Proceedings of the ASME International Mechanical and Engineering Congress and Exposition, vol. 2A, V02AT02A062.

[9] Zheng, L., Li, C., and Yang, S., 2020 "Analysis of Color Gamut in Color 3D Printing," Advanced Graphic Communication, Printing and Packaging Technology, Lecture Notes in Electrical Engineering, Springer, Singapore, vol. 600, pp. 148–155.

[10] Li, C., Zheng, L., and Xiao, Y., 2020, "Study on the Influencing Factors of Color Reproduction in Color 3D Printing," Advanced Graphic Communication, Printing

and Packaging Technology, Lecture Notes in Electrical Engineering, Springer, Singapore, vol. 600, pp. 156–163.

[11] Ronnenberg, M., and Farnand, S., 2019, “The Effect of Subsurface Structure on the Color Appearance of 3D Printed Objects,” Journal of Imaging Science and Technology, vol. 63, no. 4, pp. 120–127.

[12] Arikan, C., Brunton, A., Tanksale, T., and Urban, P., 2015, “Color-managed 3D-Printing with highly Translucent Printing Materials,” Proceedings of Society of Photo-Optical Instrumentation Engineers, The international Society for Optical Engineering, vol. 9398.

[13] Tanksale, T., and Urban, P., 2016, “Trichromatic Reflectance Capture Using A Tunable Light Source: Setup, Characterization and Reflectance Estimation,” Proceedings of Society for Imaging Science and Technology, International Symposium on Electronic Imaging. Measuring, Modeling, and Reproducing Material Appearance, pp. 355–361.

[14] Elek, O., Sumin, D., Zhang, R., Weyrich, T., Myszkowski, K., Bickel, B., Wilkie, A., and Křivánek, J., 2017, “Scattering-aware Texture Reproduction for 3D Printing,” Association for Computing Machinery Transactions on Graphics, vol. 36, no. 6, pp. 241–255.

[15] Brunton, A., Arikan, C., and Urban, P., 2015, “Pushing the Limits of 3D Color Printing: Error Diffusion with Translucent Materials,” Association for Computing Machinery Transactions on Graphics, vol. 35, no. 1, pp. 4–18.

[16] Brunton, A., Arikan, C., Tanksale, T., and Urban, P., 2018, "3D Printing Spatially Varying Color and Translucency," Association for Computing Machinery Transactions on Graphics, vol. 37, no. 4, pp. 157–169.

[17] Babaei, V., Vidimče, K., Foshey, M., Kaspar, A., Didyk, P., and Matusik. W., 2017, "Color Contoning for 3D printing," Association for Computing Machinery Transactions on Graphics, vol. 36, no. 4, pp. 124–138.

[18] Xiao, K., Sohiab, A., Sun, P., Yates, J., Li, C., and Wuerger, S., 2016, "A Colour Image Reproduction Framework for 3D Colour Printing," Proceedings of Advanced Laser Manufacturing Technology, vol. 10153, 1015318.

[19] Knowledge Base, 2019, "How do you Measure Color Accuracy?" Nix Color Sensor, Available: https://www.nixsensor.com/measure-color-accuracy/.

[20] mwuc14, 2014, "Understanding CIE Illuminants and Observers," WordPress.com, Available: https://measurewhatyousee.com/2014/10/10/understanding-cie-illuminants-and-observers/.

[21] Sobhani, J., Najimi, M., Pourkhorshidi, A., and Parhizkar, T., 2010, "Prediction of The Compressive Strength of No-Slump Concrete: A Comparative Study of Regression, Neural Network and ANFIS Models," Construction and Building Materials, vol. 24, no. 5, pp. 709–718.

[22] Goodfellow, I., Bengio, Y., and Courville, A., 2016, "Deep Learning," MIT Press, Boston, USA.

[23] Kingma, D., and Ba, J., 2015, "ADAM: A Method for Stochastic Optimization," Proceedings of International Conference on Learning Representations, arXiv:1412.6980.

[24] Akritas, M., 2016, "Probability & Statistics with R for Engineers and Scientists," Pearson Education, State College, USA.

[25] Özel, T., and Karpat, Y., 2005, "Predictive Modeling of Surface Roughness and Tool Wear in Hard Turning Using Regression and Neural Networks," International Journal of Machine Tools and Manufacture, vol. 45, no. 4–5, pp. 467–479.

[26] Madić, M., and Radovanović, M., 2012, "Comparative Modeling of CO_2 Laser Cutting Using Multiple Regression Analysis and Artificial Neural Network," International Journal of Physical Sciences, vol. 7, no. 16, pp. 2422–2430.

[27] Majumder, H., and Maity, K., 2018, "Predictive Analysis on Responses in WEDM of Titanium Grade 6 Using General Regression Neural Network (GRNN) and Multiple Regression Analysis (MRA)," Silicon, vol. 10, no. 4, pp. 1763–1776.

6. PREDICTION AND COMPENSATION OF COLOR DEVIATION BY RESPONSE SURFACE METHODOLOGY FOR POLYJET 3D PRINTING

Paper title:

Prediction and Compensation of Color Deviation by Response Surface Methodology for PolyJet 3D Printing

Published in:

Journal of Manufacturing and Materials Processing 5 (2021) 131

Authors' names:

Wei, X.[1], Bhardwaj, A.[1], Zeng, L.[2], Pei, Z.[1]

Authors' affiliations:

1. Department of Industrial and Systems Engineering, Texas A&M University, College Station, Texas 77843, USA
2. School of Data Science, City University of Hong Kong, Kowloon Tong, Hong Kong SAR, China

6.1. Introduction

3D printing provides a quick way to fabricate objects from computer-aided design (CAD) files. In the last decade, it has demonstrated its advantages over traditional manufacturing methods for complex and customizable parts [1]. Color 3D printing has become possible mainly due to the introduction of multi-material printing. Color of 3D printed objects had been limited to the color of material itself in the past, and now any color can be theoretically produced by mixing multiple materials. It is desirable to have the color of a 3D printed object as close to the target color as possible for several reasons. For example, when 3D printing is used to produce medical models [1], it is desirable that 3D printed anatomies have the color as close to real anatomies as possible. Such precise representations of colors could enhance effectiveness of medical models used in surgical planning and medical education. In addition, when 3D printing is used for product prototyping, the ability to precisely represent the color of 3D printed objects is needed to determine the final color of designed products used for mass production. Furthermore, when 3D printing is used for making final products, the color of printed products has psychological effects on users' perception, and an inaccurate color representation can significantly change the attractiveness and impression of the products.

However, every printer has its own achievable range of colors and tones [2]. As a consequence, the color of the printed object may vary from printer to printer when the same target color is used as the specified color in the printer software. PolyJet 3D printing can print multiple colors on a single object [3,4]. Although mechanical properties of parts printed from the PolyJet 3D printing process are not sufficiently high for load-bearing

applications, the process has its advantages in certain applications such as medical models or product prototyping [1]. The authors' preliminary experimental data, summarized in Table 6.1, show that the measured color of a printed sample often exhibits considerable deviations from the target color (when the target color is used as the specified color) in the PolyJet printer software. The colors in Table 6.1 are presented using the RGB color system. In the RGB color system, a color can be represented by three integer numbers R, G, and B, each ranging from 0 to 255. For example, the black color in the RGB color system is (0,0,0), and the white color is (255, 255, 255). Here, the measured color refers to the RGB values measured by a color measurement device, and the specified color is defined as the RGB values entered by the user in the printer software. Ideally, measured RGB values of printed samples should match the specified RGB values in the software. However, because the measured RGB values are often different from the specified RGB values, as shown in Table 6.1, the printed samples will not have the target color (if the target color is used as the specified color).

Table 6.1 Comparison of specified RGB values and measured RGB values

Specified (R,G,B)	(100,100,100)	(175,75,75)	(75,175,75)	(75,75,175)
				
Measured (R,G,B)	(109,108,102)	(166,84,80)	(94,170,73)	(84,82,146)
				

Some literature reviews on color 3D printing pointed out that surface color of 3D printed parts should be studied as much as other aspects of 3D printing such as material

formulation, microstructure optimization, and mechanical properties, to meet modern aesthetic and practical standards [5,6]. Color accuracy issues of six types of 3D printing processes are summarized by Yuan et al [6]. The significance of colors in 3D printing is also reflected in the large number of reported studies focusing on the colors of 3D printing [7-15]. Reported studies about the colorimetry of 3D printing mainly focus on the effects of surface texture and printing orientation on color appearance of 3D printed objects. For example, Wang et al. reported that post-processing of printed samples in a powder-based color 3D printing process led to higher saturation and smaller chromatic aberration, and soaking the printed samples increased surface brightness [7]. Sun and Lai compared the glossy and matte finish objects captured by an RGB camera and established a regression model to estimate their color differences [8]. Xiao and Brainard studied the effects of surface texture (i.e., glossy finish vs. matte finish) on color perception of observers. Their results showed that changing surface texture would not affect color appearance significantly [9]. Xiao et al. developed a color management system to minimize color variation among different printing orientations for powder-binder based multi-jet printing (MJP) [10]. Sun and Sie also developed a method to improve color uniformity among different orientations in MJP [11]. Ludwig et al. reported that color uniformity was affected by printing orientation and post-processing [12]. Morovic et al. controlled composition of individual voxels to co-optimize both color accuracy and mechanical properties [13]. Wittbrodt and Pearce studied effects of filament colors on mechanical properties in fused deposition modeling process, and found that PLA filaments with five colors (Black, Gray, Blue, White, and Natural) resulted in distinctive ultimate tensile

strength, yield strength, and maximum strain [14]. Eiriksson et al. studied relationships between color input and output spaces, and predicted color output by building a Look-Up Table [15]. There are no reported investigations on deviations between the measured colors of 3D printed objects and target colors (when the target colors are used as the specified colors in the printer software). There are no commonly accepted methods to compensate such deviations, either.

This paper will fill this gap in the literature by presenting, for the first time, a systematic approach (versus the trial-and-error approach) to find the optimal color specifications for the printer software to result in a color on the printed sample that has the smallest deviation from the target color. It reports a study on the color deviation problem in PolyJet printing using the response surface methodology (RSM). As a method for process optimization, RSM has been widely used [16]. In general, RSM can be broken down into three steps: (1) collecting experimental data of response(s) obtained by adjusting process parameters in the close proximity to the maximum/minimum of the response(s), (2) developing a predictive model for the response(s) given the process parameters, and (3) optimizing the process parameters that predict the maximum/minimum of the response(s). This study follows these three steps. First, a set of designed experiments according to central composite design are conducted for a target color to collect measured RGB values of printed samples given specified RGB values in printer software. The set of experiments have 15 different specified RGB values (the target RGB value plus 14 RGB values that are in the close proximity to the target RGB value). Secondly, using the experimental data, a statistical predictive model is developed for

predicting deviations between measured RGB values and the target RGB values when different specified RGB values are used in the printer software. Finally, the predictive model and the desirability function are used to find the optimal color specification (i.e., specified RGB values) such that the deviations between the predicted RGB values of a printed sample and the target RGB values are minimized. Four cases with four different target colors are used to demonstrate the effectiveness of the proposed method.

The rest of the paper is organized as follows. Section 6.2 presents the experimental setup and procedure. Section 6.3 describes the methodology to establish the second-order multivariate multiple regression model. Section 6.4 reports the determination of the optimal color specification using the predictive model and the desirability function. Section 6.5 examines the effectiveness of the proposed method in four cases (four different target colors). The results obtained by the proposed method are compared with the performance of the conventional color specification method. Finally, Section 6.6 summarizes conclusions, and discusses limitations of the proposed method, and directions of future research.

6.2. Experimental Setup and Procedure

6.2.1. Process parameters related to color and their settings

Important process parameters related to color in PolyJet printing include finish type, material combinations, and color profiles. There are two options for finish type: glossy finish and matte finish. When glossy finish is selected, support materials only cover the bottom surface of the object and the surface of overhanging structure. When matte

finish is selected, support materials cover the entire surface of the object. Glossy finish type is used in this study because color measurements to avoid potential problems caused differences in removal of support material on the surfaces [17].

For material combinations, five base materials are mixed to generate a desired color: VeroPureWhite (RGD837), VeroBlackPlus (RGD875), VeroCyan (RGD843), VeroYellow (RGD836), and VeroMagenta (RGD851). SUP706B is used as the support material.

A profile in terms of printing color is a criterion to convert the RGB values used in digital monitors to CMYK (abbreviation for cyan, magenta, yellow, and black) values used in physical printers. Because the CMYK system does not cover the full spectrum of colors of the RGB system, a profile dictates how the software approximates RGB values to CMYK values [18]. “Natural texture” and “Natural shells” are chosen as the texture profile and color profile, respectively. There are two types of profiles because of two different options to print colors: the texture mapping based option and the shell based option. The texture mapping based option that imposes color images on the surfaces of an object (its interior is white) follows the texture profile, while the shell based option which allows users to assign colors to an entire object follows the color profile. The shell based option is used to set specified RGB values in this study.

6.2.2. Experimental design using central composite design

The central composite design (CCD) is frequently used to design experiments for a second-order model, and can provide enough samples without using a full factorial design [16]. In this study, each target color requires a CCD to collect measured RGB

values and specified RGB values in the proximity to the target RGB values. Figure 6.1 illustrates the points of RGB values in this experimental design. The RGB system is represented by the three axes. The coordinates of each design point are its coded RGB values. The center point represents the target color. Each experiment contains only one sample for each design point because previous experiments showed that the differences in measured RGB values for replicated samples are negligible [19]. Thus, a total of 15 samples are printed for a target color.

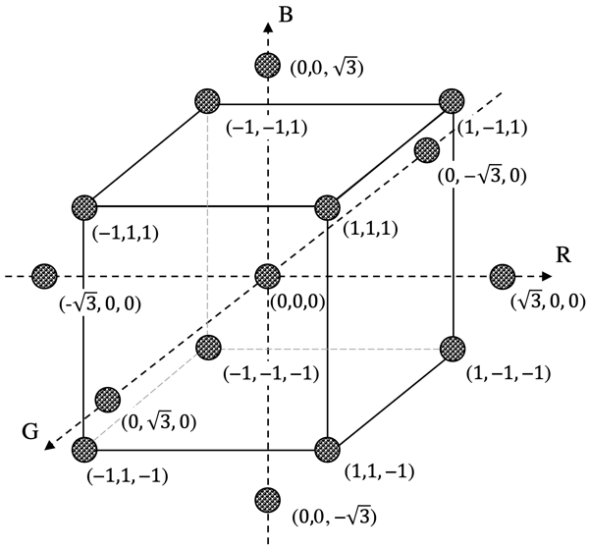

Figure 6.1 Illustration of a central composite design for coded RGB values

6.2.3. Preparation of printed samples

Printed samples are 20 mm x 20 mm square plates with the thickness of 2 mm. The dimensions are selected because the minimum scanning area required for the color measurement device is 15 mm^2. The sample geometry is generated in Autodesk Fusion 360. Layer thickness of 27 μm is selected to save printing time. The samples are printed 15 months after the printer installation, and maintenances such as cleaning had been

carried out according to the manufacturer's manual. Right before each printing, cleaning wizard, a standard procedure of the printer to reduce color contaminations on print heads, is performed. After the completion of printing, gel-like support materials (SUP706B) are manually removed by using a scraper. Then, pressurized water is blasted to the samples for further removal of support materials.

6.2.4. Measurement of color

The color of every printed sample is measured by a colorimeter, Nix Pro color sensor (Ontario, Canada). Illuminant and observer are two parameters that need to be set for the colorimeter [20]. The illuminant used is D50 which emulates horizon daylight with a color temperature of 5000 Kelvin [21]. The observer (the receiver of the illuminant) is set to 2° field of view, corresponding to the angle of cones in the fovea of human eyes. Three measurements are taken on each sample and the average of the three measurements yields the measured RGB values for the sample.

6.3. Second-Order Multivariate Multiple Regression

Using the experimental data obtained according to CCD, a second-order multivariate multiple regression (MMR) model can be built to predict the deviations between measured RGB values and target RGB values when different specified RGB values are used in the printer software. The second-order MMR model is suitable because there are multiple response and predictor variables. Definitions of variables and coefficients involved in the MMR are summarized in Table 6.2. Assume there are n observations in the training data. Each observation contains 6 elements

$\{x_{i1}, x_{i2}, x_{i3}, y_{i1}, y_{i2}, y_{i3}: i = 1,2 \dots, n\}$, where the former three are the specified RGB values and the latter three are the measured RGB values. In the MMR model, deviations of measured RGB values from the target RGB values are treated as responses and the specified RGB values are treated as predictors. The predictive model for the k-th, $k = 1, 2, 3$, response is as follows

$$y_{ik} - t_k = \beta_{0k} + \sum_{j=1}^{3} \beta_{jk} x_{ij} + \sum_{l,q} \beta_{lqk} x_{il} x_{iq} + \sum_{j=1}^{3} \beta_{jjk} x_{ij}^2 + \varepsilon_{ik} \quad (1)$$

where β_{0k} is the intercept, β_{jk} is the coefficient of the first-order term, β_{lqk} is the coefficient of the interaction term, β_{jjk} is the coefficient of the second-order term, and ε_{ik} is the random noise. The coefficients of the model can be estimated by the least-squares method [16] using experimental data (i.e., training data).

Once the MMR model is established, it can be used to predict the deviations between measured RGB values of printed sample and target RGB values (when different specified RGB values are used in printer software). Let the k-th specified RGB values be $\{x_1, x_2, x_3\}$, and the corresponding measured RGB values be $\{y_1, y_2, y_3\}$. The prediction of the deviation of the k-th response is

$$\hat{y}_k - t_k = \hat{\beta}_{0k} + \sum_{j=1}^{3} \hat{\beta}_{jk} x_j + \sum_{l,q} \hat{\beta}_{lqk} x_l x_q + \sum_{j=1}^{3} \hat{\beta}_{jjk} x_j^2 \quad (2)$$

where the "^" sign of the coefficients indicates their estimates based on the training data.

Table 6.2 Definitions of variables and coefficients

Variable/Coefficient	Definition
i	Index of observation in training data, $i \in \{1, \dots, 15\}$
j	Index of predictor, $j \in \{1,2,3\}$
l	Index of predictor, $l \in \{1,1,2\}$
q	Index of predictor, $q \in \{2,3,3\}$
k	Index of response, $k \in \{1,2,3\}$
x_{ij}	j-th predictor of i-th observation
x_{il}	l-th predictor of i-th observation
x_{iq}	q-th predictor of i-th observation
x_j	j-th given predictor
x_j^*	j-th optimal specified predictor
y_{ik}	k-th response of i-th observation
y_k	k-th measured response for the given predictor
t_k	k-th target response
β_{0k}	Regression intercept for k-th response
β_{jk}	First-order regression coefficient of j-th predictor for k-th response
β_{lqk}	Two-way interaction coefficient between l -th predictor and q -th predictor for k-th response
β_{jjk}	Second-order regression coefficient of j-th predictor for k-th response
A	Maximum acceptable difference between predicted response and target response
d_k	Individual desirability of k-th response
D	Overall desirability

6.4. Determination of The Optimal Color Specification

The optimal color specification (i.e., the specified RGB values to be used in the printer software aiming to achieve the measured RGB values of printed sample as close to the target RGB values as possible) can be determined by minimizing the difference between the predicted RGB values of printed sample and the target RGB values. Since it is necessary to optimize the specified RGB values simultaneously, this is a multi-response optimization problem. Desirability function is a popular methodology for multi-response optimization [22]. The optimal color specification is defined to be the specified RGB values $\{x_1^*, x_2^*, x_3^*\}$ whose corresponding predicted RGB values $\{\hat{y}_1^*, \hat{y}_2^*, \hat{y}_3^*\}$ from Eq. (2)

are closest to the given target RGB values $\{t_1, t_2, t_3\}$. In other words, the difference between $\{\hat{y}_1^*, \hat{y}_2^*, \hat{y}_3^*\}$ and $\{t_1, t_2, t_3\}$ is minimized. Since there are three responses, three individual desirability functions are firstly defined to measure the difference for each response. Specifically, the individual desirability function for the k-th, $k = 1,2,3$, response is defined as

$$d_k = \begin{cases} 1 - \frac{|\widehat{y_k} - t_k|}{A} & if\ A \geq |\widehat{y_k} - t_k| \\ 0 & otherwise \end{cases} \quad (3)$$

where A is the acceptance range set by the user. Intuitively, the desirability d_k indicates the difference between the predicted RGB values and its corresponding target RGB values. If this difference is larger than the acceptance range, the desirability is 0, meaning that it is not acceptable. When the difference is within the acceptance range, the desirability is a linear function of the difference and increases as the difference decreases. The highest desirability, i.e., $d_k = 1$, is achieved when the difference is 0, that is, the predicted RGB values exactly match the target RGB values. The overall desirability function as the objective function in the optimization step is a multiplication of the three individual desirability functions.

$$D = \prod_{k=1}^{3} d_k \quad (4)$$

The optimal color specification is obtained by maximizing the overall desirability.

$$\{x_1^*, x_2^*, x_3^*\} = \underset{\{x_1, x_2, x_3\}}{\arg\max}\, D \quad (5)$$

6.5. Determination of the Effectiveness of the Proposed Method by Four Cases

Demonstration of the effectiveness of the proposed method consists of four steps: 1) conducting a set of designed experiments according to the central composite design (CCD) with the target color as its center point, 2) developing a second-order multivariate multiple regression model using the experimental data (training data), 3) finding the optimal color specification using the developed model and the desirability function, and 4) printing the sample using the optimal color specification as the specified color in the printer software. The proposed method needs to be applied to every target color because the model's predictions are expected to be only effective in the approximation of the target color. Four target colors are selected to demonstrate the effectiveness of the proposed method. The four target colors are: (1) a color with equal RGB values, (2) a color with a larger red value (meaning that the R value is much higher than the G and B values), (3) a color with a larger green value, and (4) a color with a larger blue value.

6.5.1. Conducting a set of designed experiments and collecting experimental data

For each target color, 15 samples are printed according to CCD and are shown in Figure 6.2. Table 6.3, Table 6.4, Table 6.5, and Table 6.6 show the CCD matrices and measurement results for Case 1, Case 2, Case 3, and Case 4, respectively. It can be observed that there are considerable deviations between the measured RGB values and the target RGB values.

Table 6.3 CCD matrix and results for Case 1

Sample	Specified RGB values			Coded RGB values			Measured RGB values		
	sR	sG	sB	cR	cG	cB	mR	mG	mB
1	90	90	90	-1	-1	-1	99	97	92
2	90	110	90	-1	1	-1	100	115	92
3	110	90	90	1	-1	-1	117	97	93
4	110	110	90	1	1	-1	118	116	93
5	90	90	110	-1	-1	1	102	99	113
6	90	110	110	-1	1	1	104	119	112
7	110	90	110	1	-1	1	119	98	113
8	110	110	110	1	1	1	119	118	112
9	100	100	100	0	0	0	110	107	101
10	117	100	100	1.73	0	0	125	106	103
11	83	100	100	-1.73	0	0	105	108	102
12	100	117	100	0	1.73	0	110	123	103
13	100	83	100	0	-1.73	0	110	91	103
14	100	100	117	0	0	1.73	111	107	119
15	100	100	83	0	0	-1.73	109	105	83

Table 6.4 CCD matrix and results for Case 2

Sample	Specified RGB values			Coded RGB values			Measured RGB values		
	sR	sG	sB	cR	cG	cB	mR	mG	mB
1	145	65	65	-1	-1	-1	153	78	75
2	145	85	65	-1	1	-1	150	94	71
3	205	65	65	1	-1	-1	163	79	63
4	205	85	65	1	1	-1	168	89	60
5	145	65	85	-1	-1	1	155	79	95
6	145	85	85	-1	1	1	152	96	91
7	205	65	85	1	-1	1	166	79	81
8	205	85	85	1	1	1	171	89	79
9	175	75	75	0	0	0	164	84	79
10	227	75	75	1.73	0	0	164	80	62
11	123	75	75	-1.73	0	0	127	82	78
12	175	92	75	0	1.73	0	168	99	78
13	175	58	75	0	-1.73	0	159	74	81
14	175	75	92	0	0	1.73	165	84	96
15	175	75	58	0	0	-1.73	162	85	65

Table 6.5 CCD matrix and results for Case 3

Sample	Specified RGB values			Coded RGB values			Measured RGB values		
	sR	sG	sB	cR	cG	cB	mR	mG	mB
1	65	155	65	-1	-1	-1	88	160	67
2	85	155	65	1	-1	-1	101	162	67
3	65	195	65	-1	1	-1	108	167	56
4	85	195	65	1	1	-1	117	172	57
5	65	155	85	-1	-1	1	82	162	85
6	85	155	85	1	-1	1	98	164	86
7	65	195	85	-1	1	1	102	169	70
8	85	195	85	1	1	1	111	173	73
9	75	175	75	0	0	0	99	168	71
10	75	210	75	0	1.73	0	115	173	59
11	75	140	75	0	-1.73	0	87	148	77
12	92	175	75	1.73	0	0	111	172	73
13	58	175	75	-1.73	0	0	90	166	71
14	75	175	92	0	0	1.73	95	170	87
15	75	175	58	0	0	-1.73	104	167	59

Table 6.6 CCD matrix and results for Case 4

Sample	Specified RGB values			Coded RGB values			Measured RGB values		
	sR	sG	sB	cR	cG	cB	mR	mG	mB
1	65	65	125	-1	-1	-1	81	78	128
2	85	65	125	1	-1	-1	99	79	128
3	65	65	225	-1	-1	1	85	82	141
4	85	65	225	1	-1	1	94	83	141
5	65	85	125	-1	1	-1	82	96	127
6	85	85	125	1	1	-1	98	95	127
7	65	85	225	-1	1	1	73	85	145
8	85	85	225	1	1	1	84	86	144
9	75	75	175	0	0	0	84	82	142
10	75	75	255	0	0	1.6	84	83	143
11	75	75	95	0	0	-1.6	87	84	98
12	91	75	175	1.6	0	0	97	83	141
13	59	75	175	-1.6	0	0	73	83	143
14	75	91	175	0	1.6	0	84	93	152
15	75	59	175	0	-1.6	0	88	78	137

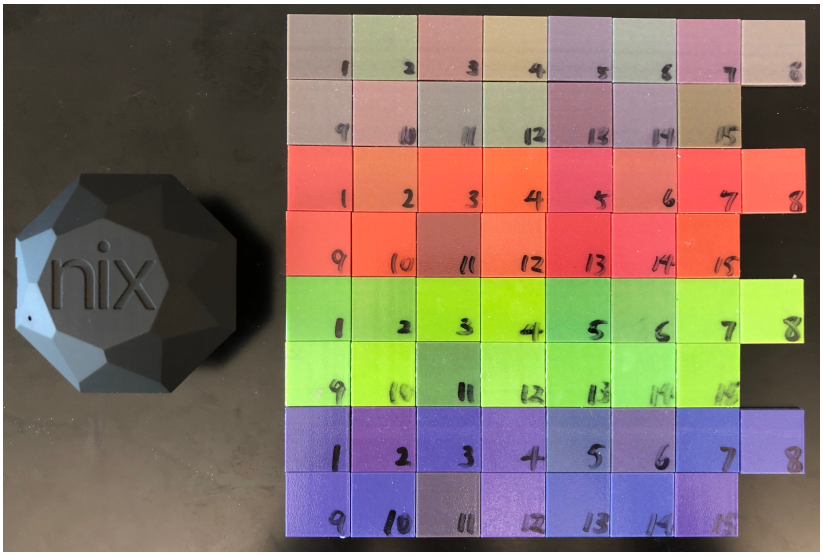

Figure 6.2 The Nix Pro colorimeter and printed samples for four cases

Table 6.7 Coefficient estimates of the fitted MMR models

Case	$\hat{y}_k$	$\widehat{\beta_{0\cdot}}$	$\widehat{\beta_{1\cdot}}$	$\widehat{\beta_{2\cdot}}$	$\widehat{\beta_{3\cdot}}$	$\widehat{\beta_{12\cdot}}$	$\widehat{\beta_{13\cdot}}$	$\widehat{\beta_{23\cdot}}$	$\widehat{\beta_{11\cdot}}$	$\widehat{\beta_{22\cdot}}$	$\widehat{\beta_{33\cdot}}$
1	mR	-100.360	-1.158	1.091	1.409	-0.003	-0.005	0.000	0.013	-0.004	-0.004
2		-144.596	1.956	-1.460	-0.470	0.007	0.001	0.000	-0.006	0.003	0.003
3		91.109	1.098	0.626	-0.753	-0.010	0.006	0.000	0.005	0.001	0.001
4		-36.047	0.362	-0.704	0.500	0.000	-0.004	-0.006	0.006	0.010	0.000
1	mG	-71.940	-0.078	0.158	0.486	0.001	-0.004	0.004	0.001	0.001	-0.002
2		-54.287	0.755	-0.161	-0.536	-0.005	-0.001	0.001	-0.001	0.011	0.004
3		-152.095	-0.708	1.892	-0.800	0.005	-0.003	0.003	0.001	-0.006	0.004
4		4.533	-0.819	-0.343	0.336	-0.003	0.001	-0.007	0.006	0.015	0.000
1	mB	33.926	-0.744	-1.132	1.542	0.000	-0.003	-0.003	0.005	0.007	0.000
2		-85.195	0.995	-0.656	0.335	0.001	-0.001	0.001	-0.003	0.001	0.005
3		-153.829	0.176	0.923	1.433	0.001	0.004	-0.003	-0.004	-0.003	-0.002
4		-100.584	-0.095	-1.577	1.205	-0.001	0.000	0.002	0.001	0.010	-0.003

6.5.2. Developing multivariate multiple regression (MMR) model

For each of the four target colors, the second-order MMR model as described in Eqs. (1) - (2) is developed using the experimental data. Table 6.7 shows the coefficient estimates of the model for each of the four cases. These models can be used to predict the

deviation of measured RGB values from the target RGB values. Two observations can be made. First, the non-zero coefficient estimates of the three first-order terms in all the responses of the four cases indicate that each of the measured RGB values depends on all three specified RGB values, instead of merely depending on one of the specified RGB values. Second, the coefficient estimates of the interaction and second-order terms are not negligible, which indicates the presences of interaction and second-order effects.

To provide a visual presentation of the MMR models, Figure 6.4 displays the deviation response surface plots of Case 3 predicted by the MMR model. Only two of the specified RGB values can be shown in each plot. First, it can be observed that the effects of the specified G value on the deviations are substantial. The deviations of the measured R values positively increase as the specified G value increases, and the deviations of the measured B value negatively increases as the specified G value increases. In fact, none of the response surfaces are completely flat, which indicate all the specified RGB values have effects on the deviation. Second, there are also noticeable interaction and second-order effects of the specified RGB values on the deviation. For example, the response surface of the deviation of measured R value based on the specified G and B values shows a convex curvature, and the response surface of the deviation of measured G value based on the specified R and G values shows a concave curvature, meaning that second-order effects exist. Moreover, the response surface of the deviation of measured R value based on the specified R and G values shows a twisted plane, indicating that interaction effects are present.

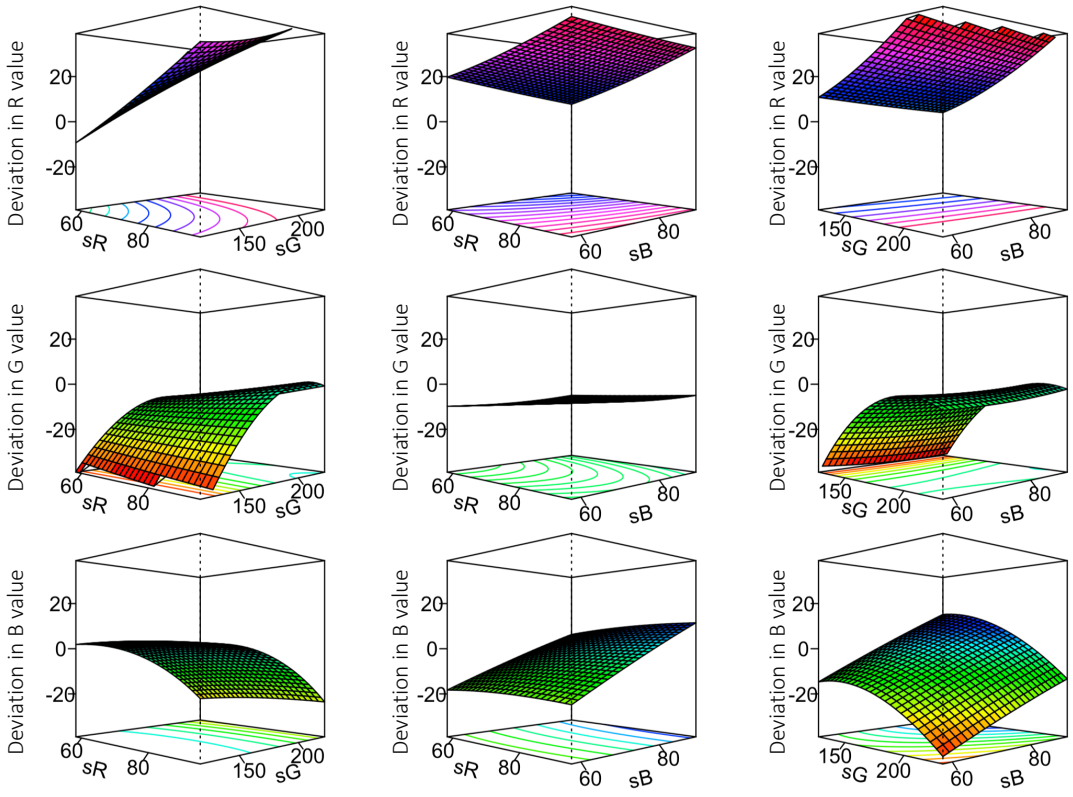

Figure 6.3 Plots of response surfaces for Case 3 based on the coefficient estimates

6.5.3. Finding the optimal color specification using the developed model and the desirability function

Based on the developed MMR models, the optimal color specification for each target color is determined by the desirability function as represented by Eqs. (3) - (5). Table 6.8 shows the optimal color specifications (that should be used as specified RGB values to print samples) and the associated desirability values. The overall desirability values for Case 1 and Case 3 are close to its maximum, 1, meaning that the predicted RGB values are close to the target values. The overall desirability values for Case 2 and Case 4 are relatively low, suggesting that the predicted RGB values are not close to the target values.

Table 6.8 Optimal color specifications determined by individual and overall desirability values

Case	RGB	Desirability		Target	Predicted	Optimal color specification
		Individual	Overall			
1	R	0.99	0.95	100	100	83
	G	0.92		100	100	92
	B	0.93		100	100	97
2	R	0.33	0.60	175	165	197
	G	0.66		75	78	68
	B	0.98		75	75	76
3	R	0.96	0.96	75	75	16
	G	0.96		175	175	178
	B	0.96		75	75	95
4	R	0.90	0.34	75	76	59
	G	0.31		75	82	72
	B	0.14		175	145	198

6.5.4. Printing samples using the optimal color specifications

To show the advantage of the proposed method over the conventional method of color specification (i.e., using the target color as the specified color), two samples are printed for each target color. One sample is printed using the optimal color specification, determined by the proposed method, shown in Table 6.8 as the specified RGB values in the printer software, and another sample is printed using the target color as the specified RGB values in the printer software. Both samples are measured by the colorimeter.

Table 6.9 compares the measured RGB values obtained by the proposed method and the measured RGB values obtained by the conventional method for the four cases. Such comparison is also shown in Figure 6.4. The proposed method produces smaller deviations (in term of the sum of deviations) than the conventional method in all the four cases. The best results are in Case 1 where the sum of deviations from the proposed method

is less than 40% of that from the conventional method. This comparison demonstrates that the proposed method can achieve the target color better than the conventional method.

Table 6.9 Comparison of deviations of measured RGB values on printed samples from the target RGB values using the proposed method versus the conventional specification method without compensation

Case	RGB	Target	Proposed method				Conventional specification method without compensation			
			Specified	Measured	Deviation	Sum of Dev.	Specified	Measured	Deviation	Sum of Dev.
1	R	100	83	95	5	7	100	109	9	19
	G	100	92	101	1		100	108	8	
	B	100	97	101	1		100	102	2	
2	R	175	197	166	9	14	175	166	9	23
	G	75	68	79	4		75	84	9	
	B	75	76	74	1		75	80	5	
3	R	75	16	77	2	22	75	94	19	26
	G	175	178	164	11		175	170	5	
	B	75	95	84	9		75	73	2	
4	R	75	59	76	1	42	75	84	9	45
	G	75	72	83	8		75	82	7	
	B	175	198	142	33		175	146	29	

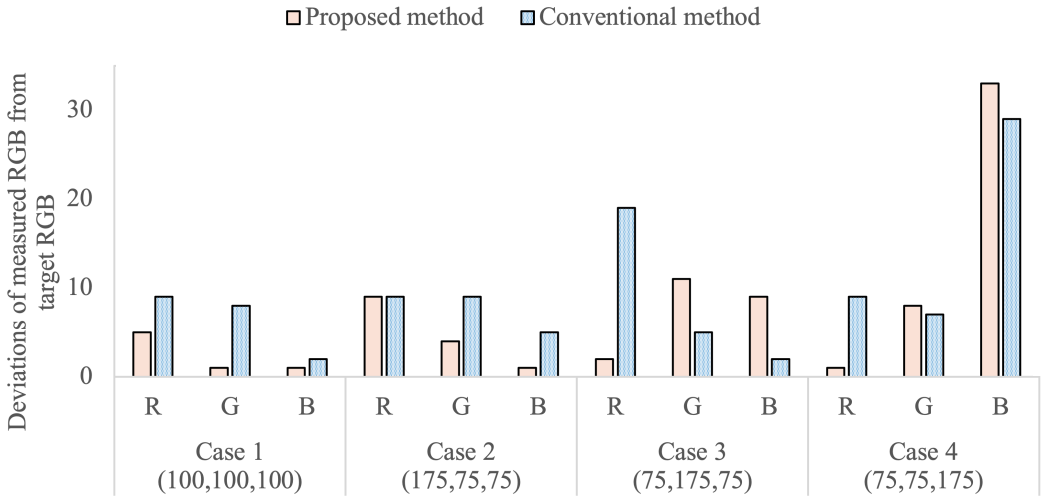

Figure 6.4 Deviations of measured RGB values from target RGB values when using the proposed method versus the conventional specification method without compensation

6.6. Conclusion

A method (based on the response surface methodology) has been proposed to compensate the color deviation of a printed sample from the target color for the printed sample in PolyJet 3D printing. The key of the study is to use the optical color specification (not the target color) determined by the proposed method as the specified color in the printer software. The proposed method consists of three steps: (1) collecting experimental data of printed samples according to the central composite design with its center being the target color, (2) developing a second-order multivariate multiple regression model using the experimental data to predict the deviation of measured color from the target color, and (3) finding the optimal color specification (that minimizes the color deviation when used as the specified color in the printer software) using the developed model and the desirability function.

This method has been applied to four cases (each has a different target color) to demonstrate its effectiveness. Experimental results show that the proposed method performs better than the conventional specification method without compensation (directly using the target color as the specified color in printer software) in all four cases (four target colors). The average improvement over the conventional specification method without compensation is 33%. It is noted that the proposed compensation method is not intended to cover the entire color gamut. In order for the compensation method to work, experiments have to be conducted in the proximity to the target color. This paper presents a systematic approach (versus the trial-and-error approach) to find the optimal color specifications for the printer software to result in a color on the printed sample that has the

smallest deviation from the target color. Although this study focused on the PolyJet printing process, the proposed method can be applied to any 3D printing processes to improve its color quality.

Future investigations are needed to understand why there are performance differences of the proposed method among the four cases. One approach towards consistent performance is to use advanced statistical predictive methods such as neural network and Gaussian process to improve the model predictive capacity. Furthermore, understanding whether and how the printing parameters such as finish type and layer thickness affect the color deviation of printed samples could improve explanatory power of the predictive methods.

6.7. References

[1] Wei, X., Zeng, L., and Pei, Z., 2017, "3D Printing of Medical Models: A Literature Review," Proceedings of the ASME International Mechanical and Engineering Congress and Exposition, V014T07A005.

[2] Goldstein, R., Chu, S., Lee, E., and Stappert, C., 2018, "Understanding Color," Ronald E. Goldstein's Esthetics in Dentistry, pp. 270–294.

[3] Napadensky, E., 2009, "Inkjet 3D Printing," The Chemistry of Inkjet Ink, pp. 249–261.

[4] Stratasys, 2018, "J750 Digital Anatomy 3D Printer," Available: https://www.stratasys.com/3d-printers/j750-digital-anatomy.

[5] Yuan, J.; Chen, G.; Li, H.; Prautzsch, H.; Xiao, K. Accurate and Computational: A Review of Color Reproduction in Full-color 3D Printing. Materials & Design 2021, vol. 209, 109943.

[6] Yuan, J.; Zhu, M.; Xu, B.; Chen, G. Review on Processes and Color Quality Evaluation of Color 3D Printing. Rapid Prototyping Journal 2018, Vol. 24, no. 2, pp. 409–415.

[7] Wang, X., Chen, C., Yuan, J., and Chen, G., 2019, "Color Reproduction Accuracy Promotion of 3D-Printed Surfaces Based on Microscopic Image Analysis," International Journal of Pattern Recognition Artificial Intelligence, vol. 34, no. 01, 2054004.

[8] Sun, P., and Lai, Y., 2017, "Estimating Appearance Differences of 3D Objects with an RGB Camera," Electronic Imaging, Color Imaging XXII: Displaying, Processing, Hardcopy, and Applications, vol. 2017, no. 18, pp. 36–41.

[9] Xiao, B., and Brainard, D., 2008, "Surface Gloss and Color Perception of 3D Objects," Visual Neuroscience, vol. 25, no. 3, pp. 371–385.

[10] Xiao, K., Sohiab, A., Sun, P., Yates, J., Li, C., and Wuerger, S., 2016, "A Colour Image Reproduction Framework for 3D Colour Printing," Proceedings of the Society of Photographic Instrumentation Engineers, vol. 10153, Advanced Laser Manufacturing Technology, 1015318.

[11] Sun, P. and Sie, Y., 2016, "Color Uniformity Improvement for an Inkjet Color 3D Printing System," Electronic Imaging, Color Imaging XXI: Displaying, Processing, Hardcopy, and Applications, vol. 2016, no. 20, pp. 1–6.

[12] Ludwig, M., Moroney, N., Tastl, I., Gottwals, M., and Meyer, G., 2018, "Perceptual Appearance Uniformity in 3D Printing," Electronic Imaging, Material Appearance, vol. 2018, no. 8, pp. 209-1–12.

[13] Morovič, P., Morovič, J., Tastl, I., Gottwals, M., and Dispoto, G., 2019, "Co-Optimization of Color and Mechanical Properties by Volumetric Voxel Control," Structural and Multidisciplinary Optimization, vol. 60, no. 3, pp. 895–908.

[14] Wittbrodt, B.; Pearce, J. The Effects of PLA Color on Material Properties of 3-D Printed Components. Additive Manufacturing 2015, vol 8, pp. 110–116.

[15] Eiriksson, E., Pedersen, D., and Aanaes, H., 2015, "Predicting Color Output of Additive Manufactured Parts," Proceedings of Achieving Precision Tolerances in Additive Manufacturing: ASPE Spring Topical Meeting, The American Society for Precision Engineering, vol. 60, pp. 95–99.

[16] Myers, R., Montgomery, D., Anderson-Cook, C., 2009, "Experimental Designs for Fitting Response Surfaces—I," Response Surface Methodology: Process and Product Optimization Using Designed Experiments, pp. 296–335.

[17] Ronnenberg, M., and Farnand, S., 2019, "The Effect of Surface Texture on Color Appearance of 3D Printed Objects," Proceedings of Color Imaging Conference, vol. 2018, no. 1, pp. 128–133.

[18] Adjusting print settings, 2019, "Print settings for PolyJet printers," GrabCAD, Available: https://help.grabcad.com/article/226-adjusting-print-settings#pj.

[19] Wei, X., Zeng, L., Pei, Z., 2019, "Experimental Investigation of PolyJet 3D Printing Process: Effects of Finish Type and Material Color on Color Appearance,"

Proceedings of the ASME International Mechanical and Engineering Congress and Exposition, vol. 2A, V02AT02A062.

[20] Knowledge Base, 2019, “How do you Measure Color Accuracy?,” Nix color sensor, Available: https://www.nixsensor.com/measure-color-accuracy/.

[21] Measure What You See, 2014, “Understanding CIE Illuminants and Observers”, WordPress.com, Available: https://measurewhatyousee.com/2014/10/10/understanding-cie-illuminants-and-observers/.

[22] Anderson, M., and Whitcomb, P., 2017, “Finding Your Sweet Spot for Multiple Responses,” RSM Simplified: Optimizing Processes Using Response Surface Methods for Design of Experiments, pp. 110–128.

7. EXPERIMENTAL INVESTIGATION ON ULTRASONIC HOPPER DISPENSING SYSTEM IN POWDER BED ADDITIVE MANUFACTURING

Paper title:

Experimental Investigation on Ultrasonic Hopper Dispensing System in Powder Bed Additive Manufacturing

Published in:

Journal of Manufacturing Processes 71 (2021) 106-112

Authors' names:

Wei, X.[1], Moghadasi, M.[2], Du, W.[1], Ma, C.[3], Pei, Z.[1]

Authors' affiliations:

1. Department of Industrial and Systems Engineering, Texas A&M University, College Station, Texas 77843, USA
2. Department of Materials Science and Engineering, Texas A&M University, College Station, Texas 77843, USA
3. Department of Engineering Technology and Industrial Distribution, Texas A&M University, College Station, Texas 77843, USA

7.1. Introduction

Powder bed additive manufacturing includes powder bed fusion and binder jetting processes [1]. In powder bed fusion process, powder is fused via high energy laser or electron beam. Material selections for powder bed fusion process range from metals to polymers. Binder jetting process selectively deposits binder onto powder bed to temporarily adhere particles together to form green parts. The green parts then go through post-processing (including curing, debinding, and sintering) to become final parts. Its material selections include ceramic materials (e.g., alumina and zirconia) as well as metals and polymers [2].

Powder bed formation is an important step in both powder bed fusion and binder jetting processes. In the traditional piston-based method [3], a spreader (e.g., roller or blade) pushes feedstock powder from a feed region to a powder bed. Note that, in order to cover the entire powder bed, some of the powder is pushed across a long distance. This method is not effective for fine powders (those with small particle sizes, e.g., < 10 μm) due to unacceptable flowability [4]. In the hopper-based method, powder bed formation is divided into two steps: powder dispensing and spreading. In powder dispensing step, feedstock powder is dispensed from the hopper to cover the entire powder bed. In powder spreading step, a spreader pushes the powder to uniformly level the powder bed. Note that the travel distance of the powder is much shorter, compared to the traditional piston-based method. The hopper dispensing system assisted by ultrasonic vibration became available recently on some powder bed additive manufacturing printers (e.g., ExOne Innovent Plus

binder jetting printers). The ultrasonic hopper dispensing system can dispense powder directly onto the powder bed, and is suitable for both fine and coarse powders.

Table 7.1 summarizes reported studies involving effects of powder dispensing variables on powder bed density as well as properties of printed parts, including green density, sintered density, and mechanical strength. In these studies, neither powder dispense rate (also known as flow rate) nor dispensed powder amount was measured directly. However, their results implied that, regardless of which method (hopper-based and piston-based) was used, higher dispense rate (or larger dispensed powder amount) would improve powder bed density, green density, sintered density, and strength of sintered parts.

Table 7.1 Reported studies related to effects of powder dispensing variables

Method	*Material*	*Particle size (μm)*	*Printer*	*Major result*	*Reference*
Hopper-based	Alumina	40	ExOne Innovent	Faster oscillator speed and slower recoat speed (likely causing higher dispense rate) led to higher density of printed green parts.	[5]
Hopper-based	Copper	5	ExOne Innovent Plus	Higher ultrasonic intensity (likely causing higher dispense rate) led to slightly higher density of printed green parts.	[6]
Piston-based	SS316L	38	ExOne M-Flex	Higher ratios between dispensed powder thickness and print layer thickness (equavelant to larger dispense amount) led to higher density of printed green parts.	[7]
Piston-based	SS316L	N/A*	ExOne X-1 Lab	Higher ratios between dispensed powder thickness and print layer thickness (equavelant to larger dispense amount) led to higher strength of sintered parts.	[8]
Piston-based	Polyamide	58	3D Systems SLS	Higher ratios between dispensed powder thickness and print layer thickness (equavelant to larger dispense amount) led to higher powder bed density.	[9]

* Information not available in reference paper [8].

Therefore, it is important to have higher dispense rate to dispense sufficient amount of powder onto the powder bed. However, dispensing unnecessarily larger amount of powder can also result in longer printing time and higher manufacturing cost. The authors observed that the ultrasonic hopper dispensing system on the binder jetting printer (Innovent Plus, ExOne, PA, USA) installed in their lab, when dispensing variables are set to the fixed values, does not always dispense powder at a constant rate. To overcome this drawback, a common practice is to set the dispense rate sufficiently (but maybe unnecessarily) high. Therefore, it is desirable to understand the dispensing behavior of the

ultrasonic hopper dispensing system. Such knowledge can provide guidance for selection and adjustment of dispensing variables of the printer to achieve a desirable dispense rate, and therefore, to ensure the quality of printed parts with minimal manufacturing cost.

This paper presents a study aiming to provide the needed knowledge to understand the powder dispensing behavior of an ultrasonic hopper dispensing system equipped on a commercial binder jetting 3D printer. In this study, effects of three dispensing variables (ultrasonic mode, ultrasonic intensity, and initial feedstock amount) and cumulative number of dispensing cycles on dispense rate are experimentally investigated. The rest of the paper is organized as follows. Section 7.2 describes experimental setup and conditions, measurement method of dispensed powder amount, and determination of dispense rate. Section 7.3 presents results and discussion. Section 7.4 summarizes findings from the study.

7.2. Experimental Setup and Conditions

7.2.1. Ultrasonic hopper dispensing system

Figure 7.1 illustrates the ultrasonic hopper dispensing system on the ExOne Innovent Plus binder jetting 3D printer. The dispensing system consists of three components: hopper, ultrasonic generator, and screen. The half angle of the wedge hopper is 22.3°, the outlet width is 12.2 mm, the height of the wedge portion is 40 mm, the hopper height is 250 mm, and the width of the hopper at the entrance is 144 mm. The ultrasonic generator is connected to the right side of the hopper, and the screen is attached to the bottom of the hopper. Feedstock powder is dispensed through the screen only when

ultrasonic vibration is activated. One dispensing cycle is defined as follows. At the beginning of a dispensing cycle, ultrasonic vibration is activated when the dispensing system is at the right side of the job box (Figure 7.1a). Then, the dispensing system moves towards the left side, while dispensing powder onto the powder bed (Figure 7.1b), until it reaches the left side of the job box. Before the next dispensing cycle, the dispensing system moves to the right side of the job box without dispensing powder.

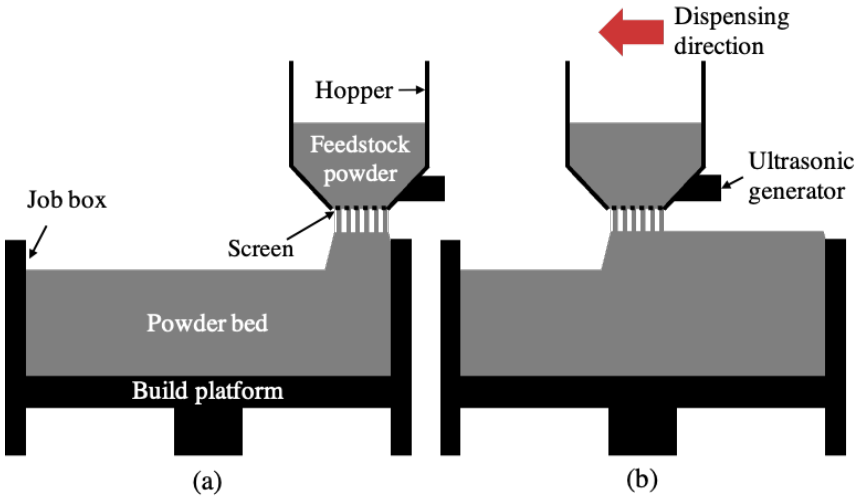

Figure 7.1 Illustration of ultrasonic hopper dispensing system on ExOne Innovent Plus printer. (a) The dispensing system starts dispensing powder at the right side of the job box, and (b) the dispensing system moves towards the left side of the job box

7.2.2. Definitions of dispensing variables

Table 7.2 Definitions of dispensing variables

Dispensing variable	*Definition*
Ultrasonic mode	Combination of ultrasonic ramping speed and ramping pattern at which the ultrasonic generator produces ultrasonic vibration
Ultrasonic intensity (%)	Scaled factor to change the intensity of the ultrasonic vibration
Initial feedstock amount (g)	Amount of powder loaded in the hopper (the hopper is emptied before the initial feedstock amount is loaded)
Recoat speed (mm/s)	Traverse speed of the dispensing system as it moves across the powder bed with ultrasonic vibration on
Time on delay (s)	Duration of time that the dispensing system stays at the right side of the job box with ultrasonic vibration on before it starts to move towards the left side of the job box
Screen size (μm)	Size of the openings of the screen attached to the hopper
Hopper traverse distance (mm)	Traverse distance of the dispensing system across the powder bed with ultrasonic vibration on

The definitions of dispensing variables of the ultrasonic hopper dispensing system are summarized in Table 7.2 [10]. The system offers eight ultrasonic modes, depending on different combinations of ultrasonic ramping pattern and ramping speed, as shown in Table 7.3. Linear ramping pattern increases the ultrasonic frequency from 33 to 37 kHz, and goes back to 33 kHz without any delay; and then repeats. Triangular ramping pattern increases the ultrasonic frequency from 33 to 37 kHz; and then decreases it from 37 to 33 kHz using the same amount of time; and then repeats. The specific values of the ramping speed are proprietary to the manufacturer of the ultrasonic generator (SK3510, TELSONIC, Bronschhofen, Switzerland). The information is acquired via communications with the manufacturer. Ultrasonic intensity can be adjusted through

either hardware or software. The physical switches of the ultrasonic generator offer eight settings from 30% to 100% by 10% increment. The software offers four options of ultrasonic intensity from 25% to 100% by 25% increment. The product of the physical setting percentage and the software setting percentage determines the ultrasonic intensity.

Table 7.3 Available ultrasonic modes and their ramping pattern and ramping speed

Mode	*Ramping pattern*	*Ramping speed*
A	Linear	Slow
B	Linear	Normal
C	Linear	Fast
D	Linear	Extra fast
E	Triangular	Fast
F	Triangular	Normal
G	Triangular	Slow
H	Triangular	Extra slow

7.2.3. Experimental conditions

Effects of three dispensing variables (ultrasonic mode, ultrasonic intensity, and initial feedstock amount) and cumulative number of dispensing cycles on dispense rate were tested in four experiments. Table 7.4 shows the experimental conditions for these four experiments. In Experiment 1, the sequence to conduct tests was randomized for eight modes (H→B→A→E→G→C→F→D), and the same sequence was repeated three times. Dispensed powder was collected after five dispensing cycles (number of dispensing cycles = 5) for each ultrasonic mode without resetting initial feedstock amount. In Experiment 2, four levels of ultrasonic intensity were tested, with the sequence randomized and three replications for each level. Dispensed powder was also collected after five dispensing cycles (number of dispensing cycles = 5) for each level of ultrasonic intensity without

resetting initial feedstock amount. In Experiment 3, four levels of initial feedstock amount were tested, with the sequence randomized and each repeated three times. Dispensed powder was collected after every 20 dispensing cycles (number of dispensing cycles = 20) for each level of initial feedstock amount. The cumulative number of dispensing cycles (i.e., total number of dispensing cycles since the hopper is loaded with the initial feedstock amount) was 100 for each level of initial feedstock amount. In Experiment 4, dispensed powder was collected after 20 dispensing cycles (number of dispensing cycles = 20). The cumulative number of dispensing cycles was not predetermined. The experiment was run until the feedstock powder in the hopper was emptied. Other dispensing variables (recoat speed, time on delay, screen size, and hopper traverse distance) were the same for all the experiments.

Table 7.4 Experimental conditions

Variable	*Experiment 1*	*Experiment 2*	*Experiment 3*	*Experiment 4*
Ultrasonic mode	A, B, C, D, E, F, G, H	D	C	C
Ultrasonic intensity (%)	100	25, 50, 75, 100	100	100
Initial feedstock amount (g)	2000	2000	2000, 4000, 6000, 8000	4000
Number of dispensing cycles	5	5	20	20
Cumulative number of dispensing cycles			100	*till the hopper was emptied

Other dispensing variables: Recoat speed = 30 mm/s; Time on delay = 2 s; Screen size = 170 μm; Hopper traverse distance = 75 mm.

7.2.4. Feedstock powder

Table 7.5 presents properties of the SS316L powder (S3109, ExOne, Pennsylvania, USA) used in this study. Each value is the average of three measurements. In this study, the standard error was calculated via $SE = \sigma/\sqrt{n}$ where σ is standard deviation of samples, and n is number of samples. The definitions of these properties (apparent density, tap density, repose angle, Hausner Ratio, and D10, D50, and D90) can be found in the literature regarding powder properties [11,12]. Apparent density and tap density of the powder were measured in accordance with ASTM B417-13 and B527-15 [13,14]. The measured apparent density and tap density are absolute density with the unit of g/cm^3. The density values presented in Table 7.5 are relative density, which is the absolute density of the powder divided by the theoretical density of the powder material. Theoretical density of SS316L used to calculate apparent density and tap density is 7.9 g/cm^3 [15]. Repose angle was measured with assistance of the image processing software (ImageJ, National Institute of Health, Maryland, USA).

Table 7.5 Properties and particle size of SS316L powder

Property	*Average*	*Standard Error*
Apparent density (%)	47.8	0.6
Tap density (%)	59.0	0.1
Hausner Ratio	1.234	0.002
Repose angle (°)	49.998	2.110
Mean size (μm)	10.598	0.076
D10 (μm)	5.650	0.037
D50 (μm)	9.797	0.042
D90 (μm)	16.454	0.167

Particle size data of the powder in Table 7.5 were obtained by a particle size analyzer (LA-960, Horiba, Kyoto, Japan). The primary axis on the left side of Figure 7.2 (a) is volume percentage of the powder (density distribution), and the secondary axis on the right side of Figure 7.2 (a) is cumulative volume percentage of the powder (cumulative distribution [16]) . The error bars in Figure 7.2 (a) (and Figures 7.4, 7.5, 7.6, 7.8, 7.9, and 7.10) were drawn with upper and lower caps representing corresponding standard error. The mean particle size of the powder was around 10 µm, which is much smaller than the screen size (170 µm) attached to the hopper. Particle size distribution of the powder was relatively narrow. Figure 7.2 (b) shows scanning an electron microscopy image (JSM-7500F, JEOL, Tokyo, Japan) of the powder. It can be observed that the powder had spherical shape. Prior to conducting the experiments, the powder was spread in a large pan (20"L × 12"W × 1"D), and kept in a drying oven (DX402C, Yamato Scientific America, California, USA) for eight hours at 65 °C to reduce moisture content of the powder.

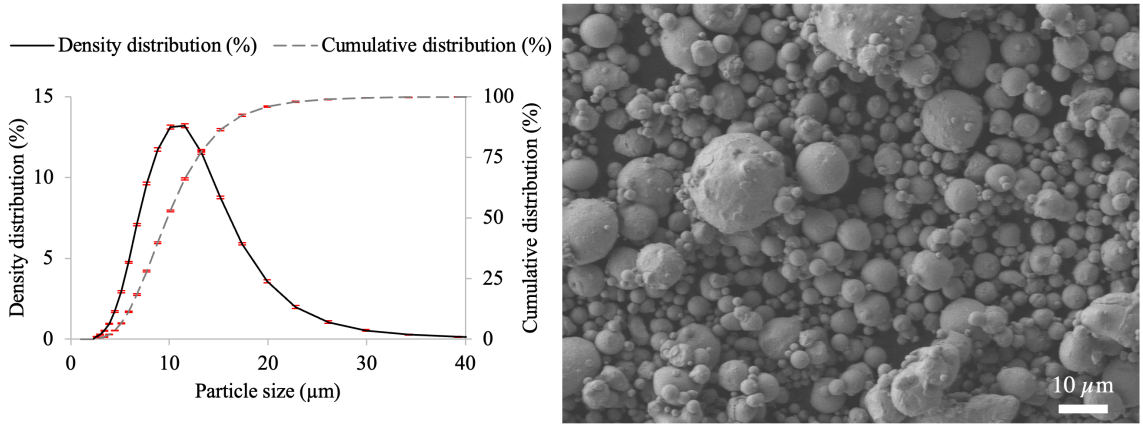

(a) (b)

Figure 7.2 Characteristics of the SS316L powder. (a) density distribution and cumulative distribution, and (b) scanning electron microscope image

7.2.5. Measurement of dispensed powder amount and determination of dispense rate

Figure 7.3 shows the experimental setup for measuring dispensed powder amount. The ultrasonic hopper dispensing system dispensed the powder contained in the hopper into a pan (12"L × 8"W × 1"D). After the pre-determined number of dispensing cycles (listed in Table 7.4), the dispensed powder in the pan was manually transferred to a small bin (6"L × 4"W × 2"D) by a brush. The dispensed powder in the bin was weighed by a lab scale (TEK-AB-0392, Yae First Trading, CA, USA) with a maximum measurable weight of 500 g and a resolution of 1 mg. The weight measured was recorded as the dispensed powder amount. Dispense rate (g/s) was then calculated via the following equation.

$$Dispense\ rate = \frac{Dispensed\ powder\ amount}{Number\ of\ dispensing\ cycles * \left(\frac{Hopper\ traverse\ distance}{Recoat\ speed} + Time\ on\ delay\right)}$$

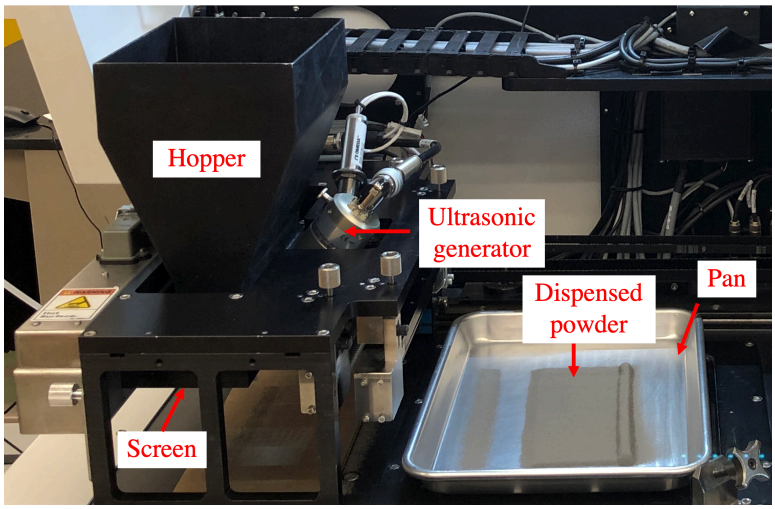

Figure 7.3 Experimental setup for measuring dispensed powder amount

7.3. Results and Discussion

7.3.1. Effects of ultrasonic mode and ultrasonic intensity

Figure 7.4 shows the change of dispense rate as ultrasonic mode changed. When ultrasonic ramping pattern was linear (Mode A to Mode D), dispense rate did not change much as ramping speed changed, except that the “Fast” ramping speed generated slightly higher dispense rate than other ramping speeds. When ultrasonic ramping pattern was triangular (Mode E to Mode H), dispense rate decreased significantly as ultrasonic ramping speed decreased.

The reported study in the literature closest to this study was done by Touze et al. [17]. They attached a piezoelectric transducer to the side wall of a funnel (similar to that of a Hall flowmeter). They varied vibration frequency from 1 to 10 kHz to investigate the flow rate of Al-Cu powder for the application of laser metal deposition. They observed that vibration frequency of 3 kHz generated the highest flow rate. Note that their vibration frequencies were much lower than the vibration frequencies in this study (from 33 to 37 kHz), and they did not change ramping speed and pattern.

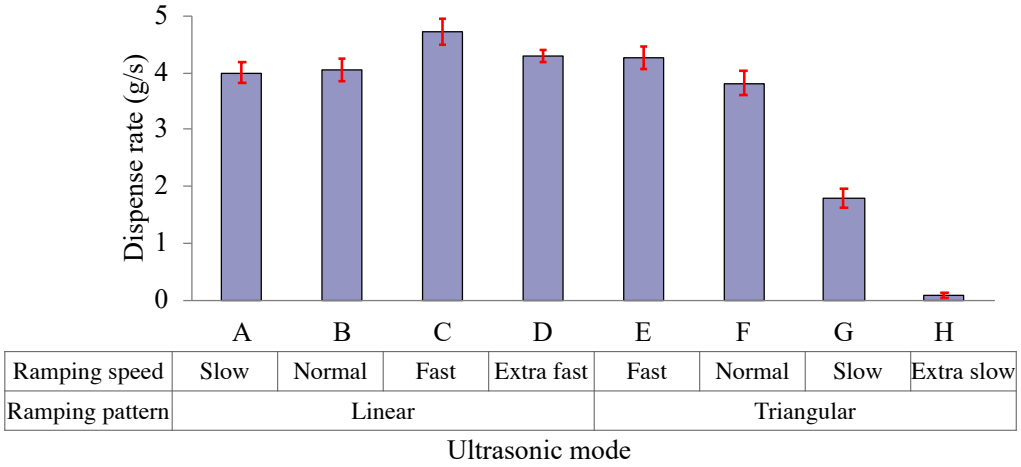

Figure 7.4 Effects of ultrasonic mode on dispense rate (ultrasonic intensity: 100%, initial feedstock amount: 2000 g, and number of dispensing cycles: 5)

Figure 7.5 displays the change of dispense rate as ultrasonic intensity changed. Dispense rate increased approximately linearly as ultrasonic intensity increased. This result was consistent with the observations made by Wu et al. [19]. In their study, the amplitude of a piezoelectric transducer was studied for micro feeding of SS316L powder through a needle attached to a syringe. They observed that flow rate increased with higher vibration amplitude.

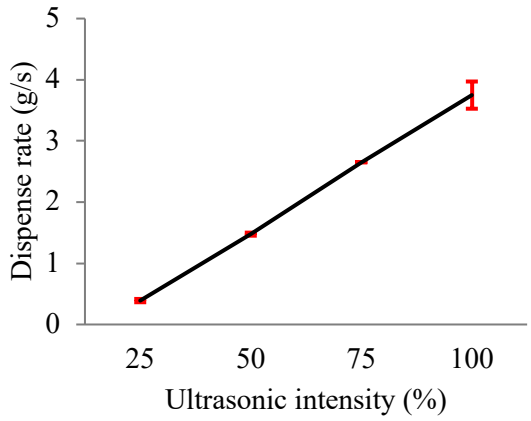

Figure 7.5 Effects of ultrasonic intensity on dispense rate (ultrasonic mode: C, initial feedstock amount: 2000 g, and number of dispensing cycles: 5)

7.3.2. Effects of initial feedstock amount in hopper

Figure 7.6 shows the change of dispense rate as initial feedstock amount changed. Dispense rate shown is the average over the 100 dispensing cycles. It can be observed that dispense rate with initial feedstock amount of 2000 g was higher than those with initial feedstock amount of 4000, 6000, and 8000 g. Tukey's honestly significant difference test [20] was used to test whether these differences are statistically significant. Table 7.6 lists *p*-values for comparing statistical differences in dispense rate between any two levels of initial feedstock amount. Dispense rate with initial feedstock amount of 2000 g was statistically higher (at the significance level of 4%) than those with initial feedstock amount of 4000, 6000, and 8000 g.

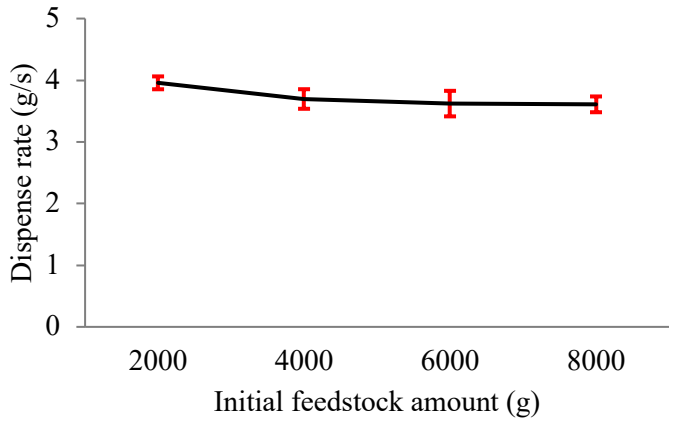

Figure 7.6 Effects of initial feedstock amount on dispense rate (ultrasonic mode: C, ultrasonic intensity: 100 %, and number of dispensing cycles: 20)

Table 7.6 p-values from Tukey's honestly significant difference test to determine statistical differences in dispense rate between any two levels of initial feedstock amount

Initial feedstock amount	4000 g	6000 g	8000 g
2000 g	**0.039**	**0.005**	**0.003**
4000 g		0.861	0.799
6000 g			0.999

This paper is the first report on the effects of initial feedstock amount on dispensing behavior of the ultrasonic hopper dispensing system for powder bed additive manufacturing in the literature. A reported study close to this was conducted by Anand et al. [21]. They investigated discharge rate (i.e., dispense rate) of powder from a wedge-shaped hopper using simulation (by the discrete element method). They reported that discharge rate of bimodal granular powder did not change as the fill height of powder in the hopper changed when friction coefficient of particles was high. However, they observed that the discharge rate increased as the fill height of powder in the hopper

increased when friction coefficient of particles was low. Their simulation results could not explain the results in this study: smaller initial feedstock amount produced higher dispense rate.

The authors proposed the following hypothesis to explain why smaller initial feedstock amount produced higher dispense rate. When more powder was loaded in the hopper, more weight and pressure were applied to the powder particles in the lower part of the hopper. This would cause these particles to pack more tightly, and, hence, increase their packing density. Assuming that it was more difficult for densely packed particles to pass through the screen (when other conditions are the same), larger initial powder amount would cause lower dispense rate. To test this hypothesis, density of the powder in the lower part of the hopper was measured for four levels of initial feedstock amount (2000, 4000, 6000, and 8000 g). For each level of initial powder amount, after adding the feedstock powder into the hopper, the hopper was separated into upper and lower parts by sliding away the upper part of the hopper, as shown in Figure 7.7. Then the weight of the powder in the power part of the hopper was measured. For each level of initial feedstock amount, three weight measurements were taken, and the average value of the three measurements was used as the weight of the powder in the lower part of the hopper. The volume of the hopper was calculated using the weight of water that filled the lower part of the hopper, assuming that density of water at room temperature is 0.997 g/cm^3. The density of powder in the lower part of the hopper (%) was calculated using the following equation:

$$Density\ of\ powder\ in\ the\ lower\ part\ of\ the\ hopper = \frac{\left(\frac{Weight\ of\ the\ powder\ in\ the\ lower\ part\ of\ the\ hopper}{Volume\ of\ the\ water\ in\ the\ lower\ part\ of\ the\ hopper}\right)}{Theoretical\ density\ of\ powder\ material}$$

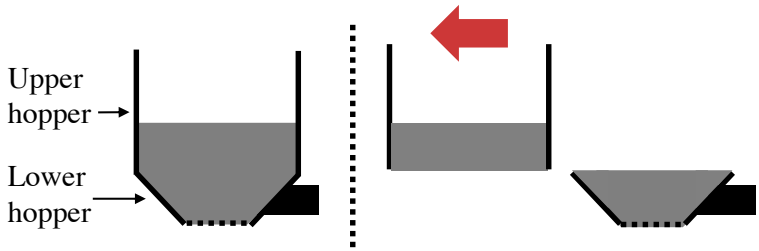

Figure 7.7 Separation of the hopper into upper and lower parts by sliding away the upper part

The relationship between the feedstock density in the lower part of the hopper and initial feedstock amount is shown in Figure 7.8. At the lowest level of initial feedstock amount (2000 g), the feedstock powder in the lower part of the hopper was the lowest. Tukey's honestly significant difference test [20] was used to test whether these differences are statistically significant. Table 7.7 lists *p*-values for comparing statistical differences in density of powder in the lower part of the hopper between any two levels of initial feedstock amount. The result showed that the feedstock density in the lower part of the hopper when initial feedstock amount was 2000 g was statistically different (at the significance level of 7%) from those when initial feedstock amount was 6000g and 8000g.

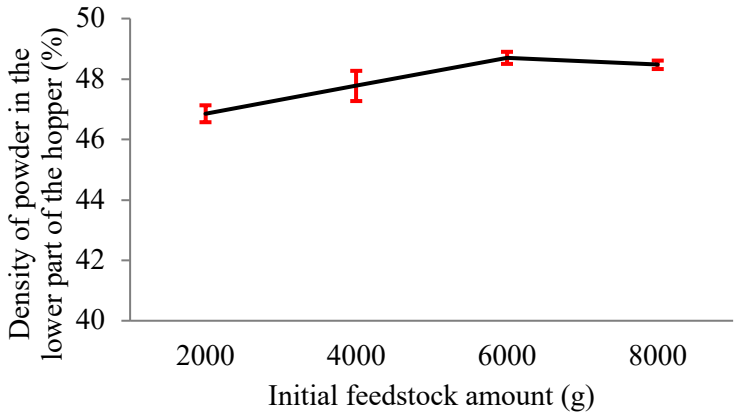

Figure 7.8 Effects of initial feedstock amount on density of powder in the lower part of the hopper

Table 7.7 p-values from Tukey's honestly significant difference test to determine statistical differences in density of powder in the lower part of the hopper between any two levels of initial feedstock amount

Initial feedstock amount	4000 g	6000 g	8000 g
2000 g	0.141	**0.009**	**0.065**
4000 g		0.335	0.731
6000 g			0.983

7.3.3. Effects of cumulative number of dispensing cycles

The relationship between cumulative number of dispensing cycles and dispense rate is displayed in Figure 7.9. It can be observed that dispense rate gradually decreased as cumulative number of dispensing cycles increased. Dispense rate decreased faster in the beginning, but became relatively stable as cumulative number of dispensing cycles increased. The effects of cumulative number of dispensing cycles on dispensing behavior of the ultrasonic hopper dispensing system for powder bed additive manufacturing have not been reported in the literature.

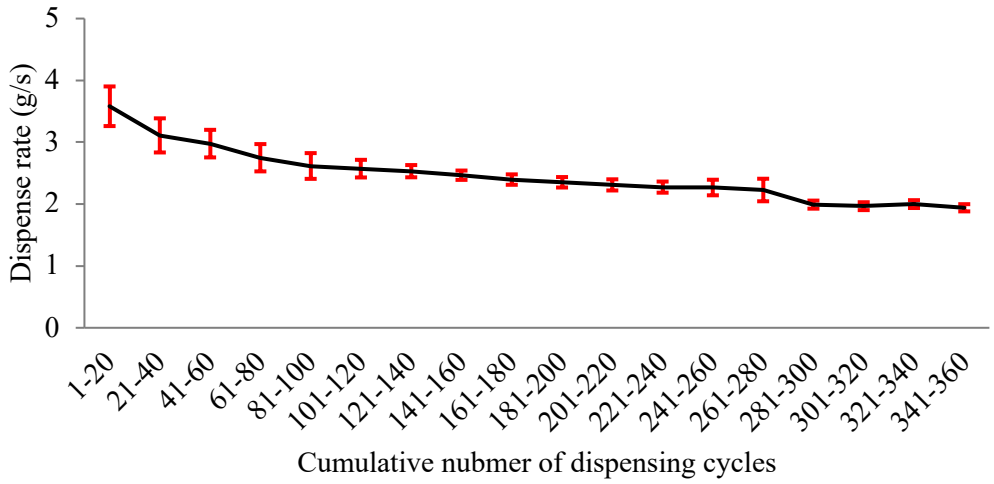

Figure 7.9 Effects of cumulative number of dispending cycles on dispense rate (ultrasonic mode: C, ultrasonic intensity: 100 %, initial feedstock amount: 4000 g, number of dispensing cycles: 20)

The authors hypothesized that the powder inside the hopper became denser as cumulative number of dispensing cycles increased, which in turn decreased dispense rate. To test this hypothesis, feedstock density in the lower part of the hopper was measured under two cases. In one case, 4000 g of the powder was added into the hopper, and the density of the powder at the lower part of the hopper was measured. In another case, 4000 g of the powder was added into the hopper, and 2000 g of the powder was dispensed from the hopper to keep the remaining feedstock powder to be 2000 g. Then, the density of the powder in the lower part of the hopper was measured using the same method described in Section 7.3.2. Measurements under each case were repeated two more times, and the average value of the three measurements was used as the density of powder in the lower part of the hopper for each case.

The results are presented in Figure 7.10. It can be seen that there was a clear difference between these two cases. Analysis by a studentized t-test [20] showed that the difference is statistically different (p-value = 0.03). Therefore, decreasing dispense rate as cumulative number of dispensing cycles increased could be attributed to the increase of density of the powder in the lower part of the hopper.

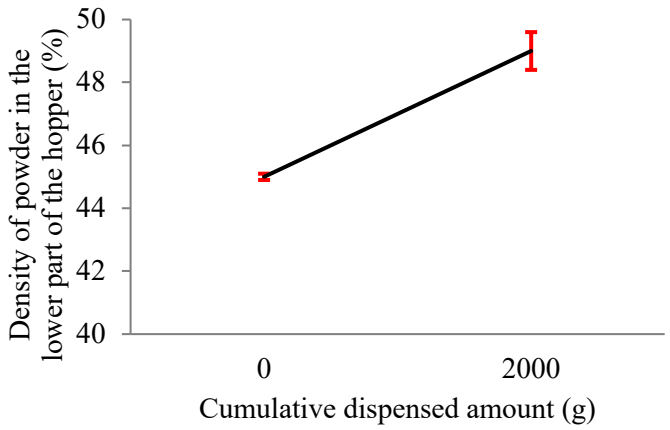

Figure 7.10 Effects of cumulative dispensed amount on density of powder in the lower part of the hopper

7.4. Conclusions

This paper reports an experimental study on powder dispensing behavior of the ultrasonic hopper dispensing system equipped on the ExOne Innovent Plus binder jetting 3D printer. The powder dispensing behavior was evaluated using dispense rate of feedstock powder. The dispensing variables investigated were ultrasonic mode (ultrasonic ramping speed and pattern), ultrasonic intensity, and initial feedstock amount loaded into the hopper. Effects of cumulative number of dispensing cycles (a variable associated with cumulative dispensed powder amount) on dispense rate were also investigated. The following conclusions can be drawn from the study.

- When ultrasonic ramping pattern was linear, dispense rate changed little as ultrasonic ramping speed increased.
- When ultrasonic ramping pattern was triangular, dispense rate decreased as ultrasonic ramping speed decreased.
- As ultrasonic intensity increased, dispense rate increased.
- Dispense rate was higher with smaller initial feedstock amount in the hopper.
- Dispense rate gradually decreased as cumulative number of dispensing cycles increased.
- Density of powder in the lower part of the hopper was higher when initial feedstock amount was larger.
- Density of powder in the lower part of the hopper became higher as cumulative number of dispensing cycles increased.

The above conclusions are obtained from the experiments using one type of powder. It is possible that the results might be different for other types of powders. For example, the initial feedstock amount in hopper (powder height in the hopper) might have little effect on flow rate for another type of powder. Nevertheless, the findings from this study provide guidance to develop approaches to reduce the variation in dispense rate. For example, keeping the amount of feedstock powder in the hopper relatively constant will reduce the variation in dispense rate. If the amount of feedstock powder in the hopper cannot be kept relatively constant, variation in dispensing rate can be minimized by changing ultrasonic intensity accordingly. The results from this study can be useful to both manufacturers and users of 3D printers equipped with ultrasonic hopper dispensing systems.

7.5. References

[1] ASTM International 52900-15, 2015, "Standard Terminology for Additive Manufacturing - General Principles - Terminology," West Conshohocken, PA.

[2] Mostafaei, A., Elliott, A., Barnes, J., Cramer, C., Nandwana, P., and Chmielus, M., 2020, "Binder Jet 3D Printing – Process Parameters, Materials, Properties, and Challenges," Progress in Materials Science, vol. 119, 100707.

[3] Du, W., Ren, X., Pei, Z., and Ma, C., 2020, "Ceramic Binder Jetting Additive Manufacturing: A Literature Review on Density," Journal of Manufacturing Science and Engineering, vol. 142, no. 4, 040801.

[4] Miao, G., Du, W., Moghadasi, M., Pei, Z., and Ma, C., 2020, "Ceramic Binder Jetting Additive Manufacturing: Effects of Granulation on Properties of Feedstock Powder and Printed and Sintered Parts," Additive Manufacturing, vol. 36, 101542.

[5] Mendoza, E., Ding, D., Su, L., Joshi, A., Singh, A., Jayan, R., and Beuth, J., 2019, "Parametric Analysis to Quantify Process Input Influence on The Printed Densities of Binder Jetted Alumina Ceramics," Additive Manufacturing, vol. 30, 100864.

[6] Miyanaji, H., Rahman, K., Ma, D., and Williams, C., 2020, "Effect of Fine Powder Particles on Quality of Binder Jetting Parts," Additive Manufacturing, vol. 36, 101587.

[7] Myers, K., 2018, "Smooth, Knurled, Steel, and Dual Roller Testing," ExOne.

[8] Shrestha, S., and Manogharan, G., 2017, "Optimization of Binder Jetting Using Taguchi Method," The Minerals, Metals & Materials Society, vol. 69, no. 3, pp. 491–497.

[9] Niino, T., and Sato, K., 2009, "Effect of Powder Compaction in Plastic Laser Sintering Fabrication," 20th Annual International Solid Freeform Fabrication Symposium, pp. 193–205.

[10] ExOne, 2021, "Innovent® 3D Printing System User Manual Version 1.02.04 – 2015-04," Available: https://cdme.osu.edu/sites/default/files/uploads/exone_-_3d_printer_-_manual.pdf

[11] Ali, U., Mahmoodkhani, Y., Shahabad, S., Esmaeilizadeh, R., Liravi, F., Sheydaeian, E., Huang, K., Marzbanrad, E., Vlasea, M., and Toyserkani, E., 2018, "On the Measurement of Relative Powder-Bed Compaction Density in Powder-Bed Additive Manufacturing Processes," Materials and Design, vol. 155, pp. 495–501.

[12] Shah, R., Tawakkul, M., Khan, M., 2008, "Comparative Evaluation of Flow for Pharmaceutical Powders and Granules," American Association of Pharmaceutical Scientists PharmSciTech. vol. 9, no. 1, pp. 250–258.

[13] ASTM International B417-13, 2013, "Standard Test Method for Apparent Density of Non-Free-Flowing Metal Powders Using the Carney Funnel," West Conshohocken, PA.

[14] ASTM International B527-15, 2015, "Standard Test Method for Tap Density of Metal Powders and Compounds," West Conshohocken, PA.

[15] ExOne, 2021, "316L Stainless Steel," Available: https://www.exone.com/Admin/getmedia/92ff696e-1b4e-4c7e-a45c-ae45b04340da/PSC_X1_MaterialData_316L_10192020_V6.pdf

[16] Leschonski, K., 1984, "Representation and Evaluation of Particle Size Analysis Data," Particle and Particle Systems Characterization, vol. 1, no. 1-4, pp. 89–95.

[17] Touze, S., Rauch, M., Hascoet, J., 2020, "Flowability Characterization and Enhancement of Aluminium Powders for Additive Manufacturing," Additive Manufacturing, vol. 36, 101462.

[18] Saito, M., 1993, "A Method of Powder Supply Using An Ultrasonic Vibrating Plate with Multiholes," The Journal of The Acoustical Society of Japan, vol. 14, no. 4, pp. 275–278.

[19] Wu, H., Pritchet, D., Wolff, S., Cao, J., Ehmann, K., and Zou, P., 2020, "A Vibration-Assisted Powder Delivery System for Additive Manufacturing - An Experimental Investigation," Additive Manufacturing, vol. 34, 101170.

[20] Akritas, M., 2016, “Probability & Statistics with R for Engineers and Scientists,” Pearson Education, pp. 193–197.

[21] Anand, A., Curtis, J., Wassgren, C., Hancock, B., and Ketterhagen, W., 2008, “Predicting Discharge Dynamics from A Rectangular Hopper Using The Discrete Element Method (DEM),” Chemical Engineering Science, vol. 63, no. 24, pp. 5821–5830.

8. CONCLUSIONS AND CONTRIBUTIONS

In this dissertation, final part qualities, including mechanical properties, surface roughness, dimensional accuracy, and color accuracy of parts printed by the PolyJet 3D printing process are investigated experimentally and theoretically. Additionally, powder dispensing behavior of ultrasonic hopper powder dispensing system equipped in a Binder Jetting process is investigated. The following conclusions are drawn from the studies.

1. As to print orientation of the PolyJet process, samples printed with their longest dimension aligned with the X axis have statistically higher elastic modulus and elongation, and samples aligned with the Y axis have statistically higher UTS. Samples aligned with the Z axis have the significantly lower mechanical properties. With respect to layer thickness, it is found that larger layer thickness leads to statistically higher elastic modulus, UTS, and elongation than smaller layer thickness. Highest mechanical properties can be achieved by orienting the longest dimension of a part along the X axis and the largest surface perpendicular to either the Y or Z axis.
2. With respect to finish type of the PolyJet process, samples printed using glossy finish type have statistically lower surface roughness than matte finish type, and glossy finish type have more accurate dimensions than matte finish type for the X and Y axes. For Shore hardness, higher Shore hardness values have lower surface roughness, and a larger value of Shore hardness lead to better dimensional accuracy in the Y axis, whereas smaller value of Shore hardness provides more accurate dimension in the X axis. It can be recommended that the combination of glossy finish and Shore hardness 100 will achieve lowest surface roughness and highest dimensional accuracy.

3. As to finish type of the PolyJet process, samples printed with matte finish type have lower brightness, and more green and blue elements, compared to glossy finish type. There are significant interaction effects between finish type and material color. Black material is influenced by difference in finish type more significantly, compared to cyan, magenta, and yellow materials. Glossy finish type is recommended to avoid color contamination for a darker color.
4. Most printed RGB values from the PolyJet process range from 50 to 200 in the RGB system, and it is not possible to achieve extreme low or high printed RGB values. Moreover, lower ranges of R value and upper ranges of B value are prone to produce higher deviations of printed colors. Printed RGB values are crossly correlated with the specified RGB values so that a nonlinear model is more suitable for predicting printed RGB values. MLP outperforms linear and cubic regression for coefficient of determination and mean absolute error, and the performance of cubic regression is better than linear regression, which indicates that the relationship between specified RGB and printed RGB is nonlinear.
5. Response surface methodology is an effective way to compensate deviations between specified color and target color in the PolyJet process. Experimental results show that the proposed method performed better than the conventional specification method (directly using the target color as the specified color in printer software) in achieving target colors.
6. Dispense rate gradually decreases as the cumulative number of dispensing cycles increases in the ultrasonic hopper powder dispensing system. When the ultrasonic

mode is triangular ramping pattern, dispense rate decreases as ultrasonic ramping speed decreases. As ultrasonic intensity increases, dispense rate increases. Dispense rate is higher with smaller initial feedstock amount in the hopper.